Moving Base INS/GPS Vector Gravimetry on a Land Vehicle

by

Xiaopeng Li

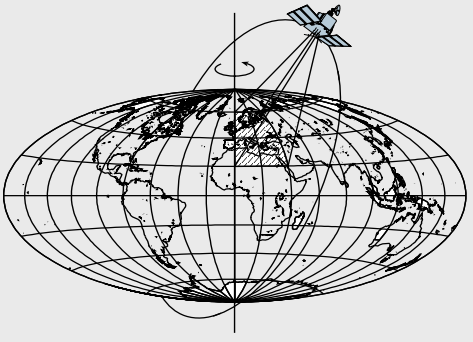

Report No. 486

Geodetic Science and Surveying

The Ohio State University
Columbus, Ohio 43210

December 2007

Moving Base INS/GPS Vector Gravimetry on a Land Vehicle

by

Xiaopeng Li

Report No. 486

Geodetic Science and Surveying

The Ohio State University
Columbus, Ohio 43210

December 2007

PREFACE

This report was prepared for and submitted to the Graduate School of the Ohio State University as a dissertation in partial fulfillment of the requirements for the PhD degree.

The research was supported by a grant from the National Geospatial Intelligence Agency (NMA202-98-1-1110) under the NGA University Research Initiative program. Additional assistance came from the Center for Mapping at the Ohio State University in the form of GPSVan survey and data analysis support.

ABSTRACT

The Inertial Navigation System and Global Positioning System (INS/GPS) system has been extensively studied over several decades, mostly for the purpose of navigation and kinematic position. Because the INS system is affected by gravitation, the integration definitely needs gravity data in order to yield accurate results. It is natural to reverse the problem and attempt a measurement of the gravity vector. The gravimetric system based on INS/GPS shows good performances in the airborne scenarios. Moving the system into a ground vehicle will help to improve the resolution of the gravity estimates, considering its lower speed and altitude. However, the system will face much more complicated dynamics and harsh observation conditions.

In this study, a two-stage extended Kalman filter based on processing noise adaptation is used to fix the position gaps and provide prior information of the Inertial Measurement Units (IMU) errors. The kinematic acceleration is computed by both the position method and the phase method. All these procedures improve the steadiness and precision of the system. The advanced wavelet de-noising technique is employed to further isolate the gravity disturbance from the observation errors in the residuals of the novel Kalman filter, previously developed at the Ohio State University (OSU). The final precision of the gravity disturbance estimates is further improved by correlatively filtering the repeated estimates in the frequency domain.

An intensive survey campaign was carried out to test the validities of these techniques. Based on data analysis, the results show significant consistency (as good as 0.6mGal, STD) in the vertical component on the repeated traverses, and comparison to control data indicates an accuracy of 2-3mGal (STD). However, it is also determined that the control data, being interpolated from a database, have an accuracy of approximately 3mGal (STD). Resolution of the estimated gravity disturbance is about 2km, based on 180-s data smoothing and a vehicle speed averaging about 80km/hr. Large scale errors exist in the horizontal gravity estimates. Removing these on the basis of extensive deflection of the vertical control yields repeatability in the horizontal components in the range of 2-15mGal (STD) and agreement with the control at the level of 5-9mGal (STD).

ACKNOWLEDGMENTS

First and foremost, I wish to express my deepest appreciation to my advisor Professor Christopher Jekeli, for his invaluable advice, patience and support throughout my graduate studies. His world-class guidance has made it a truly enjoyable and valuable experience in my years of education. I also want to acknowledge Professor C.K. Shum and Professor Ralph R. B. von Frese for reviewing this study and being part of the dissertation committee.

My gratitude also goes to Professor Burkhard Schaffrin, Professor Dorota Grejner-Brzezinska and Dr. Charles Toth (OSU Center for Mapping) for their useful help in my study. I would like to thank the NGA experts, Steven Kenyon, Robert Anderson, Terry Timblin, and Glen Noll, for their help in collecting the INS/GPS data in Montana.

Finally, I would like to express appreciation to my parents and brothers for their continuous love and support.

TABLE OF CONTENTS

Page

CHAPTER 1

INTRODUCTION

1.1 Background

The gravity field of the Earth is directly related to the mass distribution of the Earth. High resolution model of the Earth's gravity field is desirable in many applications. For example, in geodesy and solid Earth geophysics, it can help to define better the shape of the Earth, and to understand the subsurface of the Earth. In oceanography, it can help to determine the geostrophic current by comparing the slope of the geoid and the slope of the sea surface as profiled by altimetery. In oil and mineral explorations, it can help to detect the local geology features. The degree of resolution of the Earth's gravity field model directly depends on the resolution of the available gravity data. The gravity itself, as well as its related quantities such as gravitational differences, may be observed by various techniques such as Satellite to Satellite Tracking (SST), Satellite Gravity Gradiometry (SGG), airborne gravimetry, and ground gravimetry. Satellite based systems generally provide only mid-to-long (>100km) wavelength information of the gravity field. Although the traditional static ground gravimetry offers the most accuracy, it is very time and labor consuming to have adequate data coverage. Even the most advanced instruments (e.g. Hirt and Burki 2002) still need tens of minutes to finish one station. Furthermore, it is not very easy to establish benchmarks for the ground instruments in may regions of the Earth's surface, such as the ocean and mountainous areas.

The moving-base gravimetric system either based on an aircraft, a ground vehicle, or a ship, serves as a good alternative to measure the gravity disturbance, which is defined as the difference between the actual gravity and the normal gravity; for a mathematical definition see Heiskanen and Moritz (1967). In general, there are three categories of moving base gravimetric system, i.e., scalar gravimetry, vector gravimetry, and gravity gradiometry.

Scalar gravimetry, either based on gravimeter and GPS or based on INS and GPS, (Brozena 1992; Harrison et al., 1995; Olesen et al., 1997; Wei et al., 1998; Forsberg et al., 1999; Bell et al., 1999; Childers et al., 1999; Williams et al., 2001) measures the magnitude of the gravity disturbance. Thus it only requires measurements along one stabilized axis, which is relatively easier than the other two. However, to obtain the complete vector from such data requires a large amount of gravity data and involves complicated computations such as Least Square Collation (LSC) or Vening-Meinesz type integrals.

Vector gravimetry based on INS/GPS (Salychev et al. 1994; Jekeli and Kwon, 1999), on the other hand, measures all three components of gravity disturbances. It has obvious advantages over the scalar one. For instance, the along track relative geoid can be determined by the along track integration of the horizontal components rather than from surveys of the vertical components over a large area as is required by the Stokes solution to the geopotential boundary value problem. However, it requires the stabilization of the sensor package about three axes and is much more difficult to achieve. The principal difficulty with the method lies with the errors in the gyroscopes that provide orientation of the system in inertial space. As Jekeli and Kwon (1999) point out, a large north or east orientation error couples with the large vertical acceleration into the east (or north) gravity component (Hannah 2001). A leveling error of $1''$, for example, produces a 5mGal gravity error. As proved by covariance analysis (Knickmeyer 1990), a gyro drift uncertainty of $0.0001^\circ/h$ and a gyro random walk of $0.0001^\circ/\sqrt{h}$ are needed to achieve an accuracy of 1mGal for the horizontal components of the gravity disturbance vector. On the other hand, simulation studies (Wei and Schwarz 1994) showed that to obtain an accuracy of 1mGal for all components of the gravity disturbance vector, an INS with gyro drifts of $0.0001^\circ/h$ is required.

Gravity gradiometry (Jekeli 1993) measures differences in acceleration instead of measuring acceleration directly. A number of prototype systems were developed in the 70s and 80s of the last century. But only one airborne field test was undertaken, which indicated that this system could recover $5' \times 5'$ mean gravity anomalies to an accuracy of a few mGals on a grid of orthogonal tracks spaced 5km apart and at an altitude of 700km above the terrain (Jekeli 1993). However, due to the expensive cost, the system has been slow to move beyond the prototype mode and was only recently commercialized (Hammond and Murphy 2003, Murphy 2004).

As a result, the INS/GPS based moving base vector gravimetric system is an efficient choice for providing high resolution gravity data in a local area. The moving base systems, primarily the airborne systems, have been extensively studied and successfully used in many applications (Schwarz et al., 1992; Salychev et al., 1994; Kwon et al., 2001 among others.). However, the system observation errors, both GPS

error and INS error, continue to pose a major challenge to researchers attempting to simultaneously increase the accuracy and bandwidth of the gravity disturbance estimates. Furthermore, the ill-posed downward continuation (Jekeli and Serpas, 2003) should also be properly handled in order to obtain the gravity anomalies on the geoid or on the terrain.

In principle, the closer the system is to the surface of the Earth, the stronger the gravity signal. To increase the signal-to-noise ratio (SNR) and to minimize the downward continuation effects, a terrestrial moving base vector gravimetric prototype based on INS/GPS was developed at the Ohio State University (OSU). Considering that the power of the gravity field (especially the short wavelength part) intensifies steadily with a decrease in the altitude, the SNR should increase in the terrestrial system. Moreover, the lower velocity of the road vehicle should also improve the resolution and accuracy of the results.

1.2 Statement of the problem

The moving base vector gravimetric system is a combination of GPS and INS. The GPS system provides precise positioning and kinematic acceleration solutions, while the INS system offers the specific forces encountered by the vehicle. In general, there are two mechanizations for INS, i.e., platform system and strapdown system (Jekeli 2000). In the platform system, the IMUs are installed in a Schuler tuned stabilized platform. Thus the accelerometer and gyros do not encounter the kinematic observation errors directly, which may lead to better gravity estimates (Salychev 1994). But usually, the platform has relatively bigger size, and is very expensive. Unlike the platform system, the IMUs are physically bolted down to the vehicle in the strapdown system. The advantage of the strapdown INS (SINS) is its smaller size, lower cost and more operational flexibility (Jekeli 1995; Kwon 2000). It is Jekeli and Kwon (1999) who for the first time successfully recovered the complete gravity disturbance vector in an airborne SINS/GPS system with 3mGal precision in the down component, and $6-8$mGal precision in the horizontal components.

In the SINS/GPS vector gravimetry system, the specific force is measured by the accelerometers and the kinematic acceleration is measured by GPS. By Newton's second law of motion in a non-rotating coordinate frame, the gravitational force is the difference between the inertial kinematic acceleration and the specific force. As a result, the gravity vector is estimated by subtracting the specific force from the kinematic acceleration. However, in practice, the largest problem in determining the gravity signal is the extremely low SNR. Typically, the gravity disturbance vector does not exceed 100mGal in each component over distances of about 100km (Kwon 2001). But the non-gravitational accelerations measured by INS/GPS can be larger

than the gravity disturbance by factors of 100 to 1000, as reported by Schwarz and Wei. (1994) and Hannah (2001), among others. Only decreasing the altitude of the system can make the gravity disturbance signal stand out more from the observation errors. In any case, it is a challenge to remove the sensor and dynamics induced noise, while leaving the relatively small-amplitude gravity signals intact.

The innovative method developed by Kwon et al. (2001) uses the following three steps to solve this problem. First, the differential GPS (DGPS) technique is used to obtain the GPS kinematic acceleration. Second, a low-pass filter is applied to the GPS and INS accelerations to reduce the high frequency noise and thus increase the SNR. Finally, using the smoothed GPS accelerations as the only system observation updates, the INS errors are estimated by a standard Kalman filter. The gravity disturbance signal is then contained in the observation residuals of the Kalman system. However, this novel approach suffers from the following limitations. First, the DGPS positioning solution usually has gaps due to various reasons, such as GPS satellite signal blocking or strong ionosphere effects, especially in the ground-vehicle based system. These gaps will dramatically damage the precision of the gravity estimation since GPS acceleration calculation depends on a uniform data sequence. Second, the low-pass filter, by definition, does not remove or reduce the long-wavelength INS errors such as the scale error and bias of the IMU. Third, the particularly simple design of the Kalman filter only uses the accelerations as updates while excluding the position and velocity information, which may prevent an optimal estimation of the INS systematic instrument errors.

The ultimate purpose of this study is to explore a general method for the moving base vector gravimetry system, which provides optimal estimation in theory and is easy to implement in practice. The fundamental idea is to remove or reduce the systematic and random errors in both GPS and INS observables, so that all components of the gravity disturbance vector are identified without using too specific and complicated prior models. The following procedures are employed to accomplish these objectives. First, the GPS data and INS data are integrated by a loosely coupled Two-stage Adaptive Extended Kalman Filter (TAEKF) to fix the DGPS positioning gaps. Thus the precise and continuous positioning solutions are available for the following process. Second, in the TAEKF, the INS errors are controlled by the DGPS position and velocity solutions. By applying suitable adaptive schemes in the two-stage filter, the long-wavelength INS errors such as the accelerometer and gyro scale errors and biases are also optimally estimated by the TAEKF. Third, the long-wavelength IMU errors are corrected by using the estimated scale error and bias. The resulting INS measured dynamic acceleration is now better conditioned than before for further processing. Then, the GPS position-derived kinematic acceleration is compared to the accelerations determined directly from the GPS phase (thus skipping the GPS phase

to GPS position determination). The former is called the position acceleration, and the latter is referred as the phase acceleration. They are computed by the so called position method and phase method (Kleusberg et al., 1990; Jekeli 1994; Jekeli and Garcia, 1997; Kennedy 2002; Serrano et al., 2004), respectively. The main advantage of the so-called phase method is that it relaxes the stringent requirement of the position accuracy from cm level to meter level; less than 10 meters (Jekeli and Garcia 1997). As a result, in cases when the position method does not work well due to various reasons, the phase method serves as a backup. To yield the most accurate result, the final GPS kinematic accelerations are determined by correlating the position derived acceleration and the phase derived acceleration in the frequency domain. Then a B-spline smoother is used to reduce the high frequency observation errors both in the kinematic acceleration and in the dynamic acceleration. Finally, these smoothed accelerations are used in the Kalman filter developed by Kwon (2000) to obtain a first estimate of the gravity disturbance from the observation residuals. Furthermore, end-point matching (Serpas 2003), wave-number correlation (Kwon 2000), and wavelet de-noising methods (Li and Jekeli 2004, 2006) are used to further isolate the gravity signals from the observation errors in the Kalman residuals. Moreover, several interpolation methods are studied in order to compare the gravity disturbance estimates with the available ground control data at the same points.

1.3 Chapter description

The fundamental principle of the inertial navigation system, especially the strapdown inertial navigation system (SINS), is briefly overviewed in Chapter 2. The basic observables and the free inertial navigation equation of the SINS are described for the processes treated explicitly in the following chapters.

In Chapter 3, the necessities and methodologies of GPS and INS integration are discussed thoroughly. Out of a number of methods, the TAEKF in a loosely coupled frame is selected to combine the GPS position and velocity data with the free inertial navigation solution for the purpose of fixing the GPS positioning gaps and estimating the IMU long wavelength errors.

Chapter 4 explores methodologies to optimally determine the kinematic acceleration by use of GPS observables. Both the position method and the phase method are applied to yield better kinematic accelerations. Furthermore, a novel Kalman filter is investigated to handle the challenging cycle slip problems in the kinematic scenarios.

Chapter 5 describes the data processing procedures for determining the gravity disturbance in the moving base SINS/GPS vector gravimetry system. Various cutting edge techniques are applied to the Kalman residuals to further isolate the gravity

disturbance from the observation errors. Several interpolation methods are compared to yield the most accurate validation results.

All of these techniques and methods are applied in the SINS/GPS based terrestrial moving base gravimetry campaign conducted by the National Geospatial-Intelligence Agency (NGA) and OSU in southwestern Montana in 2005. The data processing procedure and results are described in chapter 6.

Finally, chapter 7 gives some conclusions and summaries of the moving-base SINS/GPS vector gravimetric system.

CHAPTER 2

INERTIAL NAVIGATION SYSTEM

In general, an inertial navigation system (INS) comprises two sets of inertial measurement units, i.e., accelerometers and gyroscopes. The former one senses the inertial accelerations, while the latter one measures the rotation rate with respect to the inertial frame. The main idea of inertial navigation is based on the acceleration integration. The first integration provides the velocity increment. The second integration yields the vehicle position increments relative to the initial point. In order to match the sensitive axes of accelerometers with a certain navigation coordinate frame, different types of mechanism are used. There are two different concepts for the navigation frame simulation: the stabilized platform and the strapdown configuration. Stabilized platforms provide angular motion isolation from the vehicle; while strapdown system is just what the name implies: the platform holding the IMUs is attached firmly to the vehicle.

The stabilized platform isolates the vehicle's rotation from the IMUs and hence provides more accurate measurements. In the strapdown mode, the accelerations and gyros are physically bolted to the vehicle, where all instruments are contained within a single box. Consequently, these sensors are subjected to the entire range of dynamics of the vehicle, which degrades their performance. In addition, certain modeling errors in the computed navigation solution are caused by numerically integrating the accelerations and angular rates in the body fixed reference frame of the rotating vehicle. At each discrete step of the numerical integration, the frame is assumed to be non-rotating, when in fact it is rotating, resulting in coning errors for the gyroscope and sculling errors for the accelerometers, which need to be properly handled in the computation. However, the strapdown system is small in size, weight, and power consumption, and lower in cost. Furthermore, the recent developments in optimal gyroscopes have brought the strapdown system close to par in accuracy with its gimbaled cousin. So, here, only the strapdown INS (SINS) is studied.

2.1 Introduction

In the strapdown configuration, the accelerometer output, indicating the inertial acceleration of the vehicle, is referenced in the coordinate frame of the vehicle (body frame, or b-frame). Though they are important in actual operations, we will ignore the lever-arm effects and any transformation between the reference frame of each accelerometer and the platform or instrument frames at this moment. It is convenient for an understanding of the strapdown mechanization to think of the accelerations and angular rates as being sensed in the b-frame. The sensed accelerations, a^b, cannot be integrated directly to obtain velocity and position as in the case of the stabilized system that mechanically defines the navigation frame for the accelerometers. Instead, the inertial accelerations for a particular frame must be computed by applying a transformation to the acceleration data according to equation (2.1.1):

$$a^a = C_b^a a^b, \tag{2.1.1}$$

where C_b^a is the orthogonal transformation from the b-frame to some arbitrary frame , a-frame. Here, we select a non-rotating inertial frame, i-frame, as the navigation frame.

In the strapdown mode, the transformation is accomplished computationally, where the rates sensed by the gyros are used to obtain the transformation matrix C_b^i that connects the sensed accelerations to the navigation frame.

$$a^i = C_b^i a^b, \tag{2.1.2}$$

where C_b^i is the transformation matrix from b-frame to i-frame, which can be expressed in terms of quaternions (a, b, c, d) as :

$$C_b^i = \begin{bmatrix} a^2+b^2-c^2-d^2 & 2(bc+ad) & 2(bd-ac) \\ 2(bc-ad) & a^2-b^2+c^2-d^2 & 2(cd+ab) \\ 2(bd+ac) & 2(cd-ab) & a^2-b^2-c^2+d^2 \end{bmatrix}, \tag{2.1.3}$$

where the unity constraint that must be satisfied is $a^2+b^2+c^2+d^2 = 1$.

2.2 Accelerometers

There are many different types of accelerometers and each has unique characteristics, advantages and disadvantages. The different types are shown in Table 2.1. Regardless of the various types, it is necessary to know that the accelerometer only senses specific force, that is, accelerations resulting from real (i.e., applied, action, or

Techniques	Piezo-electric accelerometers
	Piezo-resistive accelerometers
	Strain gage based accelerometers
	Force rebalanced accelerometers
Output	Charge output
	IEPE output
	Voltage output
	4-20mA output
	Velocity output
Design	Shear type design
	Isolate compression design
	Inverted compression design
	Flexural design
	Courtesy of Honeywell Inc [Honeywell Sensotec 2007]

Table 2.1: Different Types of Accelerometer.

contact) forces; see Jekeli (2000) for a detailed yet concise proof. As for the H764G IMU (used in the Montana survey, in section 6.1, the accelerometers output the velocity increments. As a result, the specific force in the b-frame is given by

$$\vec{a}^b = \delta\vec{v}/\delta t, \tag{2.2.1}$$

where $\delta\vec{v}$ is the incremental velocity over time interval δt.

2.3 Gyroscopes

The term "gyroscope" originates with J.B.L. Foucault, who in 1850, using a spinning disc, demonstrated that the Earth rotates (Jekeli 2000). With the development of the technology, todate, there are many kinds of gyroscopes to measure the rotation of a vehicle with respect to the inertial space. In general, these gyros can be classified into three types, i.e., mechanical gyro, optical gyro, and vibrating gyro, which may be argued as a subset of the first category.

The mechanical gyro is the classical gyro that has a mass spinning steadily with free movable axis (so called gimbal). It functions on the basis of a rapidly spinning mass whose angular momentum provides a well defined direction in inertial space. When the gyro is tilted, gyroscopic effect causes precession (motion orthogonal to the direction of tilt) on the rotating mass axis, hence letting you know the angle moved.

The optical gyro is based on totally different principles. The rotational sensitivity of the optical gyro is based on the Sagnac effect (Jekeli 2000; Post 1967) which occurs when a light beam propagates around a closed path in a frame that rotates with respect to the inertial frame. If the enclosure rotates, the duration between the moment of laser emittance to eventual reception at the same point will be different. In a Ring Laser Gyro (RLG), the laser go-around is achieved by mirrors inside the enclosure. In a Fiber Optic Gyro (FOG), it is done by a coil of optical fiber.

The vibrating gyro is based on the fact that a vibrating element, when rotated, is subjected to the Coriolis effect that causes secondary vibration orthogonal to the original vibrating direction. By sensing the secondary vibration, the rate of turn can be detected.

Because the gyros only sense the rotation rates relative to the inertial space, it is not that straightforward to obtain C_b^i from the gyro outputs as it is to compute the accelerations from the raw accelerometer outputs. The following section introduces a third-order algorithm for computing C_b^i based on the raw gyro outputs.

2.4 Numerical determination of the transform matrix

Due to movement, in general, the b-frame and i-frame are rotating with respect to each other, that is, their relative orientation changes with time. To describe this in terms of rotational transformations, it is necessary to find an expression for the derivative of the transformation with respect to time. In the i-frame, the time derivative of the rotational transformation, C_b^i, is given by:

$$\dot{C}_b^i = \lim_{\delta t \to 0} \frac{C_b^i(\tau + \delta\tau) - C_b^i(\tau)}{\delta\tau}. \tag{2.4.1}$$

The transformation at time $\tau + \delta\tau$ is the result of the transformation up to time τ followed by a small change of the i-frame with respect to the b-frame during the interval, $\delta\tau$. This is expressed as

$$C_b^i(\tau + \delta\tau) = \delta C^i C_b^i(\tau), \tag{2.4.2}$$

where the small-angle transformation can be written as $\delta C^i \approx I - \Psi^i$, and Ψ^i is a skew symmetric matrix of the small rotation angles. As a result, equation (2.4.1) is written by:

$$\dot{C}_b^i = \lim_{\delta t \to 0} \frac{(I - \Psi^i)C_b^i(\tau) - C_b^i(\tau)}{\delta\tau} = \lim_{\delta t \to 0} \frac{\Psi^i}{\delta\tau} C_b^i(\tau) = -\Omega_{bi}^i C_b^i, \tag{2.4.3}$$

where Ω^i_{bi} represents the angular velocity of the i-frame with respect to the b-frame as coordinatized in the i-frame. Considering the following relationship:

$$\Omega^i_{bi} = -\Omega^i_{ib} = -C^i_b \Omega^b_{ib} C^b_i. \tag{2.4.4}$$

the time derivative of the transformation matrix is given by:

$$\dot{C}^i_b = C^i_b \Omega^b_{ib}. \tag{2.4.5}$$

Most inertial navigation algorithms employ quaternions to solve the equation. After substituting equation (2.1.3) into equation (2.4.5), we have the equivalent differential equation in terms of quaternions as shown in equation (2.4.6):

$$\dot{q} = \frac{1}{2} A q, \tag{2.4.6}$$

where A is a 4×4 skew-symmetric matrix of time-dependent angular rates

$$A = \begin{bmatrix} 0 & \omega_1 & \omega_2 & \omega_3 \\ -\omega_1 & 0 & \omega_3 & -\omega_2 \\ -\omega_2 & -\omega_3 & 0 & \omega_1 \\ -\omega_3 & \omega_2 & -\omega_1 & 0 \end{bmatrix} \tag{2.4.7}$$

where ω_1, ω_2, ω_3 are coming from the angular velocity of b-frame with respect to the i-frame, which is give by:

$$\omega^b_{ib} = \begin{bmatrix} \omega_1 \\ \omega_2 \\ \omega_3 \end{bmatrix}. \tag{2.4.8}$$

The integration of q according to equation (2.4.6) is done incrementally over a time interval, such as δt, or a multiple of δt; and, this gives the elements of C^i_b for each step. We note that the digital readout of gyros consists of pulses representing angular increments per unit time. Combining the pulses from all three gyros into a single vector, we define $\delta\theta_l$ as the vector of body-frame angle increments, for the l^{th} time increment, $l = 1, 2, \ldots$, with corresponding time increments, $\delta t = t_l - t_{l-1}$, assumed constant. The data from the gyros are given exactly by:

$$\delta\theta_l = \int_{\delta t} \omega^b_{ib}(t) dt \tag{2.4.9}$$

To reduce the coning error in the strapdown systems, a third-order algorithm is used here. Jekeli (2001) proved that the third-order Runge-Kutta algorithm requires that the function being integrated is evaluated at either end of the integration interval

and half-way in between. Therefore, in this case the integration interval is twice the data sampling interval, $\Delta t = 2\delta t$. To simplify the notation, the index notation for the frames is dropped here since there is only one objective, and that is to determine the quaternions for the transformation matrix, C_b^i. Therefore, let

$$\omega_{ib}^b(t) = \omega(t), \tag{2.4.10}$$

and assume that over the integration interval, Δt, we may write:

$$\omega(t) = \omega_{l-2} + \dot{\omega}_{l-2}(t - t_{l-2}) + O(\Delta t^2), \qquad |t - t_{l-2}| \leq \Delta t, \tag{2.4.11}$$

where the subscript, l, as before, denotes the evaluation of the true quantity at the corresponding epochs spanning the sampling intervals δt. Substituting equation (2.4.11) into equation (2.4.9) yields for two consecutive sampling epochs:

$$\delta\beta_{l-1} = \int_{t_{l-2}}^{t_{l-1}} \omega(t')dt' = \omega_{l-2}\delta t + \frac{1}{2}\dot{\omega}_{l-2}\delta t^2 + O(\Delta t^3), \tag{2.4.12}$$

$$\delta\beta_l = \int_{t_{l-1}}^{t_l} \omega(t')dt' = \omega_{l-2}\delta t + \frac{3}{2}\dot{\omega}_{l-2}\delta t^2 + O(\Delta t^3). \tag{2.4.13}$$

For each of these sampling epochs, the incremental angle, $\delta\beta_l$, strictly given by equation (2.4.9) is approximated by:

$$\delta\beta_{l-1} = \delta\theta_{l-1} - C_i^b(t_{l-1})\omega_{ii}^i(t_{l-1})\frac{\Delta t}{2} = \delta\theta_{l-1}, \tag{2.4.14}$$

$$\delta\beta_l = \delta\theta_l - C_i^b(t_{l-1})\omega_{ii}^i(t_{l-1})\frac{\Delta t}{2} = \delta\theta_l, \tag{2.4.15}$$

where $\delta\theta_l$ is the vector of output values indicated by the gyros. Note, however, that the evaluation of this term in both cases is at the center of the integration interval, and requires that the quaternions be solved for every epoch, t_l, associated with the sampling interval. The last equalities in equation (2.4.14) and (2.4.15) follow from the fact that the i-frame does not rotate, i.e., $\omega_{ii}^i = 0$.

Solving (2.4.12) and (2.4.13) for ω_{l-2}, and $\dot{\omega}_{l-2}$, it is readily verified that

$$\omega_{l-2} = \frac{1}{2\delta t}(3\delta\beta_{l-1} - \delta\beta_l) + O(\Delta t^2) \tag{2.4.16}$$

and

$$\dot{\omega}_{l-2} = \frac{1}{\delta t^2}(\delta\beta_l - \delta\beta_{l-1}) + O(\Delta t) \tag{2.4.17}$$

Using these expressions in (2.4.11) yields for three consecutive sampling epochs:

$$\begin{aligned}
\omega_{l-2}\Delta t &= 3\delta\beta_{l-1} - \delta\beta_l + O(\Delta t^3) \\
\omega_{l-1}\Delta t &= \delta\beta_{l-1} + \delta\beta_l + O(\Delta t^3) \\
\omega_l\Delta t &= 3\delta\beta_l - \delta\beta_{l-1} + O(\Delta t^3)
\end{aligned} \tag{2.4.18}$$

After neglecting the high order terms, we have the following observed quantities:

$$\begin{aligned}
\hat{\omega}_{l-2}\Delta t &= 3\delta\beta_{l-1} - \delta\beta_l \\
\hat{\omega}_{l-1}\Delta t &= \delta\beta_{l-1} + \delta\beta_l \\
\hat{\omega}_l\Delta t &= 3\delta\beta_l - \delta\beta_{l-1}
\end{aligned} \tag{2.4.19}$$

The recursive algorithm for the quaternions is given by:

$$\hat{q}_l = \left[I + \frac{1}{12}(\hat{B}_l + 4\hat{B}_{l-1} + \hat{B}_{l-2}) + \frac{1}{12}(I + \frac{1}{4}\hat{B}_l)\hat{B}_{l-1}\hat{B}_{l-2} + \frac{1}{12}\hat{B}_l(\hat{B}_{l-1} - \frac{1}{2}\hat{B}_{l-2}) \right] \hat{q}_{l-2} \tag{2.4.20}$$

where the elements of $\hat{B}_{l-2}$, $\hat{B}_{l-1}$, $\hat{B}_l$ now are, respectively, the components of the vectors defined by equation (2.4.19), i.e.,

$$\hat{B}_{l-2} = \begin{bmatrix}
0 & 3(\delta\beta_1)_{l-1} - (\delta\beta_1)_l & 3(\delta\beta_2)_{l-1} - (\delta\beta_2)_l & 3(\delta\beta_3)_{l-1} - (\delta\beta_3)_l \\
-3(\delta\beta_1)_{l-1} + (\delta\beta_1)_l & 0 & 3(\delta\beta_3)_{l-1} - (\delta\beta_3)_l & -3(\delta\beta_2)_{l-1} + (\delta\beta_2)_l \\
-3(\delta\beta_2)_{l-1} + (\delta\beta_2)_l & -3(\delta\beta_3)_{l-1} + (\delta\beta_3)_l & 0 & 3(\delta\beta_1)_{l-1} - (\delta\beta_1)_l \\
-3(\delta\beta_3)_{l-1} + (\delta\beta_3)_l & 3(\delta\beta_2)_{l-1} - (\delta\beta_2)_l & -3(\delta\beta_1)_{l-1} + (\delta\beta_1)_l & 0
\end{bmatrix} \tag{2.4.21}$$

$$\hat{B}_{l-1} = \begin{bmatrix}
0 & (\delta\beta_1)_{l-1} + (\delta\beta_1)_l & (\delta\beta_2)_{l-1} + (\delta\beta_2)_l & (\delta\beta_3)_{l-1} + (\delta\beta_3)_l \\
-(\delta\beta_1)_{l-1} - (\delta\beta_1)_l & 0 & (\delta\beta_3)_{l-1} + (\delta\beta_3)_l & -(\delta\beta_2)_{l-1} - (\delta\beta_2)_l \\
-(\delta\beta_2)_{l-1} - (\delta\beta_2)_l & -(\delta\beta_3)_{l-1} - (\delta\beta_3)_l & 0 & (\delta\beta_1)_{l-1} + (\delta\beta_1)_l \\
-(\delta\beta_3)_{l-1} - (\delta\beta_3)_l & (\delta\beta_2)_{l-1} + (\delta\beta_2)_l & -(\delta\beta_1)_{l-1} - (\delta\beta_1)_l & 0
\end{bmatrix} \tag{2.4.22}$$

$$\hat{B}_l = \begin{bmatrix}
0 & 3(\delta\beta_1)_l - (\delta\beta_1)_{l-1} & 3(\delta\beta_2)_l - (\delta\beta_2)_{l-1} & 3(\delta\beta_3)_l - (\delta\beta_3)_{l-1} \\
-3(\delta\beta_1)_l + (\delta\beta_1)_{l-1} & 0 & 3(\delta\beta_3)_l - (\delta\beta_3)_{l-1} & -3(\delta\beta_2)_l + (\delta\beta_2)_{l-1} \\
-3(\delta\beta_2)_l + (\delta\beta_2)_{l-1} & -3(\delta\beta_3)_l + (\delta\beta_3)_{l-1} & 0 & 3(\delta\beta_1)_l - (\delta\beta_1)_{l-1} \\
-3(\delta\beta_3)_l + (\delta\beta_3)_{l-1} & 3(\delta\beta_2)_l - (\delta\beta_2)_{l-1} & -3(\delta\beta_1)_l + (\delta\beta_1)_{l-1} & 0
\end{bmatrix} \tag{2.4.23}$$

The initial quaternions (a_0, b_0, c_0, d_0) are needed to solve equation (2.4.20). One way to obtain the initial quaternions is to use the initial attitude angles, roll (η_0), pitch (χ_0), and yaw (α_0), which may be obtained from the initial alignment. The initial transformation matrix from b-frame to n-frame, C_b^n, is computed by:

$$C_b^n = R_3(-\alpha_0)R_2(-\chi_0)R_1(-\eta_0)$$

$$= \begin{bmatrix} \cos\alpha_0\cos\chi_0 & \cos\alpha_0\sin\chi_0\sin\eta_0 - \sin\alpha_0\cos\eta_0 & \cos\alpha_0\sin\chi_0\cos\eta_0 + \sin\alpha_0\sin\eta_0 \\ \sin\alpha_0\cos\chi_0 & \sin\alpha_0\sin\chi_0\sin\eta_0 + \cos\alpha_0\cos\eta_0 & \sin\alpha_0\sin\chi_0\cos\eta_0 - \cos\alpha_0\sin\eta_0 \\ -\sin\chi_0 & \cos\chi_0\sin\eta_0 & \cos\chi_0\cos\eta_0 \end{bmatrix} \tag{2.4.24}$$

Then the initial transformation matrix C_b^i is given by:

$$C_b^i = C_n^i C_b^n \tag{2.4.25}$$

where $C_n^i = C_e^i C_n^e$,

$$C_e^i = \begin{bmatrix} \cos(\omega_E t) & -\sin(\omega_E t) & 0 \\ \sin(\omega_E t) & \cos(\omega_E t) & 0 \\ 0 & 0 & 1 \end{bmatrix}, \tag{2.4.26}$$

where ω_E is the mean Earth rotation rate, and

$$C_n^e = \begin{bmatrix} -\sin\phi\cos\lambda & -\sin\lambda & -\cos\phi\cos\lambda \\ -\sin\phi\sin\lambda & \cos\lambda & -\cos\phi\sin\lambda \\ \cos\phi & 0 & -\sin\phi \end{bmatrix}. \tag{2.4.27}$$

Finally, the initial quaternions are given by:

$$\begin{aligned} a_0 &= \tfrac{1}{2}\left(1 + (C_b^i)_{1,1} + (C_b^i)_{2,2} + (C_b^i)_{3,3}\right)^{\frac{1}{2}}; \\ b_0 &= \tfrac{1}{4a_0}\left((C_b^i)_{2,3} - (C_b^i)_{3,2}\right); \\ c_0 &= \tfrac{1}{4a_0}\left((C_b^i)_{3,1} - (C_b^i)_{1,3}\right); \\ d_0 &= \tfrac{1}{4a_0}\left((C_b^i)_{1,2} - (C_b^i)_{2,1}\right). \end{aligned} \tag{2.4.28}$$

Furthermore, in each step, the quaternions are normalized to ensure the unity constraint. Then the transformation matrix C_b^i at any epoch is obtained by use of the quaternions through equation (2.1.3). The position and velocity are computed by integrating the accelerations as shown in the following section.

2.5 Numerical integration of navigation equations

The navigation equation in the i-frame is given by:

$$\frac{d}{dt}\dot{x}^i = C_b^i a^b + f(x^i, g^i) \tag{2.5.1}$$

where

$$\begin{aligned} f(x^i, g^i) &= C_n^i g^n = C_n^i \delta\overline{g}^n + C_n^i(\gamma^n + C_i^n \Omega_{ie}^i \Omega_{ie}^i x^i) \\ &\approx C_n^i \gamma^n + \Omega_{ie}^i \Omega_{ie}^i x^i \end{aligned} \tag{2.5.2}$$

γ^n is the normal gravity in the local north, east, and down frame (n-frame), Ω_{ie}^i is the rotation matrix of the Earth with respect to the inertial frame in the i-frame, x^i is the position vector in the i-frame, $\delta\overline{g}^n$ is the gravity disturbances in the n-frame; at this stage, usually it is not available to the users. So it is neglected in the free inertial navigation equation. Then the velocity increment in the i-frame is given by:

$$\Delta\dot{x}^i = \int_{\Delta t} C_b^i(t') a^b(t') dt' + f(x^i, \dot{x}^i, C_i^n, \Omega_{ie}^i, g^i)\Delta t. \tag{2.5.3}$$

The accelerometer output data arrive in the form of velocity increments, or pulses, that capture the time history of the acceleration over the sampling interval. Thus, these increments are expressed exactly in terms of the body-frame acceleration as:

$$\delta v_l^b = \int_{t_{l-1}}^{t_l} a^b(t') dt'. \tag{2.5.4}$$

Following the same procedure of deriving the angular increments, the integration of the linear velocity is given by:

$$\begin{aligned} &\hat{v}_l^i = \hat{v}_{l-2}^i + \tfrac{1}{6}\Big(\hat{C}_b^i(l-2)(3\delta v_{l-1}^b - \delta v_l^b) + 4\hat{C}_b^i(l-1)(\delta v_{l-1}^b + \delta v_l^b)\hat{C}_b^i(l)(3\delta v_l^b - \delta v_{l-1}^b)\Big) \\ &+ \hat{f}(x^i, C_i^n, \Omega_{ie}^i, g^i)_{t=t_{l-2}}\Delta t. \end{aligned} \tag{2.5.5}$$

Note: two separate iterations (with two sets of initial values) are required to obtain estimates at even and odd multiples of δt. With deliberate interlacing of estimates the term, $\hat{f}(x^i, C_i^n, \Omega_{ie}^i, g^i)$ could also be evaluated at $t = t_{l-1}$, with potential improvement in the integration accuracy. Finally, the positions can be obtained from the velocities:

$$\hat{x}^i = \hat{x}_{l-2}^i + \hat{\dot{x}}_{l-1}^i \Delta t \quad \text{Set } \hat{\dot{x}}_{l-1}^i = (\hat{v}_l^i + \hat{v}_{l-2}^i)/2. \tag{2.5.6}$$

To test the above free INS navigation algorithm, sets of INS data collected by a ground vehicle are processed. The IMU are mounted firmly in a ground vehicle, which also has independently working GPS units. The data sets were collected in southwestern Montana (see Chapter 6, and Jekeli and Li 2006 for more details of the system setup and data collection). One set of the free INS navigation solution collected along State Route 43(SR43) on June 15 2005 is shown by the solid(red) lines in Figures 2.1 to 2.6.

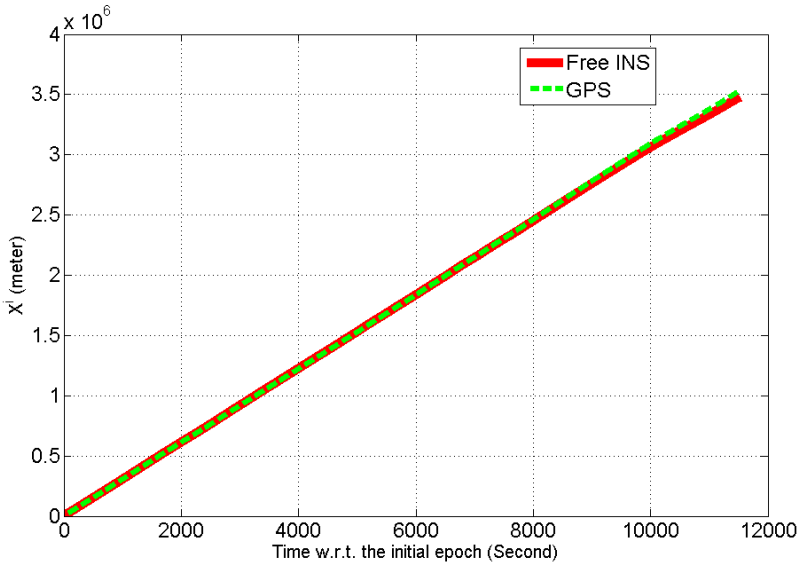

Figure 2.1: The relative X-axis coordinates of the free INS navigation solution in the i-frame

The dashed(green) lines in Figures 2.1 to 2.6 are the GPS navigation solutions, which are presumably more accurate than the free INS navigation solutions. The large discrepancies between these two solutions are mainly due to the IMU errors. And from these figures, it is clear that these IMU errors are accumulative (the differences of the navigation solutions are getting larger with time). Therefore, these IMU errors have to be properly handled and well determined in order to obtain the gravity disturbance estimates from the INS/GPS system. In Chapter 3, the relative long wave-length component of the IMU errors will be estimated by the Two-stage Adaptive Extended Kalman Filter. The high frequency component of the IMU errors will be reduced by the B-spline smoother in Chapter 5.

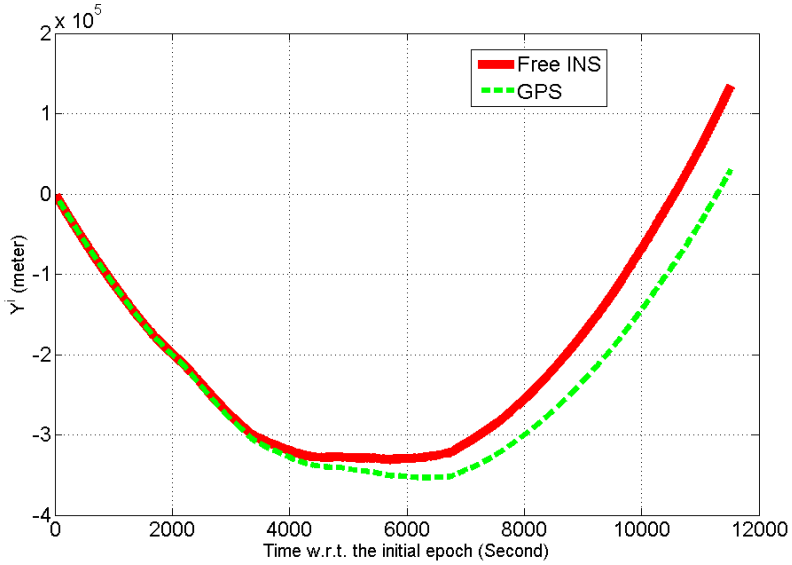

Figure 2.2: The relative Y-axis coordinates of the free INS navigation solution in the i-frame

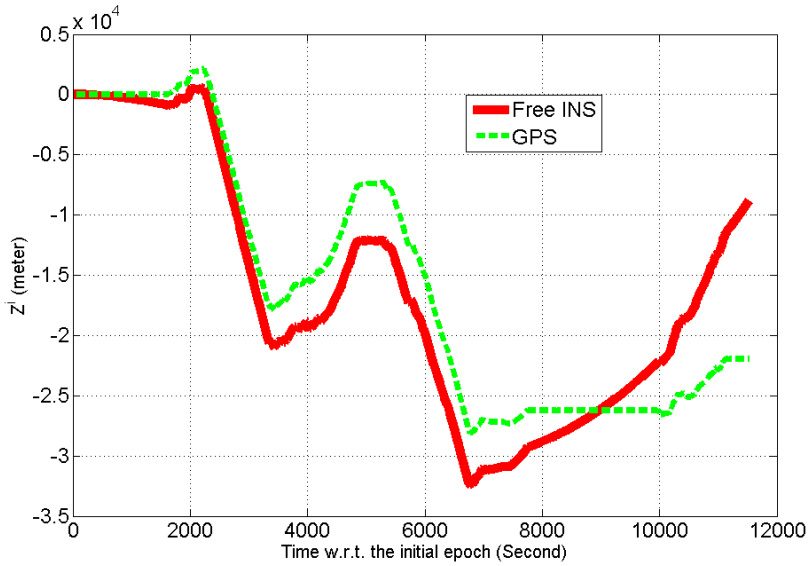

Figure 2.3: The relative Z-axis coordinates of the free INS navigation solution in the i-frame

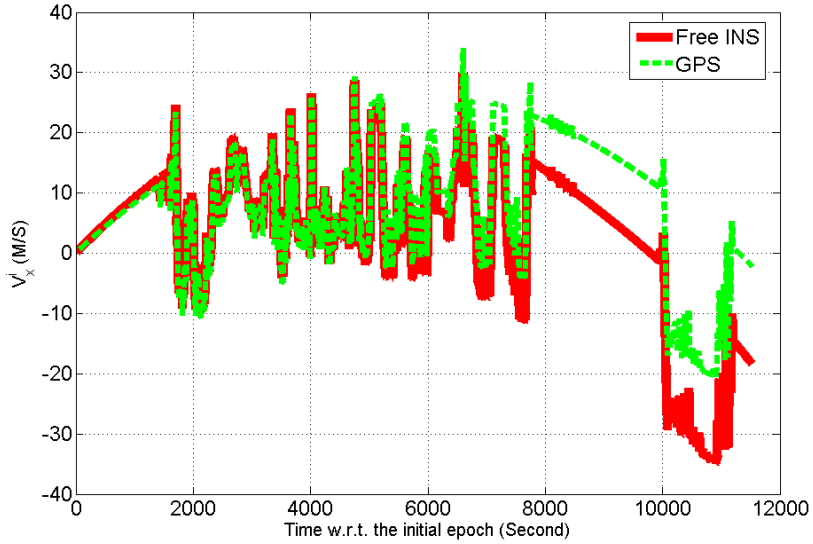

Figure 2.4: The relative X-axis velocities of the free INS navigation solution in the i-frame.

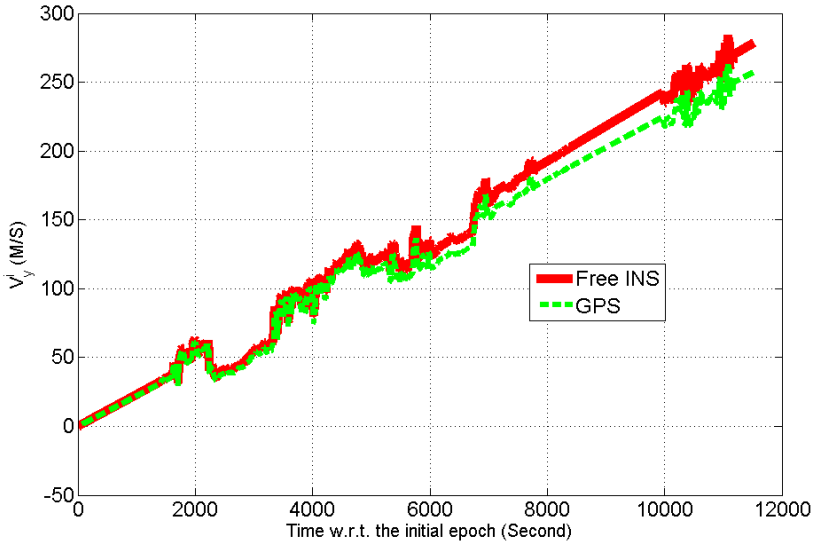

Figure 2.5: The relative Y-axis velocities of the free INS navigation solution in the i-frame.

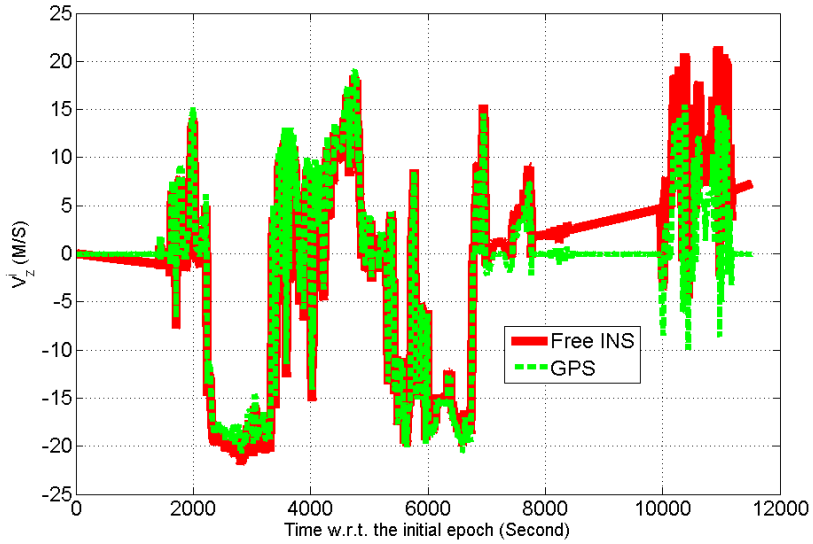

Figure 2.6: The relative Z-axis velocities of the free INS navigation solution in the i-frame.

CHAPTER 3

SINS/DGPS INTEGRATION

As shown in the previous chapter, the differences between INS and GPS navigation systematically increase with time. This is due to the accumulation of errors of the free inertial navigation system, since GPS errors are generally bounded. The long wavelength IMU errors such as bias and scale errors cannot be averaged out and are integrated with respect to time. These errors should be reduced in order to obtain accurate dynamic accelerations and to yield better navigation solutions.

On the other hand, the GPS errors such as ionospheric delay, tropospheric delay, and multipath effects, etc. have high frequency characteristics in the kinematic scenario. Moreover, as is well known, the GPS solution relies on the availability of continuous GPS satellite signals. There may be data gaps in the positioning results due to various reasons in practical operations. However, the INS system does not rely on any external signals. It can always deliver a position solution regardless where the system is.

Considering the complimentary properties of the GPS and INS, an integration algorithm should be applied to yield continuous and accurate position solutions, and to provide the estimates of the INS errors.

3.1 Introduction

Combining the short-term stability of INS and the long-term accuracy of GPS offers many practical advantages. For instance, the positioning gaps in the GPS solution can be fixed, and the INS systematic errors may be well estimated. An appropriate and efficient integration scheme should be used in order to achieve these objectives. In general, the integration can be classified into two types. One is known as tightly-coupled system where all the INS and GPS raw observables are processed simultaneously and optimally to enhance the performances of each individual sensor component, hence avoiding the loss of information and cross correlations among the position estimates. The main advantage relies on the fact that the measurements are

uncorrelated. The other is called the loosely-coupled system where GPS solutions are fed back in an aiding capacity to improve the utility of the performances of INS, but both GPS and INS still have their own individual data processing algorithm (Jekeli 2001). This is by far a simpler approach because it is easier to manipulate and requires minimum modification for customized applications. Wei and Schwarz (1990) showed that, in practice, there is very little difference in the accuracy of the results between these two integration methods. Considering the computational efficiency, the following work is done in the loosely-coupled mode.

Over the decades, many algorithms have been applied to blend the GPS and INS solutions, such as the well known Kalman Filter, Neural Network (Wang et al. 2006; Kaygisiz et al. 2003), Artificial Intelligence/Fuzzy Logic (EI-Gizawy et al. 2004; Jwo and Huang, 2005; Sasiadek et al. 2000), and Particle Filters (Gustafsson et al.). Among them, the Kalman Filter is the mostly common used technique in practice. As pointed out by Wang et al. (2006), it still remains at the forefront of INS/GPS integration, because other techniques either are not ideal or demand artificial experience and complicated training procedures. Of course, the Kalman Filter also has limitations. The main drawback is that it only works well under the predefined models. For instance, the system dynamics of the driving and measurement processes need to be completely known. To overcome these limitations, the Adaptive Kalman Filter (AKF, Myers and Tapley 1976; Mohammed and Schwarz 1999; Hide et. al., 2003), Unscented Kalman Filter (UKF, Julier and Uhlmann 2004; Wan and Merwe 2000), and Two-stage Adaptive Extended Kalman Filter (TAEKF, Ignagni 1981, 1990; Kim et al. 2006) have been investigated. From the computational point of view, the TAEKF is selected, because this filter gives explicit expressions of the IMU errors by decoupling the conventional system into a bias free estimator and a bias estimator. We will see that this configuration offers much flexibility for the adaptive schemes later on.

3.2 Error Dynamics Equations

As is well known, the Kalman Filter is a model based system. It works only well under certain predefined models. So it is very important to correctly describe the INS/GPS system via precise mathematical models. The INS/GPS integration system is a rather complex system, especially the INS, which is an assemblage of mechanical and/or optical inertial sensors. Each component responds to physical and systematic effects extraneous to the actual desired navigation function, as well as to internal random errors of various characters and consequences. The error dynamics equations describe how the sensor errors affect the position and velocity of the system. From Chapter 2, we know the position and velocity of the INS solution are based on

the integration of the accelerations. So it will be easier to describe the error effects in the acceleration equation. From Newton's second law of motion in the inertial (i-) frame, we have the following equation:

$$\ddot{\vec{x}}^i = \vec{a}^i + \vec{g}^i, \tag{3.2.1}$$

where $\ddot{\vec{x}}^i$ is the kinematic acceleration, $\vec{a}^i$ is the specific force measured by the accelerometer, and $\vec{g}^i$ is the gravitational acceleration due to the attraction of the Earth. All quantities are expressed in the i-frame. By applying the perturbation technique, we have the following equation (Jekeli 2000):

$$\frac{d}{dt}\delta\dot{x}^i = \Gamma^i \delta x^i + \delta a^i + \delta g^i, \tag{3.2.2}$$

where

$$\delta a^i = C_b^i \delta a^b + a^i \times \Psi^i, \tag{3.2.3}$$

δa^b is the accelerometer error,
Ψ^i is the orientation error and is given by equation (3.2.4).

$$\Psi^i = -C_b^i \delta\omega_{ib}^b, \tag{3.2.4}$$

$\delta\omega_{ib}^b$ is the gyro error.

As a result, equation (3.2.2) can be written as:

$$\frac{d}{dt}\delta\dot{x}^i = \Gamma^i \delta x^i + C_b^i \delta a^b - a^i \times C_b^i \delta\omega_{ib}^b + \delta g^i \tag{3.2.5}$$

$$\frac{d}{dt}\delta x^i = \delta\dot{x}^i \tag{3.2.6}$$

If we combine equations (3.2.4)-(3.2.6), then the error dynamics may be cast in matrix form as:

$$\frac{d}{dt}\begin{bmatrix} \delta x^i \\ \delta\dot{x}^i \\ \Psi^i \end{bmatrix} = \begin{bmatrix} 0 & I & 0 \\ \Gamma^i & 0 & [a^i\times] \\ 0 & 0 & 0 \end{bmatrix}\begin{bmatrix} \delta x^i \\ \delta\dot{x}^i \\ \Psi^i \end{bmatrix} + \begin{bmatrix} 0 & 0 & 0 \\ I & C_b^i & 0 \\ 0 & 0 & -C_b^i \end{bmatrix}\begin{bmatrix} \delta g^i \\ \delta a^b \\ \delta w_{ib}^b \end{bmatrix} \tag{3.2.7}$$

where

$$[a^i\times] = \begin{bmatrix} 0 & -a_3^i & a_2^i \\ a_3^i & 0 & -a_1^i \\ -a_2^i & a_1^i & 0 \end{bmatrix} \tag{3.2.8}$$

$$\Gamma^i = \frac{\partial \vec{g}^i}{\partial \vec{x}^i} \tag{3.2.9}$$

$$\vec{g}^i = -g^i \begin{bmatrix} \frac{x}{r} \\ \frac{y}{r} \\ \frac{z}{r} \end{bmatrix} \approx -\frac{KM}{r^2} \begin{bmatrix} \frac{x}{r} \\ \frac{y}{r} \\ \frac{z}{r} \end{bmatrix} \tag{3.2.10}$$

$$KM = 3.986 \times 10^{14} m^3/s^2 \quad r = \sqrt{x^2 + y^2 + z^2} \tag{3.2.11}$$

$$\frac{\partial \vec{g}^i}{\partial \vec{x}^i} = KM \begin{bmatrix} \frac{\partial}{\partial x}\left(\frac{x}{r^3}\right) & \frac{\partial}{\partial y}\left(\frac{x}{r^3}\right) & \frac{\partial}{\partial z}\left(\frac{x}{r^3}\right) \\ \frac{\partial}{\partial x}\left(\frac{y}{r^3}\right) & \frac{\partial}{\partial y}\left(\frac{y}{r^3}\right) & \frac{\partial}{\partial z}\left(\frac{y}{r^3}\right) \\ \frac{\partial}{\partial x}\left(\frac{z}{r^3}\right) & \frac{\partial}{\partial y}\left(\frac{z}{r^3}\right) & \frac{\partial}{\partial z}\left(\frac{z}{r^3}\right) \end{bmatrix} \tag{3.2.12}$$

$$\begin{array}{lll} \frac{\partial}{\partial x}\left(\frac{x}{r^3}\right) = \frac{1}{r^3} - 3\frac{x^2}{r^5} & \frac{\partial}{\partial y}\left(\frac{x}{r^3}\right) = -3\frac{xy}{r^5} & \frac{\partial}{\partial z}\left(\frac{x}{r^3}\right) = -3\frac{xz}{r^5} \\ \frac{\partial}{\partial x}\left(\frac{y}{r^3}\right) = -3\frac{xy}{r^5} & \frac{\partial}{\partial y}\left(\frac{y}{r^3}\right) = \frac{1}{r^3} - 3\frac{y^2}{r^5} & \frac{\partial}{\partial z}\left(\frac{y}{r^3}\right) = -3\frac{yz}{r^5} \\ \frac{\partial}{\partial x}\left(\frac{z}{r^3}\right) = -3\frac{xz}{r^5} & \frac{\partial}{\partial y}\left(\frac{z}{r^3}\right) = -3\frac{yz}{r^5} & \frac{\partial}{\partial z}\left(\frac{z}{r^3}\right) = -\frac{2}{r^3} + 3\frac{x^2+y^2}{r^5} \end{array}$$

and

$$\delta a^b = b_a + \text{diag}\{a^b\} k_a + \varepsilon_a, \tag{3.2.13}$$

$$\delta w_{ib}^b = b_g + \text{diag}\{w_{ib}^b\} k_g + \varepsilon_g, \tag{3.2.14}$$

$$\text{diag}\{w_{ib}^b\} = [w_{ib}^b]$$

In equations (3.2.13) and (3.2.14),

b_a is the accelerometer bias,
k_a is the accelerometer scale error,
b_g is the gyro bias,
k_g is the gyro scale error.

The evolution of the above sensor errors can be expressed as follows:

$$\dot{b}_a = \text{diag}\{C_{ab}\} k_a + \eta_{ab}, \tag{3.2.15}$$

$$\dot{b}_g = \text{diag}\{C_{gb}\} k_g + \eta_{gb}, \tag{3.2.16}$$

$$\dot{k}_a = \text{diag}\{C_{ak}\} k_a + \eta_{ak}, \tag{3.2.17}$$

$$\dot{k}_g = \text{diag}\{C_{gk}\} k_g + \eta_{gk}, \tag{3.2.18}$$

which can be represented as a random constant, a first-order Gauss-Markov, or a random walk processes according to the choice of the parameters, C_{ab}, η_{ab}, $C_{gb} \ldots \eta_{gk}$ (Shin 2005). In general, the noise affecting inertial sensors contains two parts: a low frequency component and a high frequency component, where the high frequency part plays a dominate role, which makes the SNR very poor. For instance, it can be in the range of -20db (El-Sheimy et. al. 2004). Both noise components are combined together and affect the inertial sensor measurement accuracy. As pointed

out by Nassar (2003), directly modeling of these noises is not possible in practice. As a result, the effect of IMU measurement noises is usually decreased by employing cascade algorithms. First, the high frequency noise is reduced by de-noising and/or smoothing techniques such as wavelet de-noising and B-spline smoothing. Second, the constant part is estimated through a Kalman filter by deterministic models.

It is noted that the relatively short wavelength gravity data are not available at this stage. Therefore, it induces errors in the observed quantities in the loosely-coupled system. If the IMU error models are defined by higher-order differential equations, the short wavelength gravity induced observation errors tend to be absorbed by the IMU error models. Consequently, the filter generates inaccurate IMU error estimates. To avoid this phenomenon, a low-order differential model, a random constant model, is used for equations (3.2.15) to (3.2.18). As a result, the error dynamics equation becomes:

$$\frac{d}{dt}\begin{bmatrix} \delta x^i \\ \delta \dot{x}^i \\ \Psi^i \\ b_a \\ b_g \\ k_a \\ k_g \end{bmatrix} = \begin{bmatrix} 0 & I & 0 & 0 & 0 & 0 & 0 \\ \Gamma^i & 0 & [a^i\times] & C_b^i & 0 & C_b^i[\tilde{a}^b] & 0 \\ 0 & 0 & 0 & 0 & -C_b^i & 0 & -C_b^i[\omega_{ib}^b] \\ 0 & 0 & 0 & 0 & 0 & 0 & 0 \\ 0 & 0 & 0 & 0 & 0 & 0 & 0 \\ 0 & 0 & 0 & 0 & 0 & 0 & 0 \\ 0 & 0 & 0 & 0 & 0 & 0 & 0 \end{bmatrix} \begin{bmatrix} \delta x^i \\ \delta \dot{x}^i \\ \Psi^i \\ b_a \\ b_g \\ k_a \\ k_g \end{bmatrix} + \begin{bmatrix} I & 0 & 0 & 0 & 0 & 0 & 0 \\ 0 & C_b^i & 0 & 0 & 0 & 0 & 0 \\ 0 & 0 & -C_b^i & 0 & 0 & 0 & 0 \\ 0 & 0 & 0 & I & 0 & 0 & 0 \\ 0 & 0 & 0 & 0 & I & 0 & 0 \\ 0 & 0 & 0 & 0 & 0 & I & 0 \\ 0 & 0 & 0 & 0 & 0 & 0 & I \end{bmatrix} \begin{bmatrix} \varepsilon_1 \\ \varepsilon_2 \\ \varepsilon_3 \\ \varepsilon_4 \\ \varepsilon_5 \\ \varepsilon_6 \\ \varepsilon_7 \end{bmatrix} \tag{3.2.19}$$

Or, it can be written in short notation for convenience of the following derivations:

$$\dot{X}(t) = F(t)X(t) + G(t)\Omega(t) \tag{3.2.20}$$

where $X = (\ \delta x^i \quad \delta \dot{x}^i \quad \Psi^i \quad b_a \quad b_g \quad k_a \quad k_g\ )^T$
$E\left\{\Omega(t)\Omega(t)^T\right\} = Q_\Omega(t)\delta(t-\tau)$.

Considering the high sampling rate of the SINS system, the above continuous time system is to be transformed into the following discrete time form:

$$X_k = \Phi_{k,k-1}X_k + w_k \tag{3.2.21}$$

where $\Phi_{k,k-1} = I + F\Delta t$ is the transformation matrix and $w_k \sim (0, Q_k)$. By taking the navigation differences between INS and GPS, we can also establish an observation

equation, which is directly related to the error state vector as in equation (3.2.22).

$$z_k = H_k X_k + v_k \tag{3.2.22}$$

where
$z_k := \begin{bmatrix} \delta x^i \\ \delta \dot{x}^i \end{bmatrix}_k = \begin{bmatrix} x^i_{\text{INS}} - x^i_{\text{GPS}} \\ \dot{x}^i_{\text{INS}} - \dot{x}^i_{\text{GPS}} \end{bmatrix}_k$
$H := \begin{bmatrix} I & 0 & 0 & 0 & 0 & 0 & 0 \\ 0 & I & 0 & 0 & 0 & 0 & 0 \end{bmatrix}_{n \times m}$
$v_k \sim (0, R_k)$.

3.3 Kalman Filters

The Minimum Mean Squared Error (MMSE) estimator of X_k from equation (3.2.21) and equation (3.2.22) can be obtained by the Kalman Filter (Kalman 1960), which can also be derived as in the following. Suppose the initial condition is given by:

$$\hat{X}_0 = X_0 + e_0 \tag{3.3.1}$$

At the first epoch, the state space transition equation (3.2.21) reads as:

$$X_1 = \Phi_{1,0} X_0 + w_1 \tag{3.3.2}$$

And the observation equation at the first epoch is given by:

$$z_1 = H_1 X_1 + v_1 \tag{3.3.3}$$

where

$$\begin{bmatrix} v_1 \\ w_1 \\ e_0 \end{bmatrix} \sim \left(\begin{bmatrix} 0 \\ 0 \\ 0 \end{bmatrix}, \begin{bmatrix} R_1 & 0 & 0 \\ 0 & Q_1 & 0 \\ 0 & 0 & P_0 \end{bmatrix} \right) \tag{3.3.4}$$

i.e., the errors are zero mean and uncorrelated noises.

Without using the observation information, equation (3.3.1) and (3.3.2) offer *a priori* estimation of X_1:

$$\hat{X}_1^- := \Phi_{1,0} \hat{X}_0 = \Phi_{1,0} X_0 + \Phi_{1,0} e_0 = X_1 - w_1 + \Phi_{1,0} e_0 = X_1 - (w_1 - \Phi_{1,0} e_0) \tag{3.3.5}$$

$$\implies X_1 = \hat{X}_1^- + (w_1 - \Phi_{1,0} e_0) \tag{3.3.6}$$

Substituting equation (3.3.6) into equation (3.3.3), we have:

$$z_1 - H_1\hat{X}_1^- = v_1 + H_1(w_1 - \Phi_{1,0}e_0) \tag{3.3.7}$$

This is the well known condition equation in the geodetic literature, the LEast Sum of Squares, LESS, solution is given by:

$$\begin{aligned}\begin{bmatrix} \tilde{v}_1 \\ \tilde{w}_1 \\ \tilde{e}_0 \end{bmatrix} &= \begin{bmatrix} R_1 & 0 & 0 \\ 0 & Q_1 & 0 \\ 0 & 0 & P_0 \end{bmatrix} \begin{bmatrix} I \\ H_1^T \\ -\Phi_{1,0}^T H_1^T \end{bmatrix} \\ &\quad \times \left[R_1 + H_1(Q_1 + \Phi_{1,0}P_0\Phi_{1,0}^T)H_1^T\right]^{-1}(z_1 - H_1\hat{X}_1^-)\end{aligned} \tag{3.3.8}$$

$\Longrightarrow$

$$\begin{aligned}\hat{X}_1 &= \hat{X}_1^- + (\tilde{w}_1 - \Phi_{1,0}\tilde{e}_0) \\ &= \hat{X}_1^- + (Q_1 + \Phi_{1,0}P_0\Phi_{1,0}^T)H_1^T\left[R_1 + H_1(Q_1 + \Phi_{1,0}P_0\Phi_{1,0}^T)H_1^T\right]^{-1}(z_1 - H_1\hat{X}_1^-)\end{aligned} \tag{3.3.9}$$

where $(Q_1 + \Phi_{1,0}P_0\Phi_{1,0}^T)H_1^T\left[R_1 + H_1(Q_1 + \Phi_{1,0}P_0\Phi_{1,0}^T)H_1^T\right]^{-1}$ is the Kalman gain matrix K_1. $(z_1 - H_1\hat{X}_1^-)$ is usually referred to as the innovation matrix. The expectation of the MMSE estimate $\hat{X}_1$ is given by:

$$\begin{aligned}E\left\{\hat{X}_1\right\} &= E\left\{\hat{X}_1^-\right\} + K_1 E\left\{z_1 - H_1\hat{X}_1^-\right\} \\ &= E\left\{X_1\right\} + K_1\left(H_1 E\left\{X_1\right\} - H_1 E\left\{X_1\right\}\right) \\ &= E\left\{X_1\right\}\end{aligned} \tag{3.3.10}$$

So we can see that $\hat{X}_1$ is also weakly unbiased, in the sense that $E\left\{\hat{X}_1 - X_1\right\}$ is a null vector. The dispersion matrix of $\hat{X}_1$ is given by:

$$\begin{aligned}P_1 :=\ & D\left\{\hat{X}_1 - X_1\right\} = D\left\{(\hat{X}_1 - \hat{X}_1^-) - (X_1 - \hat{X}_1^-)\right\} \\ =\ & D\left\{\hat{X}_1 - \hat{X}_1^-\right\} - C\left\{(\hat{X}_1 - \hat{X}_1^-), (X_1 - \hat{X}_1^-)\right\} \\ & -C\left\{(X_1 - \hat{X}_1^-), (\hat{X}_1 - \hat{X}_1^-)\right\} + D\left\{X_1 - \hat{X}_1^-\right\}\end{aligned} \tag{3.3.11}$$

where

$$\begin{aligned}D\left\{X_1 - \hat{X}_1^-\right\} &= K_1 D\left\{z_1 - H_1\hat{X}_1^-\right\}K_1^T \\ &= K_1\left[R_1 + H_1(Q_1 + \Phi_{1,0}P_0\Phi_{1,0}^T)H_1^T\right]K_1^T \\ &= K_1 H_1(Q_1 + \Phi_{1,0}P_0\Phi_{1,0}^T)\end{aligned} \tag{3.3.12}$$

$$
\begin{aligned}
C\left\{(\hat{X}_1 - \hat{X}_1^-), (X_1 - \hat{X}_1^-)\right\} &= K_1 C\left\{R_1 + H_1(w_1 - \Phi_{1,0}e_1), (w_1 - \Phi_{1,0}e_0)\right\} \\
&= K_1 H_1 (Q_1 + \Phi_{1,0} P_0 \Phi_{1,0}^T) \\
&= C\left\{(X_1 - \hat{X}_1^-), (\hat{X}_1 - \hat{X}_1^-)\right\}
\end{aligned}
\tag{3.3.13}
$$

$$
P_0 := D\left\{X_1 - \hat{X}_1^-\right\} = D\left\{w_1 - \Phi_{1,0}e_1\right\} = Q_1 + \Phi_{1,0} P_0 \Phi_{1,0}^T \tag{3.3.14}
$$

Substituting equations (3.3.12)-(3.3.14) into equation (3.3.11), we have:

$$
P_1 := (I_m - K_1 H_1) P_1^- (I_m - K_1 H_1)^T + K_1 R_1 K_1^T \quad \text{if } n \leq m \tag{3.3.15}
$$

So in the next epoch, $\hat{X}_1$ and P_1 can be used as the initial information to obtain the MMSE estimate of $\hat{X}_2$ as well as its dispersion matrix P_2. This establishes the following iteration procedure for solutions at subsequent epochs. That is, we have the following algorithm:

Prediction:

$$
\hat{X}_k^- = \Phi_{k,k-1} \hat{X}_{k-1} \tag{3.3.16}
$$

$$
\hat{P}_k^- = \Phi_{k,k-1} \hat{P}_{k-1} \Phi_{k,k-1}^T + Q_{k-1} \tag{3.3.17}
$$

where $\hat{X}_k$ denotes the KF estimated state vector;
$\hat{X}_k^-$ is the predicted state vector for the next epoch;
$\hat{P}_k$ is the estimated state covariance matrix;
$\hat{P}_k^-$ is the predicted state covariance matrix.

Update:

$$
K_k = \hat{P}_k^- H_k^T (H_k \hat{P}_k^- H_k^T + R_k)^{-1} \tag{3.3.18}
$$

$$
\hat{X}_k = \hat{X}_k^- + K_k (z_k - H_k \hat{X}_k^-) \tag{3.3.19}
$$

$$
\hat{P}_k = (I - K_k H_k) \hat{P}_k^- \tag{3.3.20}
$$

where K_k is the Kalman gain, which defines the updating weight between measurements and predictions from the system dynamics model.

The innovation sequence is defined as:

$$
d_k = z_k - H_k \hat{X}_k^- \tag{3.3.21}
$$

And the residual sequence is:

$$\varepsilon_k = z_k - H_k \hat{X}_k \tag{3.3.22}$$

Equations (3.3.16) to (3.3.20) represent the well known Kalman algorithm. From equation (3.2.19), we can see that the INS sensor errors and the navigation errors are both included in the system state vector, which requires relatively large matrix inversions. Through transformation of the variance equation, Friedland (1969) decoupled the Kalman Filter into two stages i.e., a bias-free estimator and a bias estimator. This rearrangement avoids dealing with large matrix manipulations. And more importantly it offers explicit expressions of the bias estimation. The decoupling of the bias estimation from the state estimation makes the effect of the bias on the estimation of the navigation errors more readily apparent (Friedland 1969).

Ignagni (1990) showed that the decomposition inherent in Friedland's two-stage estimator follows naturally and directly from the original estimation problem statement by using the familiar notions from the conventional Kalman estimation theory. A relatively simple and straightforward inductive proof is then employed to demonstrate equivalency with a partitioned form of the generalized Kalman estimator. This alternate simplified approach preserves a great deal of insight into the fundamental nature of the solution, and allows certain extensions of the basic idea to be easily recognized. Specifically, by considering that the bias states will undergo some random variation with time, Ignagni (1990) developed the decoupled Kalman estimator for the following system as shown in equations (3.3.23) and (3.3.24).

$$x_k = A_{k-1} x_{k-1} + B_{k-1} b_{k-1} + \xi_k \tag{3.3.23}$$

$$b_k = b_{k-1} + \beta_k \tag{3.3.24}$$

The observation equation is given by:

$$y_k = H_k x_k + C_k b_k + \eta_k \tag{3.3.25}$$

where

$$E\left\{\xi_j \xi_k'\right\} = Q_x \delta_{j,k} \tag{3.3.26}$$

$$E\left\{\beta_j \beta_k'\right\} = Q_b \delta_{j,k} \tag{3.3.27}$$

$$E\left\{\eta_j \eta_k'\right\} = R \delta_{j,k} \tag{3.3.28}$$

$$E\left\{\xi_j \beta_k'\right\} = E\left\{\eta_j \xi_k\right\} = E\left\{\eta_j \beta_k'\right\} = 0 \tag{3.3.29}$$

The decoupled algorithm is given by equations (3.3.30)-(3.3.43).

▶ **Initial condition:**

$\tilde{X}_0$, $\tilde{P}_x(0) = P^*_{x0}$ for the bias free estimator

$U_x(0) = 0$, $M(0) = P_b(0)$, $\hat{b}(0) = 0$ for the bias estimator

▶ **Bias free estimator:**

$$\tilde{X}_k^- = A_{k-1}\tilde{X}_{k-1} \tag{3.3.30}$$

$$\tilde{P}_x^-(k) = A_k\tilde{P}_x(k-1)A_k' + B_kQ_b(k-1)B_k' + Q_X(k) \tag{3.3.31}$$

$$\tilde{K}_x(k) = \tilde{P}_x^-(k)H_k'\left[H_k\tilde{P}_x^-(k)H_k' + R_k\right]^{-1} \tag{3.3.32}$$

$$\tilde{P}_x(k) = \left[I - \tilde{K}_x(k)H_k\right]\tilde{P}_x^-(k) \tag{3.3.33}$$

$$\tilde{X}_k = \tilde{X}_k^- + \tilde{K}_x(k)\left(y_k - H_k\tilde{X}_k^-\right) \tag{3.3.34}$$

▶ **Bias estimator:**

$$\hat{b}_k^- = \hat{b}_{k-1} \tag{3.3.35}$$

$$P_b^-(k) = P_b(k-1) + Q_b(k) \tag{3.3.36}$$

$$K_b(k) = P_b^-(k)S_k'\left[S_kP_b^-(k)S_k' + H_k\tilde{P}_x^-(k)H_k' + R_k\right]^{-1} \tag{3.3.37}$$

$$P_b(k) = [I - K_b(k)S_k]\,P_b^-(k) \tag{3.3.38}$$

$$\hat{b}_k = \hat{b}_k^- + K_b(k)\left[y_k - H_k(k)\tilde{X}_k^-(k) - S_k\tilde{b}_k^-\right] \tag{3.3.39}$$

where S_k is defined by the recursive sequence

$$U_k = A_kV_{k-1} + B_k \tag{3.3.40}$$

$$S_k = H_kU_k + C_k \tag{3.3.41}$$

$$V_k = U_k - \tilde{K}_x(k)S_k \tag{3.3.42}$$

▶ **Compute State estimates:**

$$\hat{X}_k = \tilde{X}_k + V_k\hat{b}_k \tag{3.3.43}$$

To apply the two-stage algorithm into the loosely-coupled INS/GPS integration system, we just need to properly decompose equation (3.2.19) and equation (3.2.20) into equations (3.3.23)-(3.3.25), and let x_k include the position, velocity and orientation error and b_k include the accelerometer and gyro bias and scale error.

3.4 Adaptive methods

Whether it is a one-stage or two-stage algorithm, the implementation of the Kalman filter requires precise *a priori* knowledge of both the dynamic processing noise and the observation noise. Furthermore, these statistics are usually assumed to remain constant in a particular run. However, in kinematic applications, neither the trajectory geometry nor the trajectory dynamics remain constant (Mohamed and Schwarz 1999). Therefore, the stochastic properties of the system vary depending on the vehicle dynamics as well as the observation conditions. Assuming constant covariances of the *a priori* observation noise and the processing noise may cause the accuracy of the estimation to degrade or even cause divergence of the filter.

Considering that the innovation and residual sequences of the Kalman filter are reliable indicators of the filter performance, many adaptive methods have been investigated by online monitoring of the innovation and residual covariance to overcome these limitations. An ideal adaptive Kalman filter would be able to identify the correct stochastic properties without the need for any *a priori* statistics (Hide et. al., 2003). An increment of the elements of Q will increase the Kalman gain, resulting in greater filter dynamics, i.e., a relatively large oscillation of the state estimates; while increasing the values of the elements of R will mean that the measurements are affected more by noise and thus imply less confidence. Since the 1970s, many adaptive approaches have been investigated. For the convenience of implementation, three typical adaptive schemes are considered here.

3.4.1 Maximum Likelihood estimator of Q and R based on innovations.

Under the normal distribution assumption of the filter innovation sequence, Mohamed and Schwarz (1999) derived the Maximum Likelihood estimator of the filter's statistical information matrices as follows:

$$\hat{R}_k = \hat{C}_{d_k} - H_k P_k^- H_k^T \tag{3.4.1}$$

$$\hat{C}_{d_k} = \frac{1}{N}\sum_{j=j_0}^{k} d_k d_k^T, \;\; j_0 = k - N + 1 \tag{3.4.2}$$

and

$$\hat{Q}_k = \frac{1}{N}\sum_{j=j_0}^{k} \Delta X_j \Delta X_j^T + P_k - \Phi_{k,k-1} P_{k-1} \Phi_{k,k-1}^T \tag{3.4.3}$$

where $\Delta X_k = \hat{X}_k - \hat{X}_k^-$ In practice, to guarantee positive definiteness of the variance matrices the following approximations as shown in equations (3.3.4) and (3.4.5) may be used:

$$\hat{R}_k \approx \hat{C}_{d_k} \tag{3.4.4}$$

and

$$\hat{Q}_k \approx \frac{1}{N} \sum_{j=j_0}^{k} \Delta X_j \Delta X_j^T \tag{3.4.5}$$

3.4.2 Processing noise scaling method

The covariance scaling filter is a very simple and efficient extension to the EKF algorithm which applies a scale factor, $S_k \geq 1$, to the predicted covariance, P_k^-. When S_k is greater than 1, this has the effect of giving more weight to the new measurement. The modified covariance prediction equation in the Kalman filter is given by:

$$P_k^- = S_k \left[\Phi P_{k-1} \Phi^T + Q_{k-1} \right] \tag{3.4.6}$$

where Φ is the state transition matrix. This algorithm was used by Hu et al. (2001) where it was used to improve the stochastic modeling for differential pseudo-range GPS positioning (Hide et. al., 2003), where equation (3.4.7) was used to compute the scaling factor.

$$S_k = \frac{d_k^T d_k}{\frac{1}{N} \sum_{j=0}^{N-1} d_{k-N+j}^T d_{k-N+j}} \tag{3.4.7}$$

To improve the stability of the INS/GPS integration by use of the above adaptive method, Hide et. al., (2003) proposed the following:

$$P_k^- = \Phi P_{k-1} \Phi^T + S_k Q_{k-1} \tag{3.4.8}$$

3.4.3 State covariance scaling method

Instead of using equation (3.4.7) to obtain the scaling factor, Kim et al. (2006) proposed a "forgetting factor" λ_k to rescale the predicted state covariance matrix as shown in equations (3.4.9) and (3.4.10).

$$P_k^- = \lambda_k \left[\Phi P_{k-1} \Phi^T + Q_{k-1} \right] \tag{3.4.9}$$

The forgetting factor is generated from the ratio between the calculated and the estimated innovation covariance.

$$\lambda_k = \max\left\{1, \frac{\text{trace}(\overline{C}_k)}{\text{trace}(C_k)}\right\} \tag{3.4.10}$$

where

$$C_k = E\left\{d_k d_k^T\right\} = H_k P_k^- H_k^T + R_k \tag{3.4.11}$$

$$\overline{C}_k = \frac{1}{M-1}\sum_{i=k-M+1}^{k} d_i d_i^T \tag{3.4.12}$$

C_k is the calculated innovation covariance, and $\overline{C}_k$ is the estimated innovation covariance, and M is a window size. The relation between the two innovation covariances is defined as $\overline{C}_k = \lambda_k C_k$. Kim et al. (2006) stated that if R_k remains unchanged, the effects of incomplete information in the dynamics equation can be compensated by an increase in the magnitude of P_k^-.

3.5 Comparison tests and conclusions

All these three adaptive methods can be applied both in the EKF and TEKF systems. For instance, the state covariance scaling method (Kim et al. 2006) is implemented in EKF by equations (3.5.1)-(3.5.8).

Time Update

(1) Project the state ahead

$$\hat{x}_k^- = \Phi_k \hat{x}_{k-1} \tag{3.5.1}$$

(2) Compute the innovation

$$d_k = z_k - h_k(\hat{x}_k^-) \tag{3.5.2}$$

(3) Estimate the innovation covariance

$$\overline{C}_k = \frac{1}{M-1}\sum_{i=k-M+1}^{k} d_i d_i^T \tag{3.5.3}$$

(4) Compute λ_k

$$\lambda_k = \max\left\{1, \frac{\text{trace}(\overline{C}_k)}{\text{trace}(C_k)}\right\} \tag{3.5.4}$$

where $C_k = H_k P_k^- H_k^T + R_k$

(5) Project the error covariance ahead

$$P_k^- = \lambda_k \left[\Phi_{k-1} P_{k-1} \Phi_{k-1}^T + Q_{k-1}\right] \tag{3.5.5}$$

Measurement Update

(1) Compute the Kalman gain

$$\overline{K}_k = P_k^- H_k^T \left[H_k P_k^- H_k^T + R_k\right]^{-1} \tag{3.5.6}$$

(2) Update estimate with measurement

$$\hat{x}_k = \hat{x}_k^- + \overline{K}_k \left[z_k - h_k(\hat{x}_k^-)\right] \tag{3.5.7}$$

(3) Update the error covariance

$$P_k = (I - \overline{K}_k H_k) P_k^- \tag{3.5.8}$$

Correspondingly, this scaling method can also be implemented in TEKF through equations (3.5.9)-(3.5.30).

Bias free estimator:

$$\hat{x}_k^- = \Phi_{k-1} \hat{x}_{k-1} \tag{3.5.9}$$

$$P_k^{x^-} = \lambda_k^x \left[\Phi_{k-1} P_{k-1}^x \Phi_{k-1}^T + Q_{k-1}^x\right] \tag{3.5.10}$$

$$K_k^x = P_k^{x^-} H_k^T \left[H_k P_k^{x^-} H_k^T + R_k\right]^{-1} \tag{3.5.11}$$

$$P_k^x = (I - K_k^x) H_k P_k^{x^-} \tag{3.5.12}$$

$$d_k^x = z_k - h_k(\hat{x}_k^-) \tag{3.5.13}$$

$$\hat{x}_k = \hat{x}_k^- + K_k^x d_k^x \tag{3.5.14}$$

$$C_k^x = H_k P_k^{x^-} H_k^T + R_k \tag{3.5.15}$$

$$\overline{C}_k^x = \frac{1}{M-1} \sum_{i=k-M+1}^{k} d_i^x (d_i^x)^T \tag{3.5.16}$$

$$\lambda_k^x = \max\left\{1, \frac{\text{trace}(\overline{C}_k^x)}{\text{trace}(C_k^x)}\right\} \tag{3.5.17}$$

The bias filter is:

$$\hat{b}_k^- = \hat{b}_{k-1} \tag{3.5.18}$$

	X_i	Y_i	Z_i
Position Error	0.1m^2	0.1m^2	0.1m^2
Velocity Error	$0.1(\text{m/s})^2$	$0.1(\text{m/s})^2$	$0.1(\text{m/s})^2$

Table 3.1: Initial Observation Dispersion Matrix

$$P_b^-(k) = \lambda_k^b \left(P_b(k-1) + Q_b(k)\right) \tag{3.5.19}$$

$$K_b(k) = P_b^-(k) S_k' \left[S_k P_b^-(k) S_k' + H_k P_k^{x-} H_k' + R_k\right]^{-1} \tag{3.5.20}$$

$$P_b(k) = \left[I - K_b(k) S_k\right] P_b^-(k) \tag{3.5.21}$$

$$d_k^b = z_k - H_k(k)\tilde{x}_k^-(k) - S_k \hat{b}_k^- = d_k^x - S_k \hat{b}_k^- \tag{3.5.22}$$

$$\hat{b}_k = \hat{b}_k^- + K_b(k) d_k^b \tag{3.5.23}$$

$$C_k^b = H_k P_k^{x^-} H_k^T + R_k + S_k P_b^-(k) S_k^T \tag{3.5.24}$$

$$\overline{C}_k^b = \frac{1}{M-1} \sum_{i=k-M+1}^{k} d_i^b (d_i^b)^T \tag{3.5.25}$$

$$\lambda_k^b = \max\left\{1, \frac{\text{trace}(\overline{C}_k^b)}{\text{trace}(C_k^b)}\right\} \tag{3.5.26}$$

where S_k is defined by the recursive sequence

$$U_k = A_k V_{k-1} + B_k \tag{3.5.27}$$

$$S_k = H_k U_k + C_k \tag{3.5.28}$$

$$V_k = U_k - \tilde{K}_x(k) S_k \tag{3.5.29}$$

And finally, the navigation errors are given by

$$\hat{X}_k = \hat{x}_k + V_k \hat{b}_k \tag{3.5.30}$$

To select the most effective adaptive methods, which not only can successfully fix the GPS data gaps, but also estimate the long wavelength IMU errors, all the above algorithms are tested in the southwestern Montana data sets (see Chapter 6 for more details) under the same initial conditions, which are described by Tables 3.1 to 3.4:

In particular, the integration results of the data collected along SR43 on June 15 2005 are shown here. For instance, the estimated navigation errors and the IMU

	X_i	Y_i	Z_i
Position Error (m)	0	0	0
Velocity Error (m/s)	0	0	0
Orientation Error (rad)	0	0	0
Accelerometer Bias (m/s^2)	0	0	0
Gyro Bias (rad)	0	0	0
Accelerometer Scale Error	0	0	0
Gyro Scale Error	0	0	0

Table 3.2: Initial State Vector

	X_i	Y_i	Z_i
Position Error	$25m^2$	$25m^2$	$25m^2$
Velocity Error	$25(m/s)^2$	$25(m/s)^2$	$25(m/s)^2$
Orientation Error	3.0^{-10}	3.0^{-10}	3.0^{-10}
Accelerometer Bias	$1.0^{-4}(m/s^2)^2$	$1.0^{-4}(m/s^2)^2$	$1.0^{-4}(m/s^2)^2$
Gyro Bias	$1.0^{-8}(rad)^2$	$1.0^{-8}(rad)^2$	$1.0^{-8}(rad)^2$
Accelerometer Scale Error	1.0^{-10}	1.0^{-10}	1.0^{-10}
Gyro Scale Error	1.0^{-12}	1.0^{-12}	1.0^{-12}

Table 3.3: Initial State Dispersion Matrix

	X_i	Y_i	Z_i
Position Error	$0.01m^2$	$0.01m^2$	$0.01m^2$
Velocity Error	$0.01(m/s)^2$	$0.01(m/s)^2$	$0.01(m/s)^2$
Orientation Error	1.0^{-8}	1.0^{-8}	1.0^{-8}
Accelerometer Bias	$1.0^{-7}(m/s^2)^2$	$1.0^{-7}(m/s^2)^2$	$1.0^{-10}(m/s^2)^2$
Gyro Bias	$1.0^{-16}(rad)^2$	$1.0^{-16}(rad)^2$	$1.0^{-16}(rad)^2$
Accelerometer Scale Error	1.0^{-16}	1.0^{-16}	1.0^{-16}
Gyro Scale Error	1.0^{-16}	1.0^{-16}	1.0^{-16}

Table 3.4: Initial Processing noise Dispersion Matrix

system errors by using the Maximum Likelihood estimator (section 3.4.1) are shown in Figures 3.1 to 3.7:

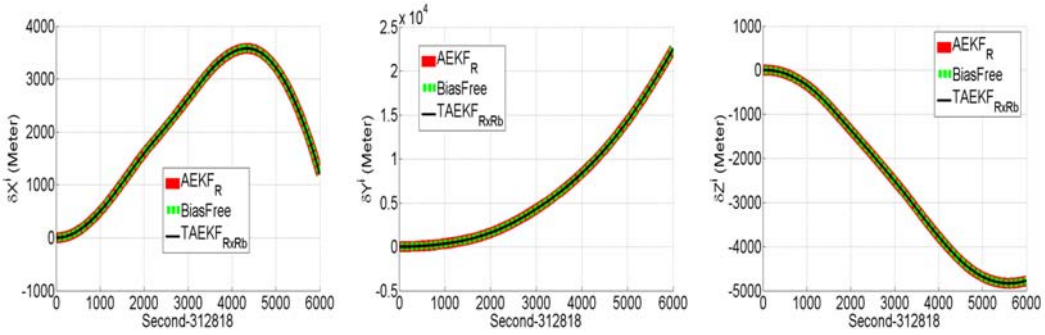

Figure 3.1: Estimated Position Errors by the Maximum Likelihood estimator

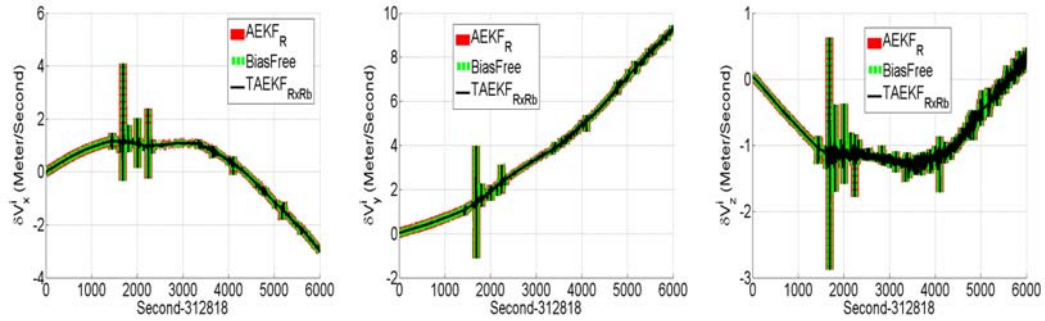

Figure 3.2: Estimated Velocity Errors by the Maximum Likelihood estimator

In Figures 3.1 to 3.7, the thick solid(red) lines are the adaptive Kalman filter estimates, where the navigation errors and the IMU errors are included in one state vector. The others are the TAEKF estimates, where the navigation errors and the IMU errors are decomposed into two stages. The subscripts in the legends denote the adaptive methods. For example, $TAEKF_{R\times Rb}$ stands for adapting the observation matrix R in the two-stage filter, and $TAEKF_{Q_x}$ stands for only adapting the processing noise of the navigation errors in equation (3.3.31), while leaving the processing

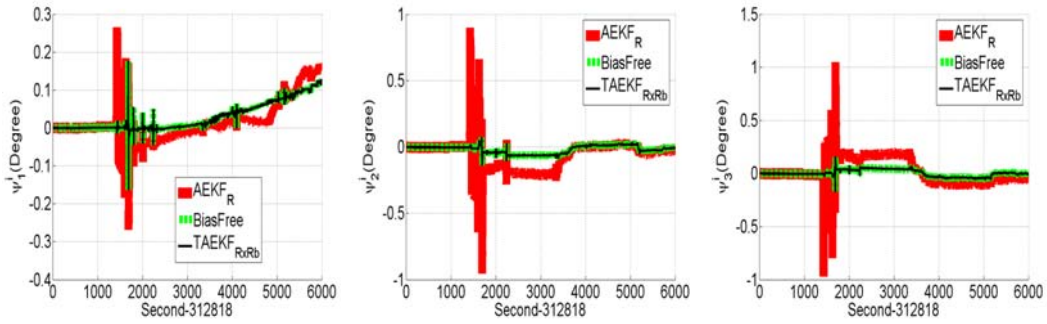

Figure 3.3: Estimated Orientation Errors by the Maximum Likelihood estimator

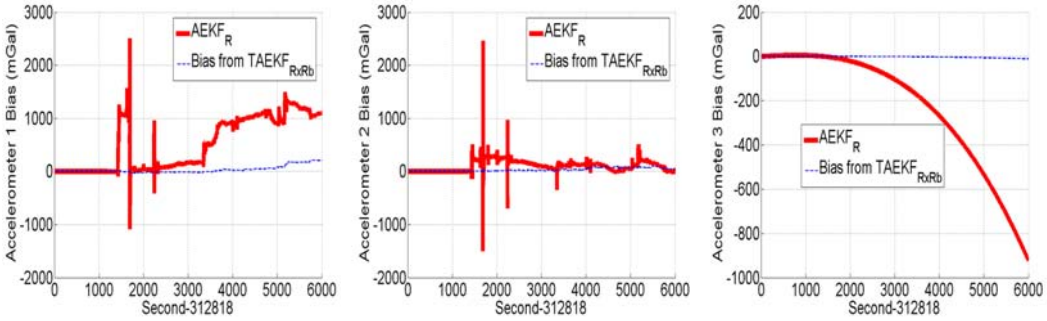

Figure 3.4: Estimated Accelerometer Biases by the Maximum Likelihood estimator

noises (in equation 3.3.36) of the IMU error models untouched. The two-stage setup allows us to have more flexibility in adapting the filter to yield the best results.

Analogously, the estimated results by rescaling the processing noise (section 3.4.2) are shown in Figures 3.8 to 3.14, in which the thick solid(red) lines are from equation (3.3.19) with equation (3.3.17) substituted into equation (3.4.8). By replacing $Q_X(k)$ with $S_k Q_X(k)$ in equation (3.3.31), the dashed(green) lines show the quantity in equation (3.3.34), while the thin solid lines in Figures 3.8 to 3.10 show the quantity in equation (3.3.43). The dashed lines in Figures 3.11 to 3.14 show the quantity in equation (3.3.39), after changing $Q_b(k)$ into $S_k Q_b(k)$ in equation (3.3.36).

The rescaling covariance matrix (see section 3.4.3) estimation results are shown in Figures 3.15 to 3.21, where the thick solid(red) lines are from equation (3.5.7). The

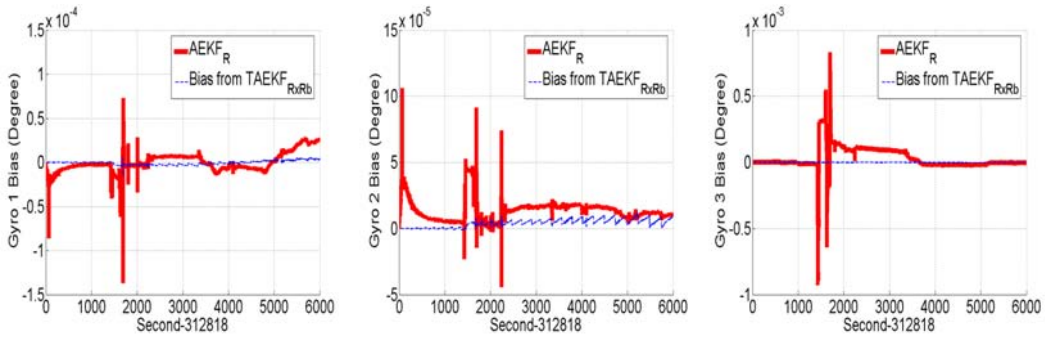

Figure 3.5: Estimated Gyro Biases by the Maximum Likelihood estimator

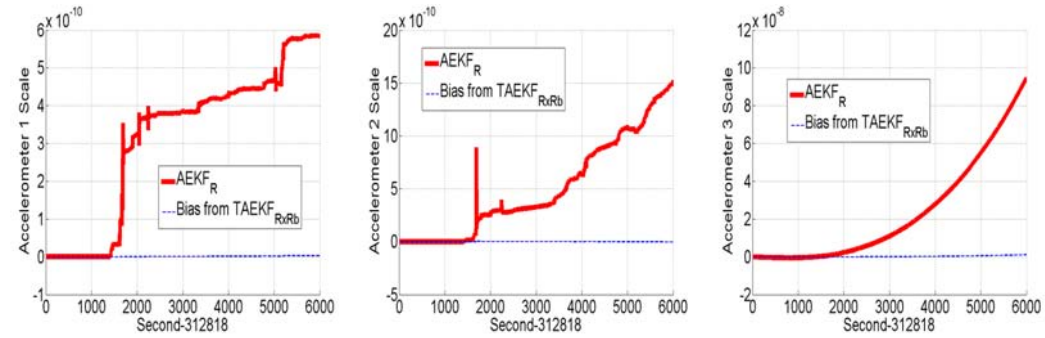

Figure 3.6: Estimated Accelerometer Scale by the Maximum Likelihood estimator

dashed(green) lines are the bias free estimator from equation (3.5.14). The thin(blue) lines in Figures 3.15 to 3.17 are from equation (3.5.30), while in Figures 3.18 to 3.21 they are the bias estimator from equation (3.5.23).

In all the Figures 3.1 to 3.21, the first 1500 seconds are the stationary data. The vehicle began traveling with an average speed of 22 meters per second after that. Due to the change of dynamics, we can see that there are relatively large oscillations in the state estimations from epoch 1500 to 2000, during which the filters adapt themselves to the new observation condition. In the figures which show the estimated IMU errors, we can see that in general the TAEKF provides relatively smoother estimation than the AEKF does. Recalling that our purpose of the INS/GPS integration is not only to fix the data gaps in the GPS solutions, but also to try to obtain the long wavelength

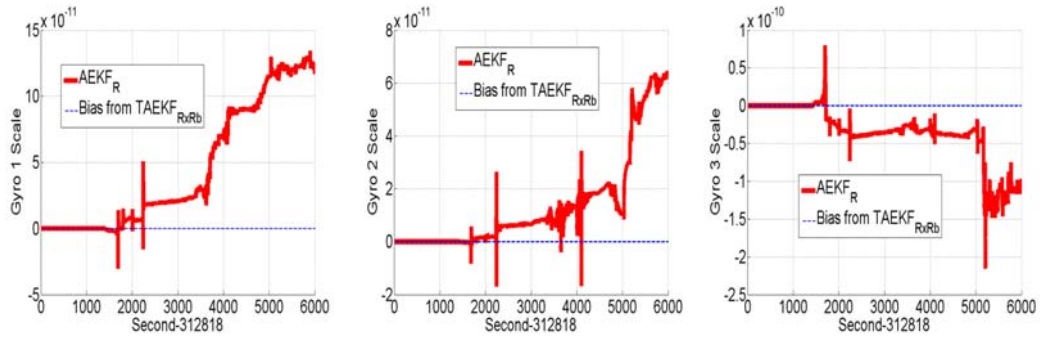

Figure 3.7: Estimated Gyro Scale by the Maximum Likelihood estimator

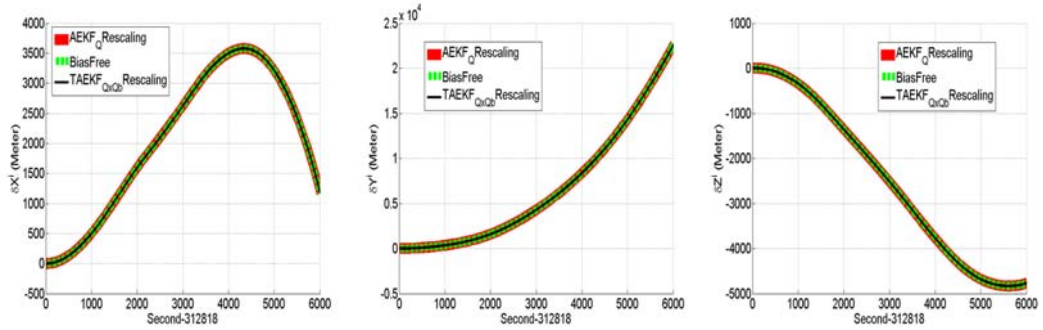

Figure 3.8: Estimated Position Error by rescaling the processing noise

IMU errors, which can be used in estimating the gravity disturbances, we choose the TAEKF in the following analysis. As for the different adaptive schemes, they do not show too much difference in the results, but the processing noise rescaling method described in section 3.4.2 is relatively easier to be implemented. As a result, the two-stage filter with processing noise rescaling method is used in the data analysis in chapter 6.

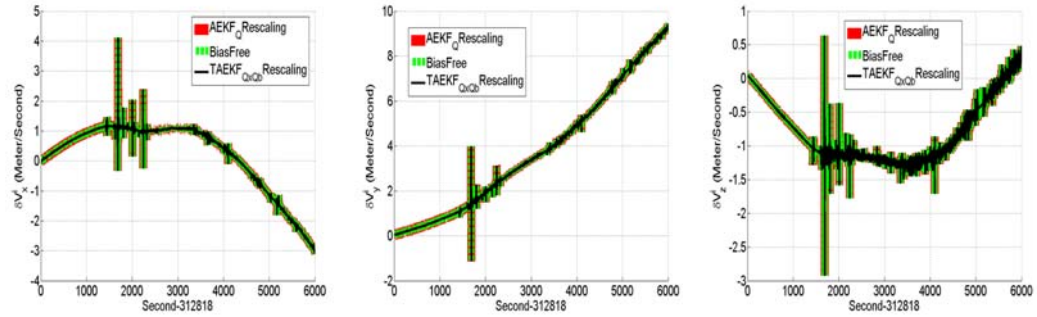

Figure 3.9: Estimated Velocity Error by rescaling the processing noise

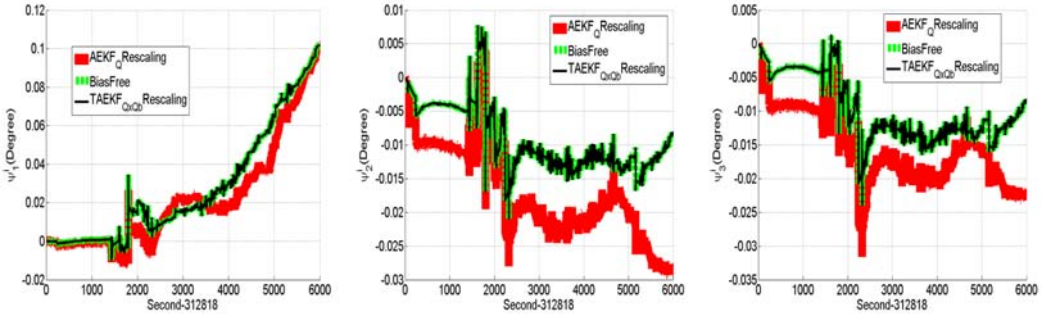

Figure 3.10: Estimated Orientation Error by rescaling the processing noise

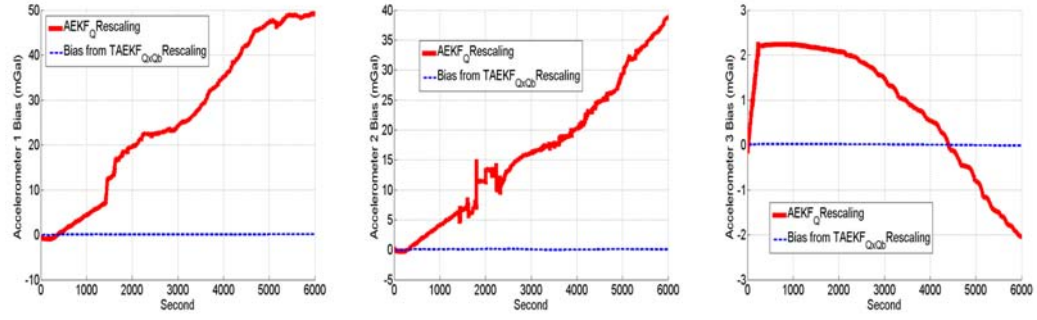

Figure 3.11: Estimated Accelerometer Biases by rescaling the processing noise

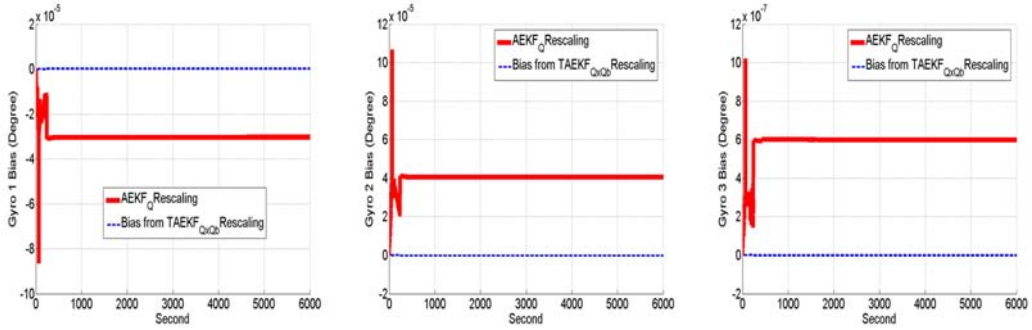

Figure 3.12: Estimated Gyro Biases by rescaling the processing noise

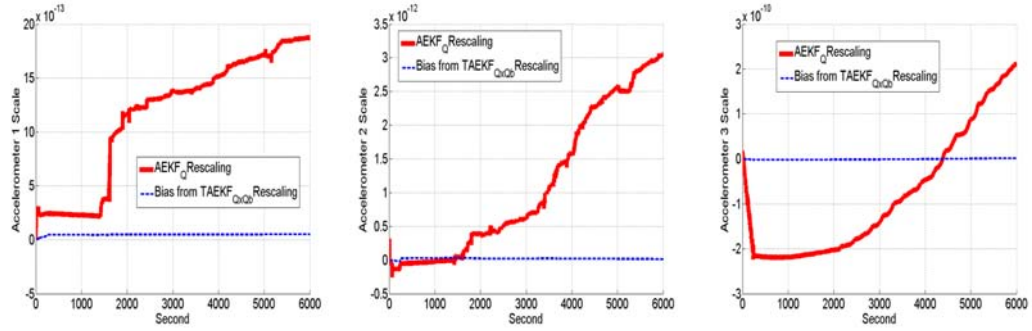

Figure 3.13: Estimated Accelerometer Scale by rescaling the processing noise

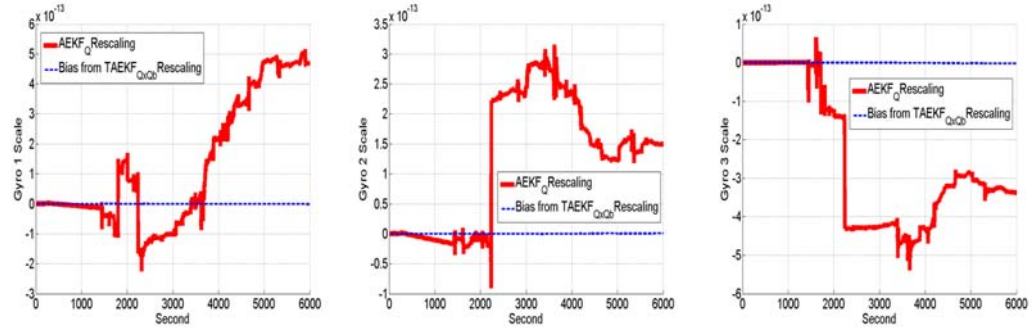

Figure 3.14: Estimated Gyro Scale by rescaling the processing noise

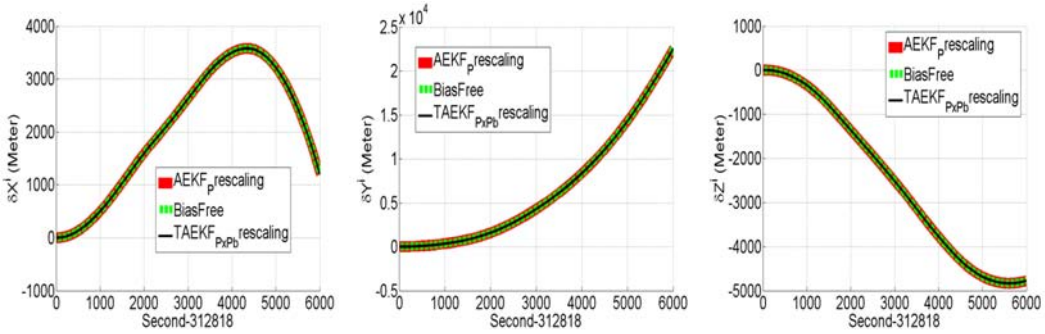

Figure 3.15: Estimated Position Errors by rescaling the covariance matrix

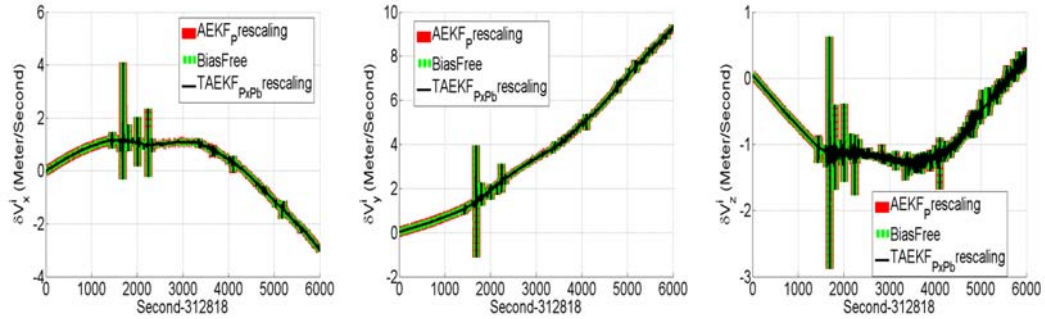

Figure 3.16: Estimated Velocity Errors by rescaling the covariance matrix

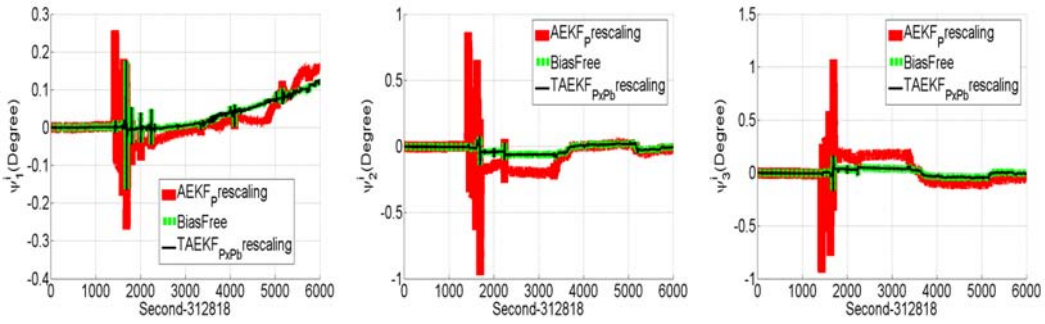

Figure 3.17: Estimated Orientation Errors by rescaling the covariance matrix

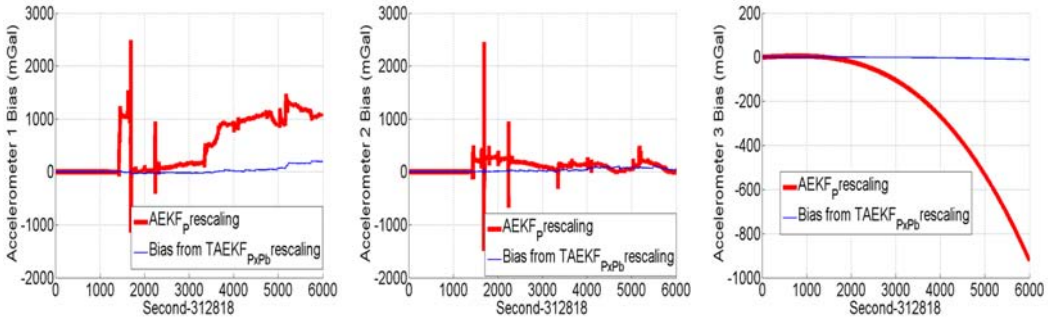

Figure 3.18: Estimated Accelerometer Biases by rescaling the covariance matrix

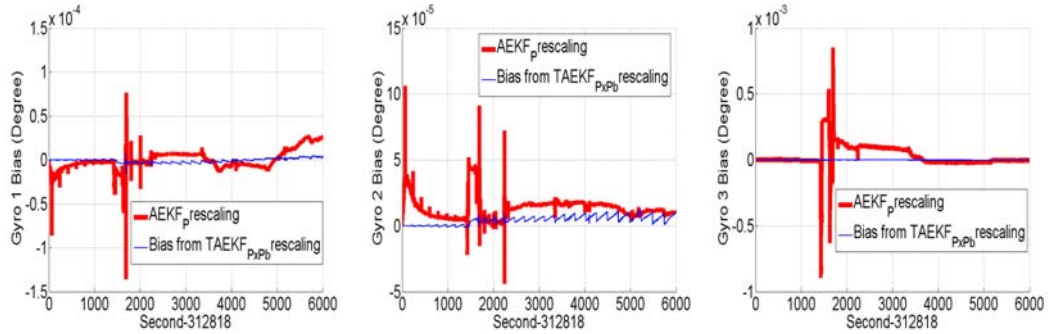

Figure 3.19: Estimated Gyro Biases by rescaling the covariance matrix

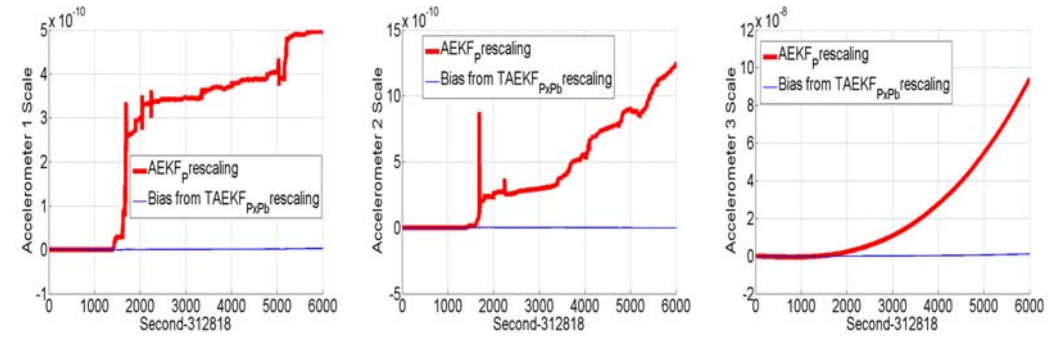

Figure 3.20: Estimated Accelerometer Scale by rescaling the covariance matrix

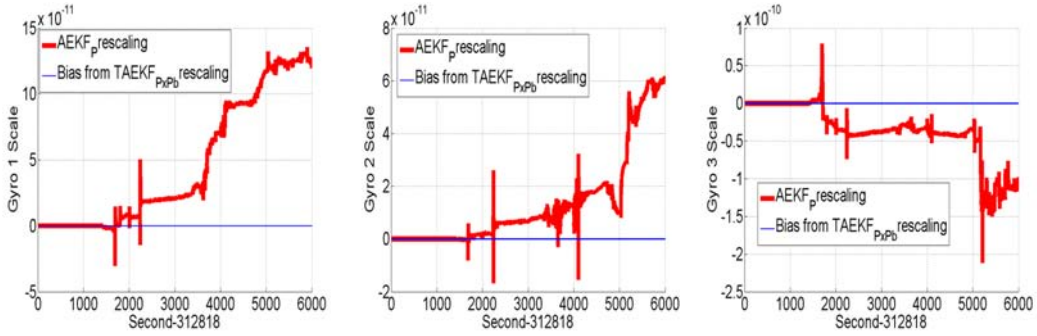

Figure 3.21: Estimated Gyro Scale by rescaling the covariance matrix

CHAPTER 4

INS ACCELERATION CALIBRATION AND GPS DATA PROCESSING

In the SINS/GPS gravimetric system, the gravity signal is the difference between the GPS determined kinematic acceleration and the IMU measured dynamic acceleration. As a result, the accuracy of the accelerations directly determines the accuracy of the gravity estimates. This chapter describes methods to improve the accuracy of these accelerations. First, in Section 4.1, the INS dynamic acceleration is calibrated based on the TAEKF estimated long wavelength errors. The rest of this chapter then focuses on improving the GPS measured kinematic acceleration and on related issues in the data processing aspects. Both the position method and the phase method are employed to determine the GPS acceleration. The final kinematic acceleration is obtained by correlating the position derived acceleration and the phase derived acceleration in the frequency domain.

4.1 Dynamic acceleration

From Chapter 2, we know that in the SINS, the specific force applied to the system is measured by the accelerometers in the b-frame. The following equation transforms this raw acceleration into the i-frame.

$$\tilde{\vec{a}}^i = \tilde{C}_b^i \tilde{\vec{a}}^b \tag{4.1.1}$$

where $\tilde{C}_b^i$ is computed by the quaternions, see Chapter 2.
$\tilde{\vec{a}}^b$ is the b-frame acceleration measured by the accelerometers.

From Chapter 3, we know the observation errors of the inertial sensors have two components. One consists of the low frequency bias and scale errors. The other is the dominant high frequency noise. Through the TAEKF described in Chapter 3, the bias and scale errors can be estimated at least partially. Then these errors can be

removed by the following equations from the dynamic acceleration:

$$\hat{\vec{a}}^i = \hat{C}_b^i \hat{\vec{a}}^b \tag{4.1.2}$$

where

$$\hat{C}_b^i = \left(I - [\hat{\Psi}^i \times]\right)^{-1} \tilde{C}_b^i \tag{4.1.3}$$

$$\hat{\vec{a}}^b = \tilde{\vec{a}}^b - \hat{b}_a - \mathrm{diag}\{\tilde{\vec{a}}^b\}\hat{k}_a \tag{4.1.4}$$

$\hat{\Psi}^i$, $\hat{b}_a$, and $\hat{k}_a$ are the TAEKF estimated orientation error, accelerometer bias and accelerometer scale error.

4.2 Kinematic acceleration

On the other hand, determining the kinematic acceleration is not as straightforward as determining the INS dynamic acceleration. It involves much more complicated computations. In general, there are two methods that may be used to obtain the kinematic acceleration. One is the position method where the acceleration is computed by taking two consecutive derivatives of the GPS-determined position with respect to time. The other method may be referred as the phase method (Kleusberg et al., 1990; Jekeli 1994; Jekeli and Garcia, 1997; Kennedy 2002; Serrano et al., 2004), where the accelerations are obtained by directly taking derivatives of the GPS carrier phase observables. The first method is relatively straightforward and easy to implement once the precise positioning solution is available. But it requires at least cm level precision in positioning in order to yield relatively accurate results (precision better than hundreds of mGal). To obtain this level of precision all the time for a terrestrial moving base system is very challenging in practice. However, the second method relaxes the stringent requirement of the position accuracy from mm-level or cm-level to meters (< 10m). But it requires continuous GPS phase observables because of the derivative computation. So any cycle slip in the phase data should be detected and fixed. After establishing the fundamental building blocks of the GPS data processing in Section 4.3 and Section 4.4, detecting and fixing cycle slips in kinematic scenarios are studied in section 4.5. Section 4.6 gives the typical differential GPS positioning algorithms. The phase method is introduced in Section 4.7, which is followed by some examples in Section 4.8.

4.3 Satellite position

Computing the satellite orbits is one of the fundamental steps of GPS data processing. The GPS satellite position can be obtained either by using the broadcast ephemeris or by interpolating the precise orbits provided by IGS or other GPS analysis centers in the post processing model. The observed GPS satellite orbit parameters are stored in the navigation file. The GPS satellite coordinates at given epoch can be computed based on these orbit parameters, for details see Appendix A.

In the post processing stage, the IGS precise orbit may be used to yield more accurate satellite coordinates. However, the IGS precise orbits only give GPS satellite position every 15 minutes, which usually does not match the sampling rate of the moving base system. The Lagrange interpolation method is probably the most convenient and efficient method and has several advantages (Cheney and Kincaid, 1994; Witchayangkoon, 2000) to interpolate these orbits into the desired epochs.

Having a set of fixed nodes, x_1, x_2, ..., x_n, the Lagrange interpolating polynomial, $P(x)$, of degree $n-1$, that passes through the n points $(x_1, y_1 = f(x_1))$, $(x_2, y_2 = f(x_2)$),..., $(x_n, y_n = f(x_n))$, and is given by

$$P(x) = \sum_{j=1}^{n} P_j(x) \tag{4.3.1}$$

where

$$P_j(x) = y_j \sum_{k=1, k\neq j}^{n} \frac{x - x_k}{x_j - x_k} \tag{4.3.2}$$

Written explicitly,

$$\begin{aligned} P(x) = \; & \tfrac{(x-x_2)(x-x_3)\cdots(x-x_n)}{(x_1-x_2)(x_1-x_3)\cdots(x_1-x_n)} y_1 \\ & + \tfrac{(x-x_1)(x-x_3)\cdots(x-x_n)}{(x_2-x_1)(x_2-x_3)\cdots(x_2-x_n)} y_2 \\ & + \cdots + \tfrac{(x-x_1)(x-x_2)\cdots(x-x_{n-1})}{(x_n-x_1)(x_n-x_2)\cdots(x_n-x_{n-1})} y_n \end{aligned} \tag{4.3.3}$$

The formula was first published by Waring in 1779, rediscovered by Euler in 1783, and published by Lagrange in 1795 (Jeffreys 1988). For interpolating the satellite coordinate, it is enough to use 11 nodes in equation (4.3.3) to yield mm-level accuracy. Both the precise and broadcast orbits are evaluated at the same time span, and the comparison results are shown in Appendix A.

4.4 GPS observables and their linear combinations

In GPS data processing, the following three kinds of observables are usually used, pseudo-range, phase, and Doppler.

The GPS pseudo-range observable:

$$P_{i,l}^k = \rho_i^k + T_i^k + I_{i,l}^k + c(\Delta t_i - \Delta t^k) + c(b^k + b_i) + m_{i,l}^k + \varepsilon_{i,l}^k \tag{4.4.1}$$

where ρ_i^k is the true geometric distance from satellite k to receiver i,
T_i^k and $I_{i,l}^k$ are the troposphere and ionosphere delay,
c is the speed of light in vacuum,
$\Delta t_i, \Delta t^k$ are the satellite and receiver clock errors,
b^k and b_i are the hardware delays,
$m_{i,l}^k$ is the multi-path effect,
$\varepsilon_{i,l}^k$ is the observation error,
l stands for the carrier phase. For example, $l = 1$ means pseudo-range carried by GPS L1 carrier.

The GPS phase observation equation:

$$\Phi_{i,l}^k = \rho_i^k + c(\Delta t_i - \Delta t^k) + T_i^k - I_i^k/f_l^2 + \lambda_l B_i^k + \lambda_l N_{i,l}^k + \lambda_l(\varphi_0^k - \varphi_{il,0}) + m_{i,l}^k + \varepsilon_{i,l}^k \tag{4.4.2}$$

where $\Phi_{i,l}^k$ is the phase observation value on frequency L1 or L2 as indicted by $l = 1$ or $l = 2$ respectively.
f_l is the GPS frequency.
λ_l is the corresponding wavelength,
I_i^k/f_l^2 is the ionosphere effect (first order only),
B_i^k constant bias expressed in cycles in practice it may contain the phase windup (Leick 2004; Wu. et. al., 1993) delays, which is due to the relative rotation between the GPS antenna and the river antenna.
φ_0^k is the initial phase of satellite k.
$\varphi_{il,0}$ is the initial phase of receiver i.
$m_{i,l}^k$ is the multi-path effect.
$\varepsilon_{i,l}^k$ contains other un-modeled errors and observation errors.

The Doppler data:

The equation for the observed Doppler shift, D, scaled to range rate is given by:

$$-D * \lambda = \dot{\rho} + c\Delta\dot{\delta} + e \tag{4.4.3}$$

where $\dot{\rho}$ is the first order derivative of the true geometric range from satellite to receiver with respect to time, and $\Delta\delta = \delta_R - \delta^s$. Assuming the satellite clock bias, δ^s, has been corrected, $\Delta\delta$ equals the receiver clock delay, δ_R. e is the observation error, which may include the atmosphere errors. The achievable observation accuracy of

the Doppler frequency is 0.001 Hz. This corresponds to 0.3m/s if the Doppler shift is measured in the C/A-code tracking loop (Hoffman-Wellenhof et al. 2001). A detailed derivation of Doppler equations within the frame of GPS is given in Remondi (1984).

To eliminate or reduce the systematic errors, various linear combinations such as the double difference and triple difference have been established.

The Double Difference (DD) model is commonly used to remove or reduce the error terms in the above one-way observables.

$$\Phi_{ij,1}^{kl} := (\Phi_{i,1}^{k} - \Phi_{j,1}^{k}) - (\Phi_{i,1}^{l} - \Phi_{j,1}^{l}) = \rho_{ij}^{*kl} - I_{ij}^{kl}/f_1^2 + \lambda_1 N_{ij,1}^{kl} + \varepsilon_{ij,1}^{kl} \tag{4.4.4}$$

$$\Phi_{ij,2}^{kl} := (\Phi_{i,2}^{k} - \Phi_{j,2}^{k}) - (\Phi_{i,2}^{l} - \Phi_{j,2}^{l}) = \rho_{ij}^{*kl} - I_{ij}^{kl}/f_2^2 + \lambda_2 N_{ij,2}^{kl} + \varepsilon_{ij,2}^{kl} \tag{4.4.5}$$

$$P_{ij,1}^{kl} := (P_{i,1}^{k} - P_{j,1}^{k}) - (P_{i,1}^{l} - P_{j,1}^{l}) = \rho_{ij}^{*kl} + I_{ij}^{kl}/f_1^2 + e_{ij,1}^{kl} \tag{4.4.6}$$

$$P_{ij,2}^{kl} := (P_{i,2}^{k} - P_{j,2}^{k}) - (P_{i,2}^{l} - P_{j,2}^{l}) = \rho_{ij}^{*kl} + I_{ij}^{kl}/f_2^2 + e_{ij,2}^{kl} \tag{4.4.7}$$

where

$$\rho_{ij}^{*kl} = \rho_{ij}^{kl} + T_{ij}^{kl} \tag{4.4.8}$$

$\varepsilon_{ij,1(2)}^{kl}$ contains the DD multi-path effect, differential code bias, and phase windup effect as well as observation errors. $e_{ij,1(2)}^{kl}$ contains the DD multipath effect, and observation errors. However, when establishing the DD observables in practice, the following three requirements (Rizos 1999) need to be considered:

(1). All receivers should take observations to common-view satellites at epochs that are within 30 milliseconds (10^{-3} second) of each other, to ensure that satellite clock errors cancel in between receiver differences. This requirement is modest. In general, it is not difficult to achieve 30 milliseconds synchronizations for the satellite transmission epochs.

(2). Receivers should be synchronized with each other at the microsecond (10^{-6} second) level to ensure that all the observation time-tags are consistent with each other.

(3). All receivers should be "externally" synchronized to the Satellite Ephemeris Time Scale (in general, GPST) at the millisecond level.

The time-tag requirements (points (2) and (3)) can be met if the GPS navigation solution is used to individually synchronize the receiver to GPST. The receiver clock bias (which defines the offset of the internal clock from GPST) can be determined to better than 1 microsecond accuracy using the pseudo-range point position solution. If the clock is reset always to GPST, code-correlating receivers can be considered as being always (automatically) synchronized to each other via GPST. On the other hand, if the receiver clock is not continuously reset to GPST using the navigation

solution, then this needs to be done during post-mission analysis of the recorded data. As a result, in the post data processing stage, a point positioning solution at both ends of the base line is performed to check the receiver clock errors. If the clock error was not corrected based on the navigation solution, i.e., the receiver did not have the "clock steering" feature, then the receiver clock is adjusted based on the estimated clock error provided by the point positioning results to fulfill the point (3). As Gurtner (2001) pointed out, the corresponding range and phase observations at this epoch should be adjusted by the equations (4.4.9) to (4.4.11):

$$t_{\text{cor}} = t_{\text{rec}} - dT_{\text{rec}} \tag{4.4.9}$$

where t_{rec} is the receiver clock time, dT_{rec} is the estimated receiver clock error, and t_{cor} is the corrected receiver clock time.

$$\rho_{\text{cor}} = \rho_{\text{obs}} - c * dT_{\text{rec}} \tag{4.4.10}$$

where ρ_{obs} is the receiver observed pseudo-range, and ρ_{cor} is the adjusted pseudo-range.

$$\phi_{\text{cor}} = \phi_{\text{obs}} - dT_{\text{rec}} * f \tag{4.4.11}$$

where ϕ_{obs} is the observed phase data unit in cycles, and f is the frequency of the corresponding carrier.

The Triple Difference (TD) which is defined to be the differences of DD between two successive epochs is another commonly used linear combination. Suppose the data having a 1Hz sampling rate, the TD observables are given by equations (4.4.12) to (4.4.15).

$$\begin{aligned}
\delta\Phi^{kl}_{ij,1}(t) &:= \Phi^{kl}_{ij,1}(t) - \Phi^{kl}_{ij,1}(t-1) \\
&= \rho^{kl}_{ij}(t) - I^{kl}_{ij}(t)/f_1^2 + T^{kl}_{ij}(t) + \lambda_1 N^{kl}_{ij,1}(t) + \varepsilon^{kl}_{ij,1}(t) - \rho^{kl}_{ij}(t-1) + \\
&\quad I^{kl}_{ij}(t-1)/f_1^2 - T^{kl}_{ij}(t-1) - \lambda_1 N^{kl}_{ij,1}(t-1) - \varepsilon^{kl}_{ij,1}(t-1) \\
&= \left[\rho^{kl}_{ij}(t) - \rho^{kl}_{ij}(t-1)\right] - \left[I^{kl}_{ij}(t) - I^{kl}_{ij}(t-1)\right]/f_1^2 + \\
&\quad \left[T^{kl}_{ij}(t) - T^{kl}_{ij}(t-1)\right] + \lambda_1 \left[N^{kl}_{ij,1}(t) - N^{kl}_{ij,1}(t-1)\right] + \delta\varepsilon^{kl}_{ij,1}(t)
\end{aligned} \tag{4.4.12}$$

$$\begin{aligned}
\delta\Phi^{kl}_{ij,2}(t) &:= \Phi^{kl}_{ij,2} - \Phi^{kl}_{ij,2}(t-1) \\
&= \rho^{kl}_{ij}(t) - I^{kl}_{ij}(t)/f_2^2 + T^{kl}_{ij}(t) + \lambda_2 N^{kl}_{ij,2}(t) + \varepsilon^{kl}_{ij,2}(t) - \rho^{kl}_{ij}(t-1) + \\
&\quad I^{kl}_{ij}(t-1)/f_2^2 - T^{kl}_{ij}(t-1) - \lambda_2 N^{kl}_{ij,2}(t-1) + \varepsilon^{kl}_{ij,2}(t-1) \\
&= \left[\rho^{kl}_{ij}(t) - \rho^{kl}_{ij}(t-1)\right] - \left[I^{kl}_{ij}(t) - I^{kl}_{ij}(t-1)\right]/f_2^2 + \\
&\quad \left[T^{kl}_{ij}(t) - T^{kl}_{ij}(t-1)\right] + \lambda_2 \left[N^{kl}_{ij,2}(t) - N^{kl}_{ij,2}(t-1)\right] + \delta\varepsilon^{kl}_{ij,2}(t)
\end{aligned}$$

(4.4.13)

$$\begin{aligned}\delta P^{kl}_{ij,1}(t) &= \left[\rho^{kl}_{ij}(t) - \rho^{kl}_{ij}(t-1)\right] \\ &\quad + \left[I^{kl}_{ij}(t) - I^{kl}_{ij}(t-1)\right]/f_1^2 + \left[T^{kl}_{ij}(t) - T^{kl}_{ij}(t-1)\right] + \delta e^{kl}_{ij,1}(t)\end{aligned} \tag{4.4.14}$$

$$\begin{aligned}\delta P^{kl}_{ij,2}(t) &= \left[\rho^{kl}_{ij}(t) - \rho^{kl}_{ij}(t-1)\right] \\ &\quad + \left[I^{kl}_{ij}(t) - I^{kl}_{ij}(t-1)\right]/f_2^2 + \left[T^{kl}_{ij}(t) - T^{kl}_{ij}(t-1)\right] + \delta e^{kl}_{ij,2}(t)\end{aligned} \tag{4.4.15}$$

In this combination, the ionosphere and toposphere effects are further reduced. If the phase observables do not have the cycle slips, then the TD phase observable does not include the integer ambiguity, which means that we need not worry about this issue in the TD model. However, due to the differencing procedures, TD observables have a much higher noise level than the DD observables. As a result, it is not recommended if the highest accuracy is expected (Rizos 1999). It is usually used to get the first positioning solution in the post data processing.

4.5 Cycle slip detection and validation

In GPS data processing, especially in the phase acceleration method, which requires taking derivatives of the phase observables, cycle slips must be properly handled. Over the past decades, many cycle-slip-sensitive linear combinations, such as ionosphere-only (Goad 1986; Bastos and Landau 1988; and Seeber 2003), wide-lane-phase-minus-narrow-lane-pseudo-range (Blewitt,1990; Gao and Li 1999; Bisnath 2000), and Triple Difference (Kim and Langley 2001) combinations have been investigated. In this section, first these methods are tested in the kinematic case. Then a new filtering model is proposed to reduce the noise level of the code measurements for fixing the cycle slips in the phase observables.

4.5.1 Ionosphere-only linear combination

By taking differences between (4.4.4) and (4.4.5), the geometric range and tropo-effect are cancelled. This leads to the ionosphere-only linear combination as shown in equation (4.5.1).

$$\begin{aligned}\Phi^{kl}_{ij,1} - \Phi^{kl}_{ij,2} &= -\tfrac{I^{kl}_{ij}}{f_1^2} + \tfrac{I^{kl}_{ij}}{f_2^2} + \lambda_1 N^{kl}_{ij,1} - \lambda_2 N^{kl}_{ij,2} + \varepsilon^{kl}_{ij,12} \\ &= \tfrac{f_1^2 - f_2^2}{f_1^2 f_2^2} I^{kl}_{ij} + \lambda_1 N^{kl}_{ij,1} - \lambda_2 N^{kl}_{ij,2} + \varepsilon^{kl}_{ij,12}\end{aligned} \tag{4.5.1}$$

Many researchers noticed that under benign observation condition, this linear combination and its time differences are very sensitive to a cycle slip. The time differences of the ionosphere-only combination leave a very small component of the ionospheric, multi-path and noise terms, and an estimate of the cycle slip, if any (Bisnath 2000). However, by only using the ionosphere-only linear combination, it is not possible to determine the size of the cycle slip on L1 and L2. It can only tell us there is a cycle slip in the phase observables. So other linear combinations are needed to determine its size.

4.5.2 Range Residuals

Bastos and Landau (1988) proposed the so-called range residuals as in equation (4.5.2) to detect and fix the cycle slip.

$$\Delta\rho_{Li}(t) = \lambda_i(\varphi_i(t) + \Delta N_i - \varphi_i(t_1)) - (\rho(t) - \rho(t_1)) \quad i = 1, 2 \tag{4.5.2}$$

This quantity is not affected by the motion of the receiver, clock, tropospheric, or relativistic errors, because they are the same for both pseudoranges and phase ranges and therefore disappear when the two are differenced. However, the range residuals have a noise level that can reach tens of cycles due to measurement, ionospheric, and multipath errors. Linear regression or a Kalman filter is required to reduce the noise level before and after cycle slip estimation.

4.5.3 Wide lane phase minus narrow lane pseudo-range

Blewitt (1990), Gao and Li (1999), and Bisnath (2000) proposed the so-called wide-lane-minus-narrow-lane linear combination as shown in the equation (4.5.3):

$$\begin{aligned} & \lambda_4(\nabla\Delta\varphi_1 - \nabla\Delta\varphi_2) - \lambda_5(\tfrac{\nabla\Delta P_1}{\lambda_1} + \tfrac{\nabla\Delta P_2}{\lambda_2}) \\ = \; & \lambda_4(\nabla\Delta N_1 - \nabla\Delta N_2) \\ & \quad + \lambda_4(\tfrac{\nabla\Delta m_1}{\lambda_1} - \tfrac{\nabla\Delta m_2}{\lambda_2}) - \lambda_5(\tfrac{\nabla\Delta M_1}{\lambda_1} + \tfrac{\nabla\Delta M_2}{\lambda_2}) \\ & \quad + \lambda_4(\tfrac{\nabla\Delta\varepsilon_1}{\lambda_1} - \tfrac{\nabla\Delta\varepsilon_2}{\lambda_2}) - \lambda_5(\tfrac{\nabla\Delta e_1}{\lambda_1} + \tfrac{\nabla\Delta e_2}{\lambda_2}) \end{aligned} \tag{4.5.3}$$

where

$$\lambda_4 = (\lambda_1^{-1} - \lambda_2^{-1})^{-1} \tag{4.5.4}$$

$$\lambda_5 = (\lambda_1^{-1} + \lambda_2^{-1})^{-1} \tag{4.5.5}$$

$\nabla\Delta\varphi_1$, and $\nabla\Delta\varphi_2$ are the corresponding quantities on the left side of equation (4.4.4) and equation (4.4.5), respectively. But the units are in cycles. $\nabla\Delta P_1$, and $\nabla\Delta P_2$ are coming from equations (4.4.6) and (4.4.7). Instead of using the superscripts and

subscripts ($\bullet_{ij}^{kl}$), $\nabla\Delta$ is used to denote the double difference operation. On the right side of equation (4.5.3), the double difference ambiguities, $\nabla\Delta N_1$ and $\nabla\Delta N_2$, are constants. The linear combinations of the error terms should show a white noise characteristic. Without cycle slips, there should not be big jumps in this linear combination. As a result, any abrupt change may indicate a cycle slip. However, the observation noises in the pseudo-ranges disallow directly using this linear combination to determine the small cycle slips (< 10 cycles). Again, before and after a cycle slip, curve fitting or Kalman filtering techniques are required to reduce the pseudo-range noises.

4.5.4 TD observables minus the Doppler predicted range changes

It was noted above that the success of these methods depends on filtering and fitting techniques. However, many cycle slips in a kinematic scenario usually occur consecutively in time, making it rather challenging to find appropriate filtering and smoothing methods. Recognizing this problem, Kim and Langley (2001) used the TD observables, and the Doppler observables to detect and fix cycle slips. The TD phase observables are given by:

$$\delta\nabla\Delta\Phi_1 = \delta\nabla\Delta\rho + \lambda_1 C_1 + \delta\nabla\Delta\tau + \delta\nabla\Delta s - \delta\nabla\Delta I + \delta\nabla\Delta b_1 + \delta\nabla\Delta\varepsilon_1 \quad (4.5.6)$$

$$\delta\nabla\Delta\Phi_2 = \delta\nabla\Delta\rho + \lambda_2 C_2 + \delta\nabla\Delta\tau + \delta\nabla\Delta s - \gamma\cdot\delta\nabla\Delta I + \delta\nabla\Delta b_2 + \delta\nabla\Delta\varepsilon_2 \quad (4.5.7)$$

where C_1 and C_2 are the potential cycle slips in L1 and L2 carrier phases, respectively; τ is the delay due to the troposphere; s is the satellite orbit bias; I is the delay of the L1 carrier phase due to the ionosphere; $\gamma = (\lambda_2/\lambda_1)^2 \approx 1.65$; b is the multi-path; and ε is the receiver system noise.

As pointed out by Kim and Langley (2001), the geometric range should be removed to estimate the size of the cycle slips. After removing it from equation (4.5.6) and (4.5.7), the TD carrier-phase prediction residuals are given by:

$$\delta\nabla\Delta\Phi_{TD1} = \delta\nabla\Delta\Phi_1 - \delta\nabla\Delta\hat{\rho} = \lambda_1\nabla\Delta C_1 + \triangle\varepsilon_1' \quad (4.5.8)$$

$$\delta\nabla\Delta\Phi_{TD2} = \delta\nabla\Delta\Phi_2 - \delta\nabla\Delta\hat{\rho} = \lambda_2\nabla\Delta C_2 + \triangle\varepsilon_2' \quad (4.5.9)$$

where $\delta\nabla\Delta\hat{\rho}_k = -(\nabla\Delta D_k + \nabla\Delta D_{k-1})/2$ if the Doppler frequencies are available, otherwise $\delta\nabla\Delta\hat{\rho}_k = (\nabla\Delta P_k - \nabla\Delta P_{k-1})/(t_k - t_{k-1})$.

The above two equations and their statistics provide some confidence intervals for the candidates of the cycle slips. To validate the amount of the cycle slips, Kim and Langley (2001) used a search method, which is conceptually the same as resolving the

ambiguities in DD observations. This method is very complicated to implement in a kinematic scenario. A more efficient method based on the Doppler data is explored in the following section.

4.5.5 Kalman filtering the pseudo-range by use of Doppler data

Suppose the acceleration of the DD geometric distances can be characterized as white noise, the dynamics of the DD geometric distance is written by:

$$\frac{d}{dt}\begin{bmatrix} \nabla\Delta P \\ \nabla\Delta\dot{P} \end{bmatrix} = \begin{bmatrix} 0 & 1 \\ 0 & 0 \end{bmatrix}\begin{bmatrix} \nabla\Delta P \\ \nabla\Delta\dot{P} \end{bmatrix} + \begin{bmatrix} 0 \\ e \end{bmatrix}, \quad e \sim N(0, \sigma_e^2) \tag{4.5.10}$$

A first order approximate solution of the above equation is given by:

$$\begin{bmatrix} \nabla\Delta P \\ \nabla\Delta\dot{P} \end{bmatrix}_k = \begin{bmatrix} 1 & \Delta t \\ 0 & 1 \end{bmatrix}\begin{bmatrix} \nabla\Delta P \\ \nabla\Delta\dot{P} \end{bmatrix}_{k-1} + \begin{bmatrix} \varepsilon_1 \\ \varepsilon_2 \end{bmatrix}, \quad \varepsilon_{1/2} \sim N(0, \sigma_{\varepsilon_{1/2}}^2) \tag{4.5.11}$$

Considering that the DD model of equation (4.4.3) does not contain the clock errors any more, the observation equation is given by:

$$z := \begin{bmatrix} \nabla\Delta P \\ \nabla\Delta\dot{P} \end{bmatrix}_k = \begin{bmatrix} \nabla\Delta P \\ -\nabla\Delta Doppler \end{bmatrix}_k + \begin{bmatrix} v_1 \\ v_2 \end{bmatrix}, \quad v_{1/2} \sim N(0, \sigma_{v_{1/2}}^2) \tag{4.5.12}$$

The above equations can be framed into a Kalman filter system by use of the following conventional notations.

The state transition equation:

$$X_k = \Phi_{k,k-1}X_{k-1} + \varepsilon_k \tag{4.5.13}$$

where $X_k := \begin{bmatrix} \nabla\Delta P \\ \nabla\Delta\dot{P} \end{bmatrix}_k$, $\Phi_{k,k-1} = \begin{bmatrix} 1 & \Delta t \\ 0 & 1 \end{bmatrix}$, $\varepsilon_k \sim (0, Q_k)$.

The observation equation:

$$z_k := H_k X_k + v_k \tag{4.5.14}$$

where $H_k = \begin{bmatrix} 0 & 1 \\ 0 & 0 \end{bmatrix}$, $v_k \sim (0, R_k)$

The solution of X_k is given by the well known Kalman algorithm as in the following steps:

Prediction:

$$\hat{X}_k^- = \Phi_{k,k-1}\hat{X}_{k-1} \tag{4.5.15}$$

$$\hat{P}_k^- = \Phi_{k,k-1}\hat{P}_{k-1}\Phi_{k,k-1}^T + Q_{k-1} \tag{4.5.16}$$

where X_k denotes the KF estimated state vector;
X_k^- is the predicted state vector for the next epoch;
$\hat{P}_k$ is the estimated state covariance matrix;
$\hat{P}_k^-$ is the predicted state covariance matrix

Update:

$$K_k = \hat{P}_k^- H_k^T (H_k \hat{P}_k^- H_k^T + R_k)^{-1} \tag{4.5.17}$$

$$\hat{X}_k = \hat{X}_k^- + K_k(z_k - H_k\hat{X}_k^-) \tag{4.5.18}$$

$$\hat{P}_k = (I - K_k H_k)\hat{P}_k^- \tag{4.5.19}$$

where K_k is the Kalman gain, which defines the updating weight between measurements and predictions from the system dynamics model.

Suppose the observation errors in the pseudo-ranges are significantly reduced by the Kalman filter. Then the ionosphere-only and the wide-lane-phase-minus-narrow-lane-pseudo-range linear combinations are used to detect the cycle slips in the phase observables. The time differences of the ionosphere-only combination is defined by equation (4.5.20):

$$\begin{aligned} \Delta\xi_n &:= (\Phi_{ij,1}^{kl} - \Phi_{ij,2}^{kl})_n - (\Phi_{ij,1}^{kl} - \Phi_{ij,2}^{kl})_{n-1} \\ &\approx \lambda_1(N_{ij,1}^{kl} + C_1) - \lambda_2(N_{ij,2}^{kl} + C_2) - [\lambda_1 N_{ij,1}^{kl} - \lambda_2 N_{ij,2}^{kl}] \\ &= \lambda_1 C_1 - \lambda_2 C_2 \end{aligned} \tag{4.5.20}$$

If $\Delta\xi_n > \tau$, say 2.5cm, then a cycle slip is identified at epoch n. Time differences of the wide-lane phase minus narrow-lane pseudo-range linear combination are used to validate the amount of the slip at this epoch.

$$\begin{aligned} \Delta\eta_n &:= \left\{\lambda_4(\nabla\Delta\varphi_1 - \nabla\Delta\varphi_2) - \lambda_5(\tfrac{\nabla\Delta P_1}{\lambda_1} + \tfrac{\nabla\Delta P_2}{\lambda_2})\right\}_n \\ &\quad - \left\{\lambda_4(\nabla\Delta\varphi_1 - \nabla\Delta\varphi_2) - \lambda_5(\tfrac{\nabla\Delta P_1}{\lambda_1} + \tfrac{\nabla\Delta P_2}{\lambda_2})\right\}_{n-1} \\ &\approx \lambda_4(C_1 - C_2) \end{aligned} \tag{4.5.21}$$

Finally, the cycle slips are determined by solving equations (4.5.20) and (4.5.21), which gives:

$$C_2 = \left(\frac{\Delta\xi_n}{\lambda_1} - \frac{\Delta\eta_n}{\lambda_4}\right)\frac{\lambda_1}{\lambda_1 - \lambda_2} \tag{4.5.22}$$

$$C_1 = \Delta\eta_n/\lambda_4 + C_2 \tag{4.5.23}$$

4.6 DGPS solutions

In the TD observables, the ionosphere and troposphere effects are reduced. Furthermore, the integer ambiguities are cancelled out in the cycle slip free phase observables. If j is the base station, whose coordinates are given, then

$$\begin{aligned}
\rho_{ij}^{kl}(t) &= \rho_i^k(t) - \rho_i^l(t) - \rho_j^k(t) + \rho_j^l(t) \\
&= \rho_i^k(t)_0 - \rho_i^l(t)_0 - \rho_j^k(t) + \rho_j^l(t) \\
&\quad + \left[\frac{x_i(t)_0 - x^k(t)}{\rho_i^k(t)_0} - \frac{x_i(t)_0 - x^l(t)}{\rho_i^l(t)_0}\right]\Delta X_i(t) \\
&\quad + \left[\frac{y_i(t)_0 - y^k(t)}{\rho_i^k(t)_0} - \frac{y_i(t)_0 - y^l(t)}{\rho_i^l(t)_0}\right]\Delta Y_i(t) \\
&\quad + \left[\frac{z_i(t)_0 - z^k(t)}{\rho_i^k(t)_0} - \frac{z_i(t)_0 - z^l(t)}{\rho_i^l(t)_0}\right]\Delta Z_i(t)
\end{aligned} \tag{4.6.1}$$

The TD observation equation is given by:

$$\begin{aligned}
\delta\Phi_{ij}^{kl}(t) &= [\rho_{ij}^{kl}(t) - \rho_{ij}^{kl}(t-1)] + \delta\varepsilon_{ij,1}^{kl}(t) \\
&= \rho_i^k(t)_0 - \rho_i^l(t)_0 - \rho_j^k(t) + \rho_j^l(t) \\
&\quad + \left[\frac{x_i(t)_0 - x^k(t)}{\rho_i^k(t)_0} - \frac{x_i(t)_0 - x^l(t)}{\rho_i^l(t)_0}\right]\Delta X_i(t) \\
&\quad + \left[\frac{y_i(t)_0 - y^k(t)}{\rho_i^k(t)_0} - \frac{y_i(t)_0 - y^l(t)}{\rho_i^l(t)_0}\right]\Delta Y_i(t) \\
&\quad + \left[\frac{z_i(t)_0 - z^k(t)}{\rho_i^k(t)_0} - \frac{z_i(t)_0 - z^l(t)}{\rho_i^l(t)_0}\right]\Delta Z_i(t) \\
&\quad - \rho_i^k(t-1)_0 + \rho_i^l(t-1)_0 + \rho_j^k(t-1) - \rho_j^l(t-1) \\
&\quad - \left[\frac{x_i(t-1)_0 - x^k(t-1)}{\rho_i^k(t-1)_0} - \frac{x_i(t-1)_0 - x^l(t-1)}{\rho_i^l(t-1)_0}\right]\Delta X_i(t-1) \\
&\quad - \left[\frac{y_i(t-1)_0 - y^k(t-1)}{\rho_i^k(t-1)_0} - \frac{y_i(t-1)_0 - y^l(t-1)}{\rho_i^l(t-1)_0}\right]\Delta Y_i(t-1) \\
&\quad - \left[\frac{z_i(t-1)_0 - z^k(t-1)}{\rho_i^k(t-1)_0} - \frac{z_i(t-1)_0 - z^l(t-1)}{\rho_i^l(t-1)_0}\right]\Delta Z_i(t-1)
\end{aligned} \tag{4.6.2}$$

where (t) denotes the current epoch, $(t-1)$ denotes the previous epoch, and the subscript zeros denote the corresponding values that are evaluated by using the given approximate coordinates.

If the first epoch coordinates are given, then we have:

$$\begin{aligned}
\delta L_{ij}^{kl}(t) &:= \delta\Phi_{ij}^{kl}(t) - \left(\rho_i^k(t)_0 - \rho_i^l(t)_0 - \rho_j^k(t) + \rho_j^l(t)\right) \\
&\quad - \left(-\rho_i^k(t-1)_0 + \rho_i^l(t-1)_0 + \rho_j^k(t-1) - \rho_j^l(t-1)\right) \\
&= \left[\frac{x_i(t)_0 - x^k(t)}{\rho_i^k(t)_0} - \frac{x_i(t)_0 - x^l(t)}{\rho_i^l(t)_0}\right]\Delta X_i(t) \\
&\quad + \left[\frac{y_i(t)_0 - y^k(t)}{\rho_i^k(t)_0} - \frac{y_i(t)_0 - y^l(t)}{\rho_i^l(t)_0}\right]\Delta Y_i(t) \\
&\quad + \left[\frac{z_i(t)_0 - z^k(t)}{\rho_i^k(t)_0} - \frac{z_i(t)_0 - z^l(t)}{\rho_i^l(t)_0}\right]\Delta Z_i(t)
\end{aligned} \tag{4.6.3}$$

Analogously, the TD pseudo-range observation equation is given by:

$$\begin{aligned}
\delta P_{ij}^{kl}(t) &:= \delta P_{ij}^{kl}(t) - \left(\rho_i^k(t)_0 - \rho_i^l(t)_0 - \rho_j^k(t) + \rho_j^l(t)\right) \\
&\quad - \left(-\rho_i^k(t-1)_0 + \rho_i^l(t-1)_0 + \rho_j^k(t-1) - \rho_j^l(t-1)\right) \\
&= \left[\frac{x_i(t)_0 - x^k(t)}{\rho_i^k(t)_0} - \frac{x_i(t)_0 - x^l(t)}{\rho_i^l(t)_0}\right] \Delta X_i(t) \\
&\quad + \left[\frac{y_i(t)_0 - y^k(t)}{\rho_i^k(t)_0} - \frac{y_i(t)_0 - y^l(t)}{\rho_i^l(t)_0}\right] \Delta Y_i(t) \\
&\quad + \left[\frac{z_i(t)_0 - z^k(t)}{\rho_i^k(t)_0} - \frac{z_i(t)_0 - z^l(t)}{\rho_i^l(t)_0}\right] \Delta Z_i(t)
\end{aligned} \tag{4.6.4}$$

The TD solution may be obtained by solving equation (4.6.3) and equation (4.6.4). First, an initial approximation position is needed to compute the quantities with the subscript zero, and $\Delta X_i(t)$, $\Delta Y_i(t)$, and $\Delta Z_i(t)$ are computed by solving the linear system described by equations (4.6.3) and (4.6.4). Then an improved approximation position is obtained by adding the computed $\Delta X_i(t)$, $\Delta Y_i(t)$, and $\Delta Z_i(t)$ into the initial approximation coordinates. The procedures are repeated several times, usually less than 5, till the linear system converge. Figures 4.1 and 4.2 show the position differences between the TD solution and the presumably more precise DGPS solutions offered by the Applanix$^{\text{TM}}$ software (http://www.applanix.com).

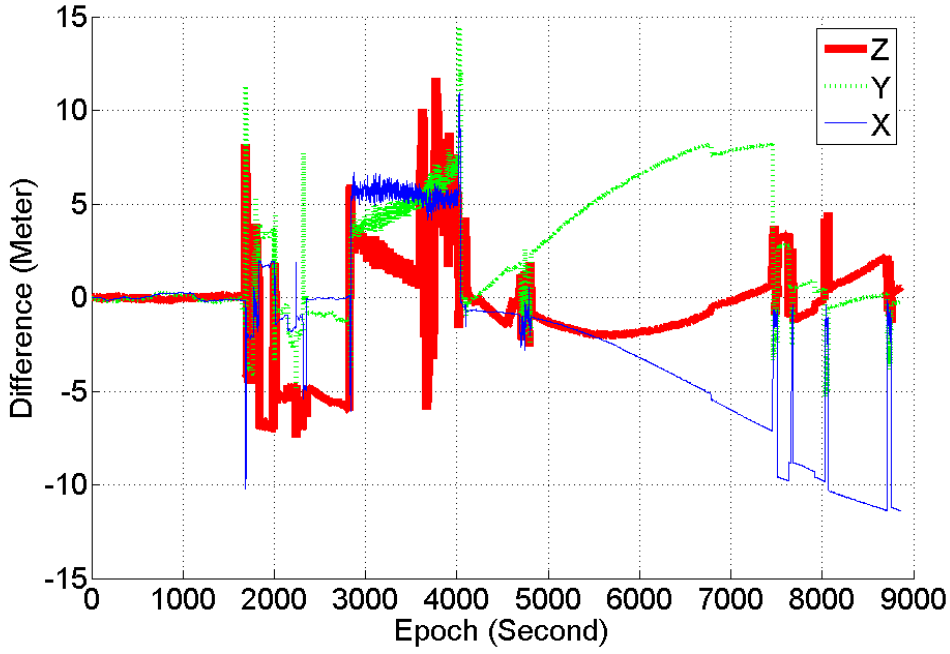

Figure 4.1: Position differences between TD solution and Applanix$^{\text{TM}}$ solution

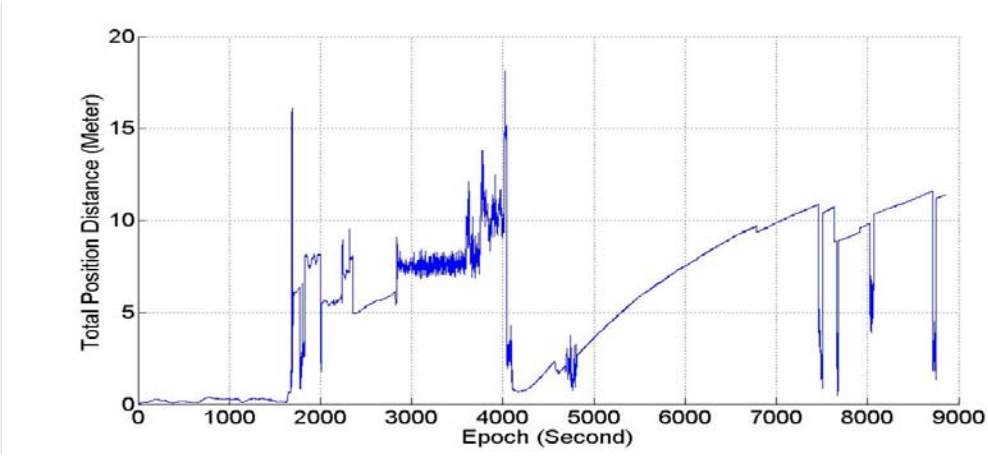

Figure 4.2: Total positioning distances between TD solution and Applanix^{TM} solution

From Figures 4.1 and 4.2, we can see that the differences are relatively small in the first 1600 seconds, when the vehicle is stationary. But the differences are getting larger in the kinematic part. The reason is that the commercial software uses a built-in Kalman filter to yield an optimal solution. The TD solution is just an epoch-by-epoch least-squares estimation; and the noise level in the TD observables is much higher than in the DD and SD observables due to the linear operations, as pointed out by many researchers. Hence, the Applanix^{TM} is used in the following data processing, when a high accuracy solution is required. However, the TD epoch by epoch solution may be better than the filtered results in the stationary case, at least in the vertical component. Indeed, Figure 4.3 shows the ellipsoidal height solution of the TD and Applanix^{TM} output when the vehicle is stationary.

4.7 Kinematic acceleration computation by phase method

This section introduces the phase method to compute the GPS acceleration. Unlike the position method, it relaxes the requirements in the positioning accuracy. Kleusberg et al. (1990), and Jekeli (1994) showed some preliminary results in the static case. Jekeli and Garcia (1997) and Kennedy (2002) presented the results in the kinematic case for the determination of gravity disturbances in the airborne gravimetric system. However, some implementation procedures such as cycle slip determination and fixing still remain vague. Here, we try to develop a clear and effective routine to obtain the GPS accelerations directly from the phase observables.

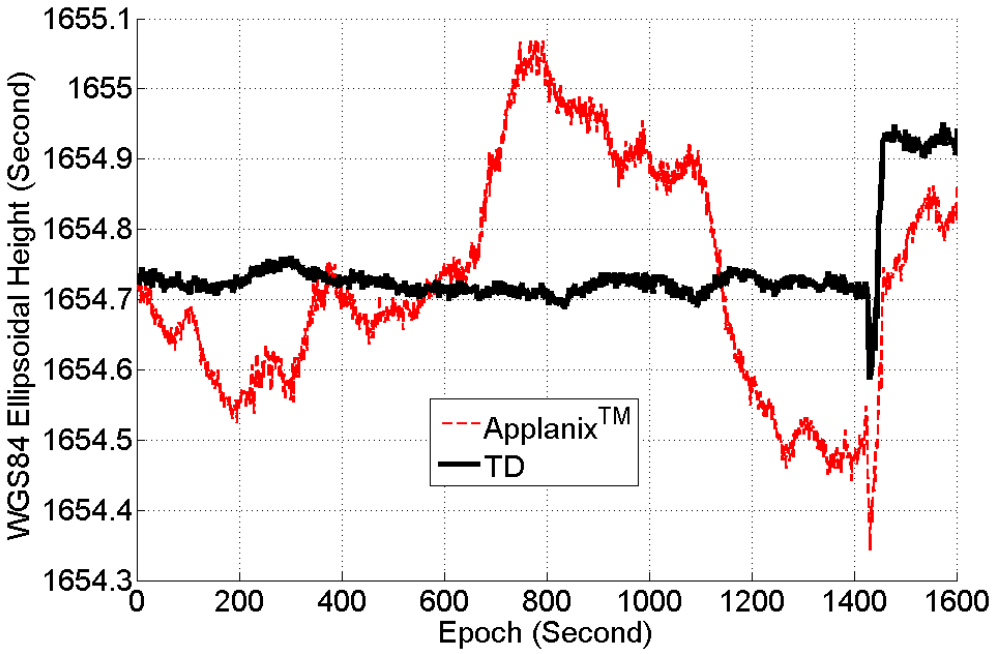

Figure 4.3: Vertical positioning results of TD solution and Applanix™ solution

From the phase acceleration algorithm in the 4-satellite scenario provided by Jekeli and Garcia (1997), an extension to more than four satellite observations is given to determine the acceleration of the rover GPS receiver in an inertial frame, as shown in equation (4.7.1).

$$\ddot{\vec{x}}_m = [E^T_{p,q;q,r;r,s;s,t;\ldots} E_{p,q;q,r;r,s;s,t;\ldots}]^{-1} E^T_{p,q;q,r;r,s;s,t;\ldots} \begin{bmatrix} a_{p,q} \\ a_{q,r} \\ a_{r,s} \\ a_{s,t} \\ \cdots \end{bmatrix} \tag{4.7.1}$$

where $\ddot{\vec{x}}_m$ is the rover acceleration in the i-frame

$$E_{p,q;q,r;r,s;s,t;\ldots} = \begin{bmatrix} \vec{e}^{\,p,q}_m \\ \vec{e}^{\,q,r}_m \\ \vec{e}^{\,r,s}_m \\ \vec{e}^{\,s,t}_m \\ \cdots \end{bmatrix} \tag{4.7.2}$$

where $\vec{e}_m^{p,q} = \vec{e}_m^{p} - \vec{e}_m^{q}$, and $\vec{e}_m^{q}$ is the unit vector along the line of sight from receiver m to satellite q.

$$\begin{bmatrix} a_{p,q} \\ a_{q,r} \\ a_{r,s} \\ a_{s,t} \\ \cdots \end{bmatrix} = \begin{bmatrix} -\ddot{\rho}_m^{p,q} + (\vec{e}_m^{p} \bullet \ddot{\vec{x}}^{p} - \vec{e}_m^{q} \bullet \ddot{\vec{x}}^{q}) + (\dot{\vec{e}}_m^{p} \bullet \dot{\vec{x}}_m^{p} - \dot{\vec{e}}_m^{q} \bullet \dot{\vec{x}}_m^{q}) \\ -\ddot{\rho}_m^{q,r} + (\vec{e}_m^{q} \bullet \ddot{\vec{x}}^{q} - \vec{e}_m^{r} \bullet \ddot{\vec{x}}^{r}) + (\dot{\vec{e}}_m^{q} \bullet \dot{\vec{x}}_m^{q} - \dot{\vec{e}}_m^{r} \bullet \dot{\vec{x}}_m^{r}) \\ -\ddot{\rho}_m^{r,s} + (\vec{e}_m^{r} \bullet \ddot{\vec{x}}^{r} - \vec{e}_m^{s} \bullet \ddot{\vec{x}}^{s}) + (\dot{\vec{e}}_m^{r} \bullet \dot{\vec{x}}_m^{r} - \dot{\vec{e}}_m^{s} \bullet \dot{\vec{x}}_m^{s}) \\ -\ddot{\rho}_m^{s,t} + (\vec{e}_m^{s} \bullet \ddot{\vec{x}}^{s} - \vec{e}_m^{t} \bullet \ddot{\vec{x}}^{t}) + (\dot{\vec{e}}_m^{s} \bullet \dot{\vec{x}}_m^{s} - \dot{\vec{e}}_m^{t} \bullet \dot{\vec{x}}_m^{t}) \\ \cdots \end{bmatrix} \tag{4.7.3}$$

$$\dot{\rho}_m^{p,q} = \dot{\rho}_{m,k}^{p,q} + \dot{\rho}_k^{p,q} \tag{4.7.4}$$

$$\ddot{\rho}_m^{p,q} = \ddot{\rho}_{m,k}^{p,q} + \ddot{\rho}_k^{p,q} \tag{4.7.5}$$

The first term of the right hand sides of equations (4.7.4) and (4.7.5) is obtained by taking derivatives of the cycle slip free DD phase observables, which can be obtained, for instance, from section 4.5.5. The second term could be computed by taking the derivatives of the range differences between the base station and the satellites, which could be computed from the given base station coordinates and the interpolated satellites coordinates.

The line of sight velocities can be obtained by using equations (4.7.6) - (4.7.9).

$$\ddot{\vec{x}}_m = [E_{p,q;q,r;r,s;s,t;\ldots}^T E_{p,q;q,r;r,s;s,t;\ldots}]^{-1} E_{p,q;q,r;r,s;s,t;\ldots}^T \begin{bmatrix} b_{p,q} \\ b_{p,r} \\ b_{p,s} \\ b_{p,t} \\ \cdots \end{bmatrix} \tag{4.7.6}$$

where

$$E_{p,q;p,r;p,s;p,t;\ldots} = \begin{bmatrix} \vec{e}_m^{p,q} \\ \vec{e}_m^{p,r} \\ \vec{e}_m^{p,s} \\ \vec{e}_m^{p,t} \\ \cdots \end{bmatrix} \tag{4.7.7}$$

$$\begin{bmatrix} b_{p,q} \\ b_{p,r} \\ b_{p,s} \\ b_{p,t} \\ \cdots \end{bmatrix} = \begin{bmatrix} \dot{\rho}_m^{p,q} - \vec{e}_m^{q} \bullet (\dot{\vec{x}}^{p} - \dot{\vec{x}}^{q}) \\ \dot{\rho}_m^{p,r} - \vec{e}_m^{r} \bullet (\dot{\vec{x}}^{p} - \dot{\vec{x}}^{r}) \\ \dot{\rho}_m^{p,s} - \vec{e}_m^{s} \bullet (\dot{\vec{x}}^{p} - \dot{\vec{x}}^{s}) \\ \dot{\rho}_m^{p,t} - \vec{e}_m^{t} \bullet (\dot{\vec{x}}^{p} - \dot{\vec{x}}^{t}) \\ \cdots \end{bmatrix} \tag{4.7.8}$$

Finally, we use equation (4.7.9) to compute the derivative of the unit vector.

$$\dot{\vec{e}}_m^p = \frac{1}{\rho_m^p}(I - \vec{e}_m^p(\vec{e}_m^p)^T)\dot{\vec{x}}_m^p \tag{4.7.9}$$

To perform the computation, first, we need the position of the rover receiver and the position of the satellites. Second these coordinates are transformed into a predefined inertial frame. Then, we take the derivatives of these i-frame coordinates and the DD phase observables. Finally, the rover acceleration in the i-frame is computed based on the flow chart in Figure 4.4.

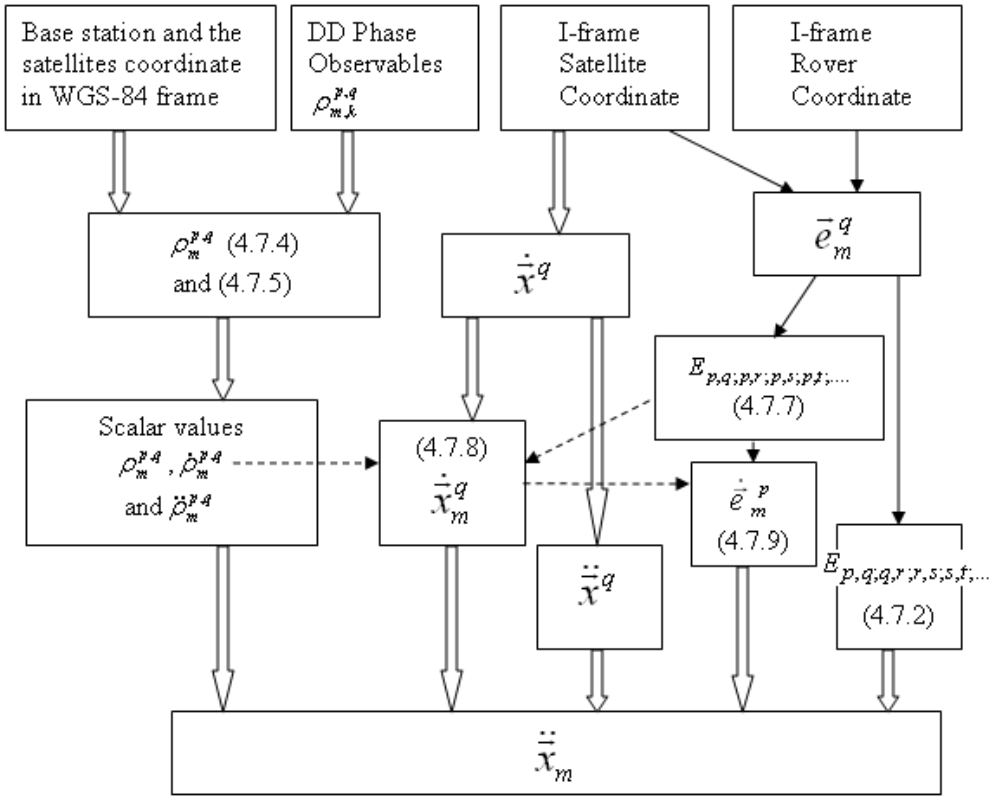

Figure 4.4: Flow chart of the phase method of determining kinematic vehicle acceleration

4.8 Acceleration computation tests

The rover GPS acceleration can be computed either by using the phase method described in the previous section or by taking two consecutive time derivatives of the position results, i.e. the position method, which is straightforward to implement once the high precision position solution is available. But in practice it is very challenging to obtain the required precision solution at all times. As a result, the phase method becomes a good alternative. In this section, the phase method is tested first by using static data; then it is applied to kinematic data. From the static data test result, we can check the algorithm and computer code. The kinematic results show that it is possible to improve the accuracy of the position-derived acceleration by incorporating the phase-derived acceleration.

4.8.1 Static data test

To test the algorithm, a set of static observation data from two CORS stations, MSOL and INDP, is used. The data were collected on June 15, 2005 at these two sites which are approximately 190 Km apart. These data sets are accessible to the public at the NGS ftp server. To simulate the situation, we chose the GPS receiver at MSOL as the base station in the DD mode, but the receiver at INDP is assumed to be a rover. The commonly viewed satellites at both ends of the baseline are shown in Figure 4.5.

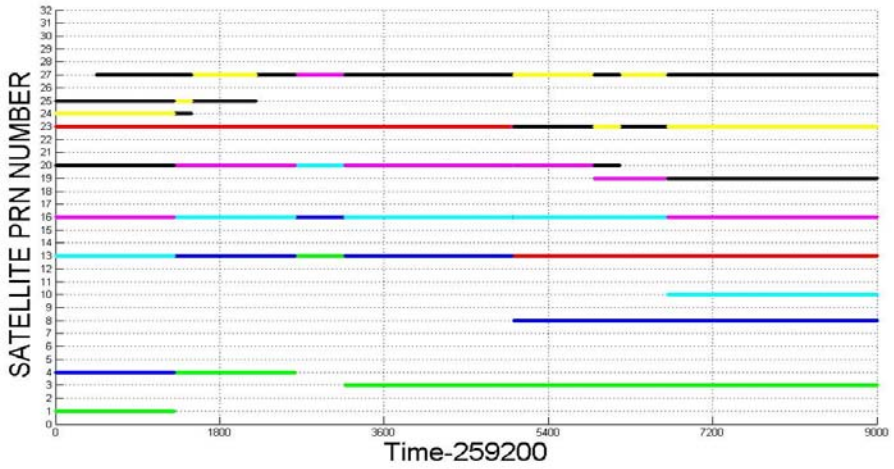

Figure 4.5: Common satellites observed at MSOL and INDP

Diff (mGal)	X	Y	Z
Mean	−1.461	−0.544	0.048
STD	230.787	359.164	241.626

Table 4.1: Statistics of the acceleration differences between the L1 phase determined GPS acceleration and the true acceleration.

In Figure 4.5, we can see that the total number of commonly viewed satellites is changing with respect to time. To reflect this, the color of each PRN satellite is used to indicate the change of satellite constellation. Based on this figure, PRN23, PRN13, PRN16, PRN20, and PRN27 are selected as the common-view satellites (from 1800 seconds to 5400 seconds after 259200 seconds of the week). The point positioning method is applied at both MSOL and INDP to estimate the receiver clock error and thus synchronize the receiver clocks to the GPST. Then the ionosphere-only linear combination is used to detect the cycle slips in the phase observables. Figure 4.6 shows the ionosphere-only solution for the selected satellites. We can see that the amplitudes of the ionosphere-only linear combinations in Figure 4.6 do not have large jumps ($> \lambda_2$), which implies that no cycle slip happened in this period of time. As a result, for the selected static data set, it is not necessary to use the Kalman filter, described in section (4.5.5). The rover acceleration (i.e., the INDP CORS station acceleration) in the i-frame is computed by use of the L1 phase observation, and is plotted in Figure 4.7.

The computed acceleration components are shown by the thick solid(blue) lines. The true acceleration of the "rover" in the i-frame can be easily obtained by using the mean Earth rotation rate and INDP's coordinates. The differences between the phase acceleration and nominal acceleration, indicated by the thin lines, are due to the observation errors. The statistics of the differences are shown in Table 4.1. On the other hand, the position method is also used to compute the accelerations. First, we use the Trimble Geomatics Office (TGO^{TM}) to compute the coordinates of the "rover" GPS receiver at INDP at every epoch in the selected time interval. Then the solutions are transformed into the i-frame. And the accelerations are obtained by take two consecutive derivatives of the computed i-frame coordinates, which are also include in Figure 4.7, from which we can see the precision of the position method generated acceleration is much worse than the phase method derived acceleration. The main reason is due to the very long base line (around 200km) between MSOL and INDP.

Diff (mGal)	X	Y	Z
Mean	−4.329	−4.636	2.513
STD	372.371	492.863	379.547

Table 4.2: Statistics of the acceleration differences between the L2 phase determined GPS acceleration and the true acceleration.

The acceleration could also be computed by using L2 phase observables. The results are shown in Figure 4.8. The statistics of the accelerations errors by use of L2 data are shown in Table 4.2. From Tables 4.1 and 4.2, we can see that the L1 data give a better solution than the L2 data, which makes sense because the wavelength of L1 is shorter than the wavelength of L2.

4.8.2 Kinematic data

The next step is to compute acceleration from some actual kinematic data. We select the same GPS data set that we used in Section 3.5 (refer to Chapter 6 for more details of the data set). The MSOL CORS station is still used as the base station in the DD model. The selected common satellites viewed at both ends of the base-line are shown in Figure 4.9.

After synchronizing the GPS receivers, the DD observables are constructed so that the cycle slips could be detected and validated using the method described in Section 4.5.5. The ionosphere-only linear combinations of the DD observables constructed by the selected satellites are shown in figure 4.10.

Figure 4.10 shows significant cycle slips in the observed phases, which need to be resolved and fixed. Furthermore, we can see that some cycle slips in $\nabla\Delta\Phi_{15,18}$, $\nabla\Delta\Phi_{18,26}$, and $\nabla\Delta\Phi_{15,26}$ occurred within very short time intervals. Apparently, there are not enough data to perform the filtering or smoothing between these cycle slips. As a result, the observation errors in the range residuals or wide-lane phase minus narrow-lane pseudo-range linear combinations can not be reduced by the conventional methods. The Kalman filter developed in Section 4.5.5 is used to reduce the noise level in the pseudo-ranges so that the wide-lane-phase-minus-narrow-lane-pseudo-range linear combination can be used together with the ionosphere-only linear combination to validate the cycle slips in both L1 and L2 frequencies. The residuals of the Kalman filtered pseudo-ranges are plotted in Figure 4.11. Figure 4.12 shows the wide-lane-phase-minus-narrow-lane-pseudo-range linear combinations based on these filtered pseudo-ranges.

After fixing the cycle slips by using equations (4.5.22) and (4.5.23), the ionosphere-only linear combinations are shown in Figure 4.13. Comparing Figures 4.10 and 4.13, we can see that the large jumps in the ionosphere-only linear combinations are eliminated. This proves that our new cycle slip fixing algorithm works well, even under extremely bad observation conditions, where the conventional cycle slip fixing techniques do not work. It is true that there are still some jumps in Figure 4.13, which may be due to the round-off error in equations (4.5.22) and (4.5.23). But they are much smaller than any GPS frequency wavelength, and their effects on computing the phase accelerations should not be significant.Finally, these cycle-slip-free phase observables are used in equations (4.7.4) and (4.7.5) to compute the derivatives of the phase data, which eventually leads to the acceleration of the GPS receiver following by the steps in Figure 4.4.

On the other hand, the accelerations also can be computed by using the position method which takes derivatives of the provided GPS coordinates. However, the data gaps in the position solution should be fixed by using the TAEKF. To yield better results, the final GPS kinematic acceleration is determined by combining these accelerations in the frequency domain via the wave number correlation filter (see section 5.3.2 for details). The results are shown in Figures 4.14 - 4.16.

In Figures 4.14 to 4.16, the dotted(red) lines are the position derived GPS acceleration, the dashed(blue) lines are the phase method provide GPS acceleration, and the solid(green) lines are the correlated GPS acceleration. Both the position derived GPS acceleration and the phase determined GPS acceleration show high frequency noises. In the kinematic scenario, neither of these methods provides apparently better results than the other. As we have already seen, the position method is very straight forward once obtaining the precise positioning solutions, while the phase method involves much more computations, especially for a long period of observation time, in which we have to change the satellite constellations from time to time to yield better results. But these repeated and independent accelerations at least can serve as a reference to each other to prevent major computation blunders.

The histograms of the differences between the phase acceleration and the position acceleration are shown in Figure 4.17, which in general show normal random distributions. We also find that the noise is essentially white. Hence, the wave-number correlation method can be employed to filter out the uncorrelated signals in these two kinds of accelerations. The better conditioned GPS acceleration is then used to estimate the gravity disturbances in Chapter 5.

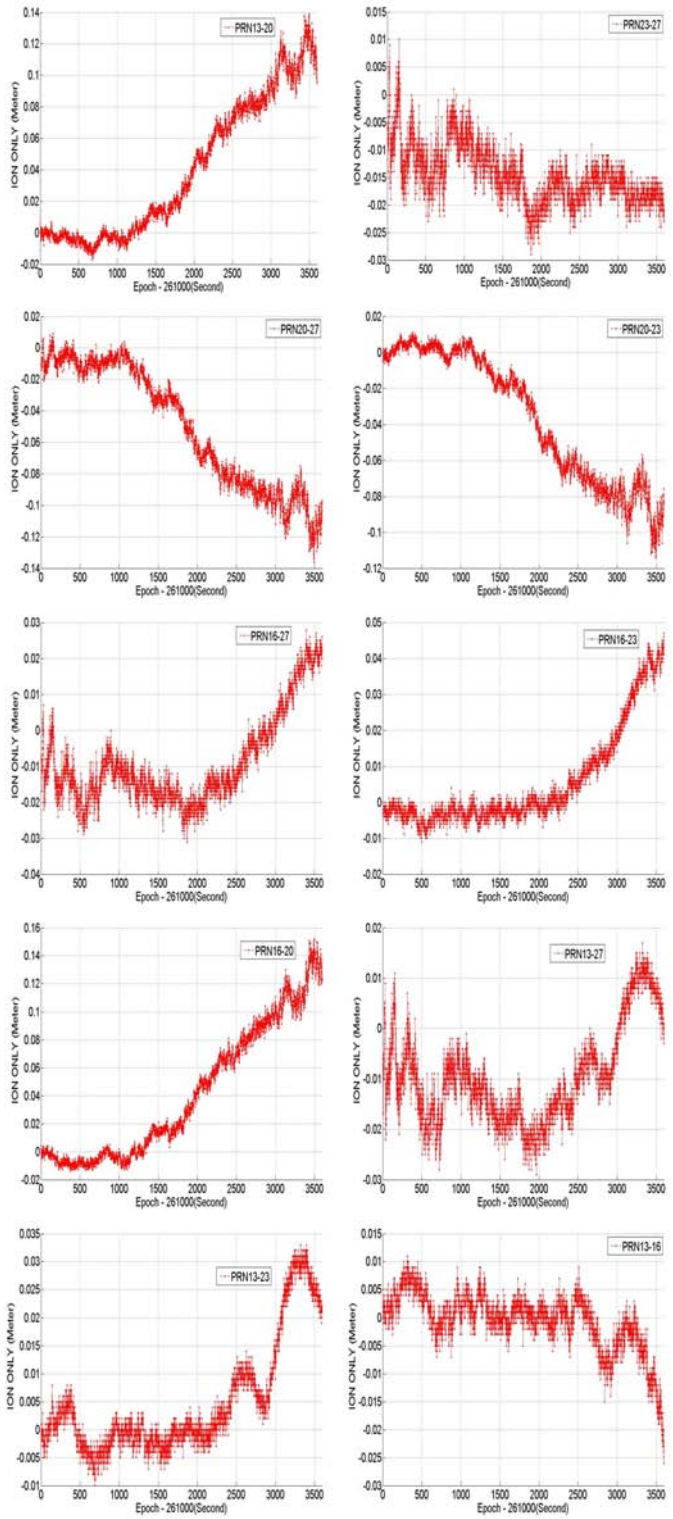

Figure 4.6: Ionosphere-only linear combinations of DD observables of the static data collected at MSOL and INDP

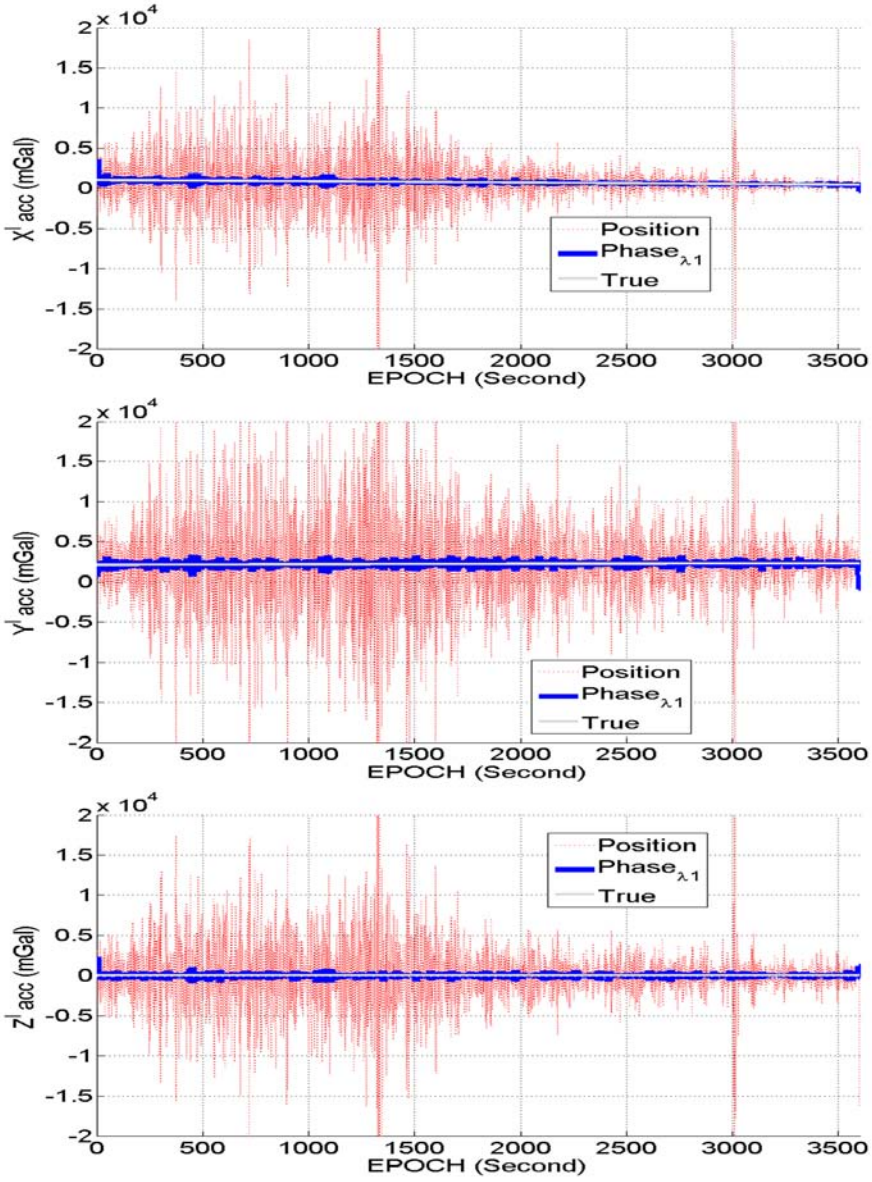

Figure 4.7: Acceleration results by using L1 phase observables

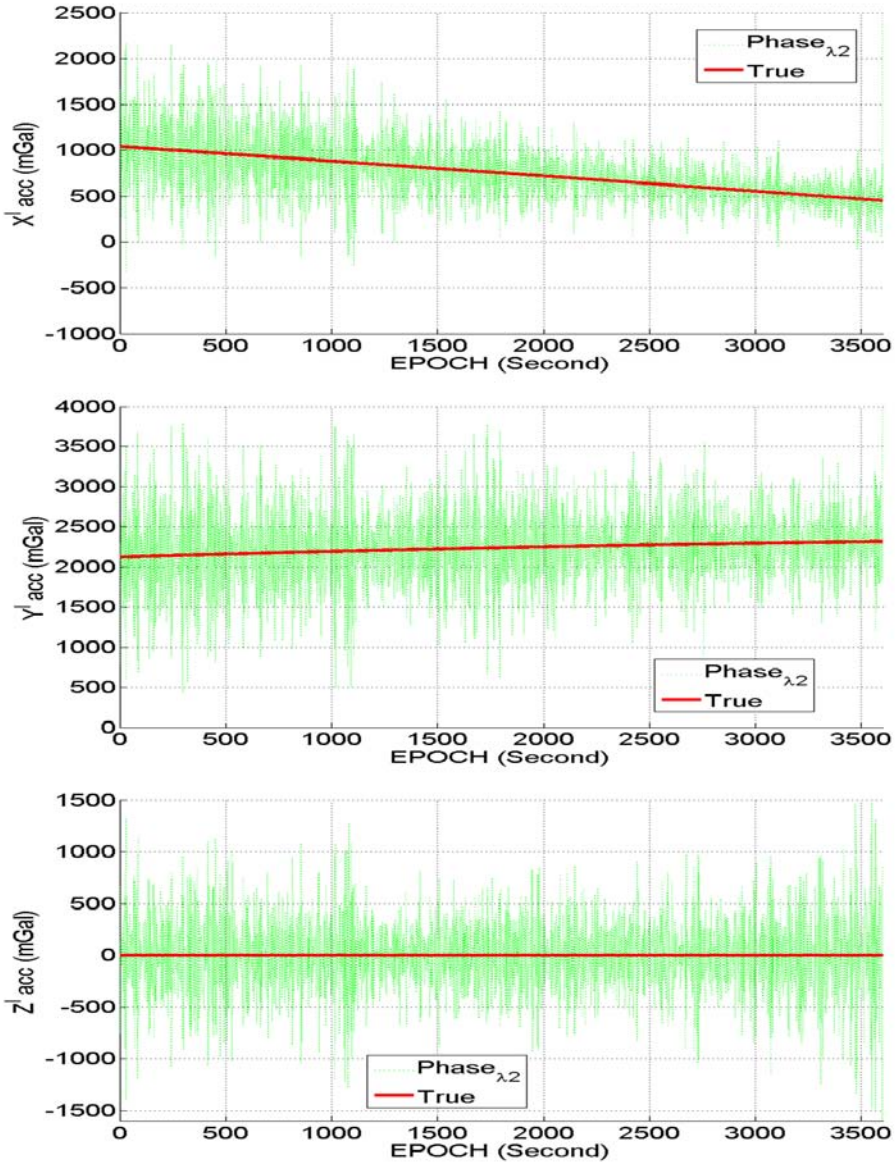

Figure 4.8: Acceleration results by using L2 phase observables

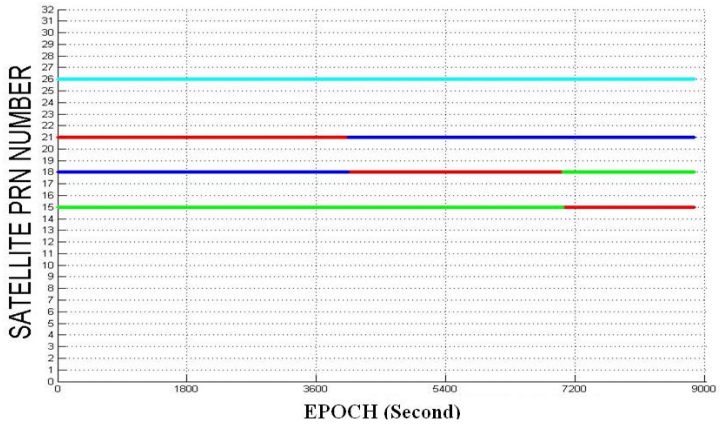

Figure 4.9: Satellites observed at both ends of the base-line in the kinematic case

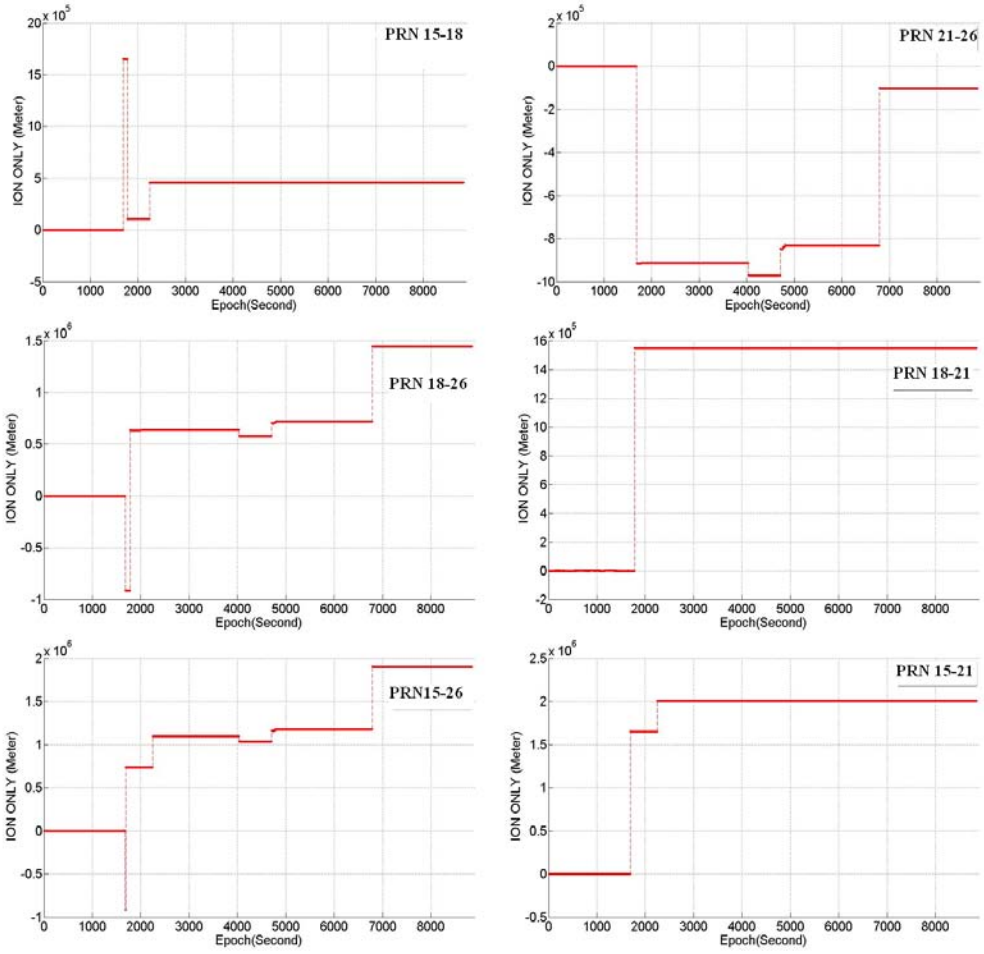

Figure 4.10: Ionosphere-only linear combination of the kinematic data before fixing cycle slips

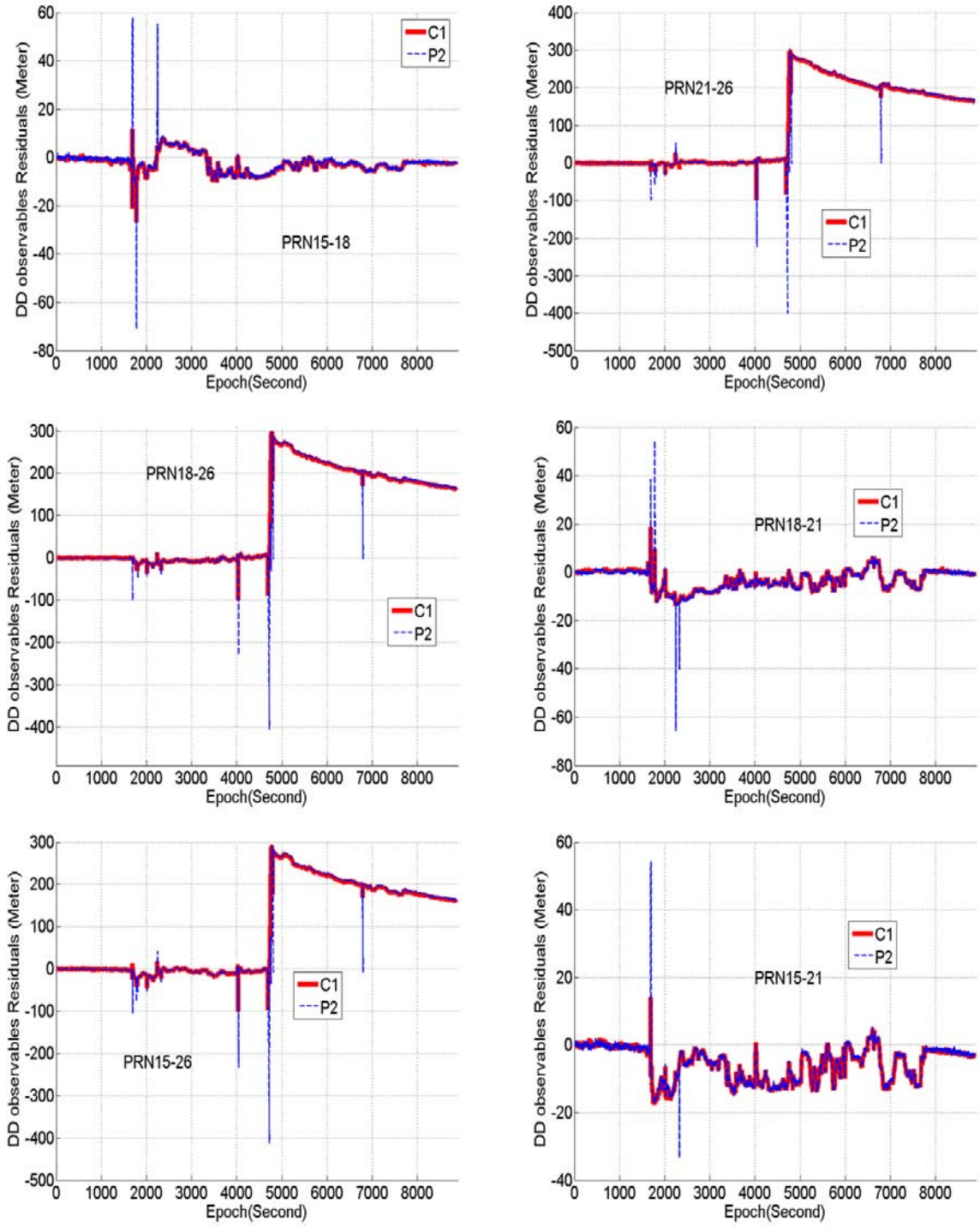

Figure 4.11: Kalman residuals of the pseudo-ranges

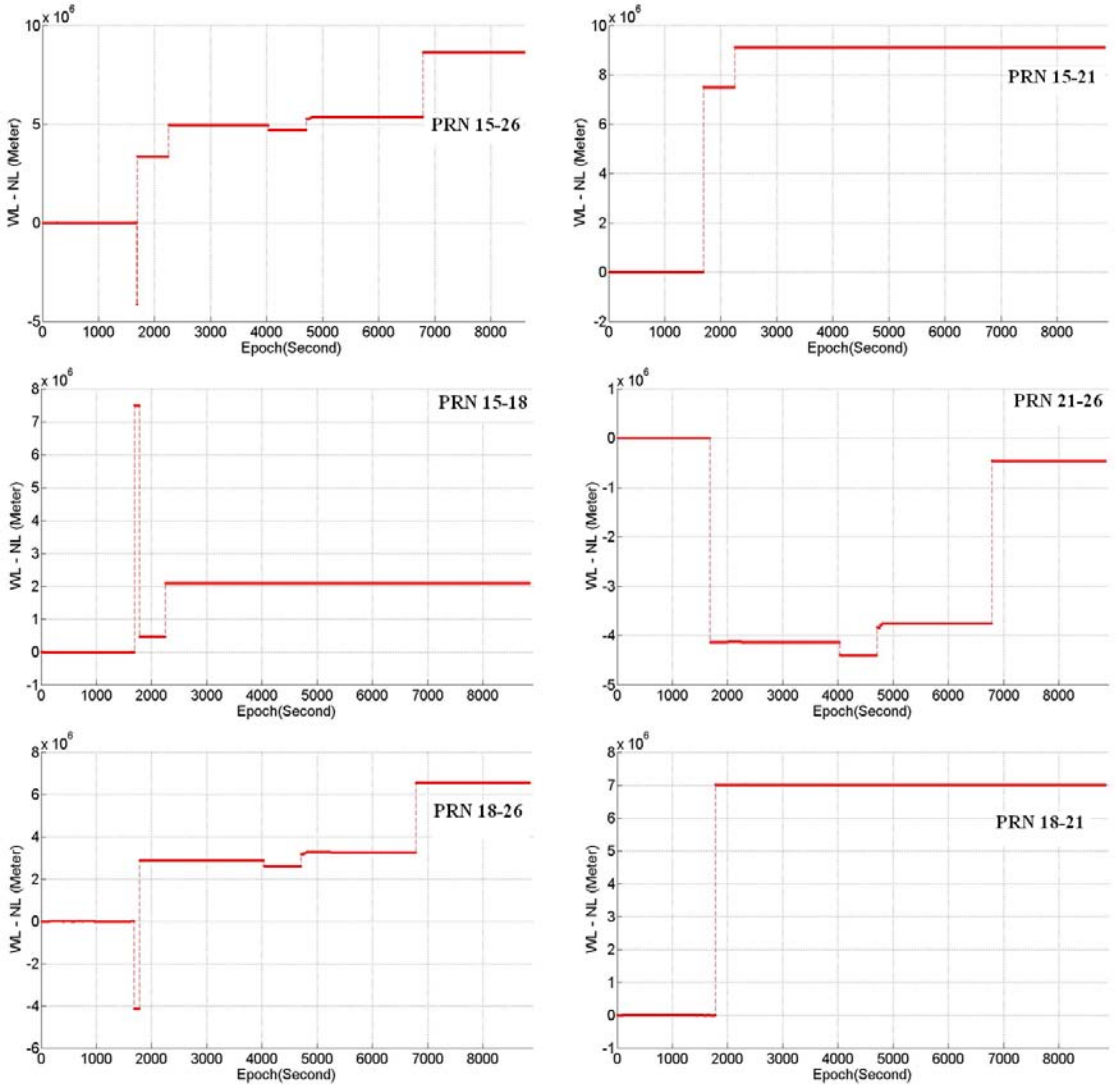

Figure 4.12: Wide lane phase minus narrow lane pseudo-range

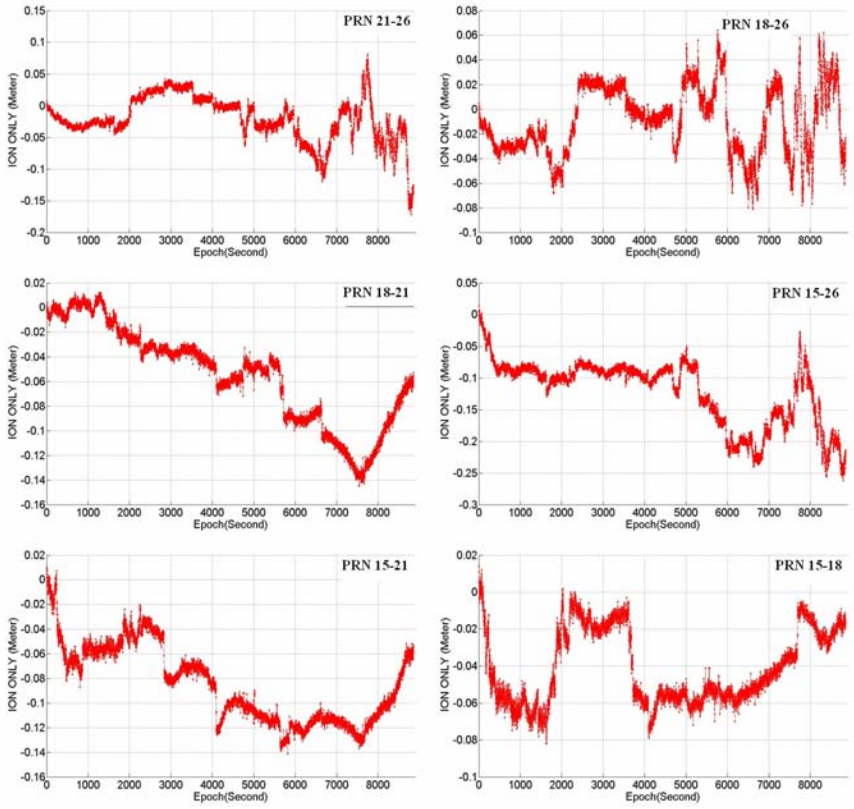

Figure 4.13: Ionosphere-only linear combinations of the kinematic data after fixing cycle slips

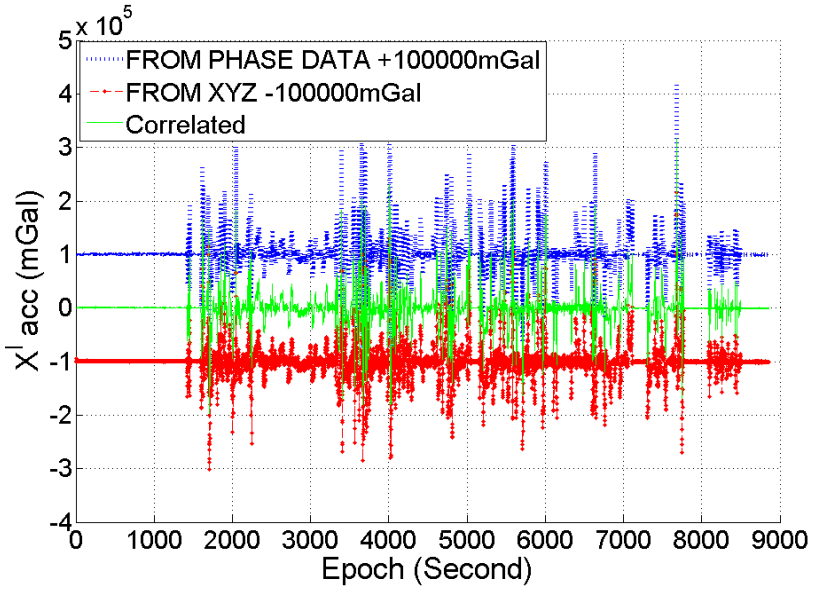

Figure 4.14: X-component kinematic acceleration in the i-frame

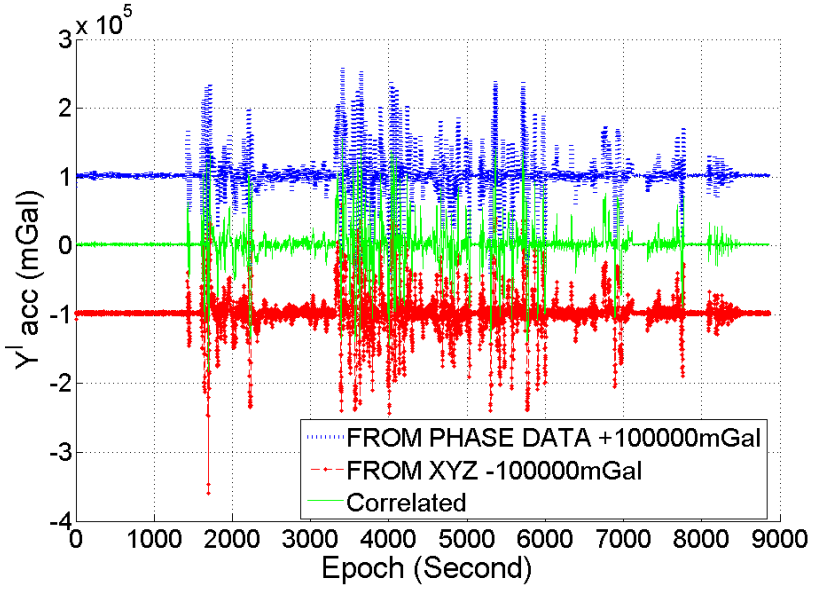

Figure 4.15: Y-component kinematic acceleration in the i-frame

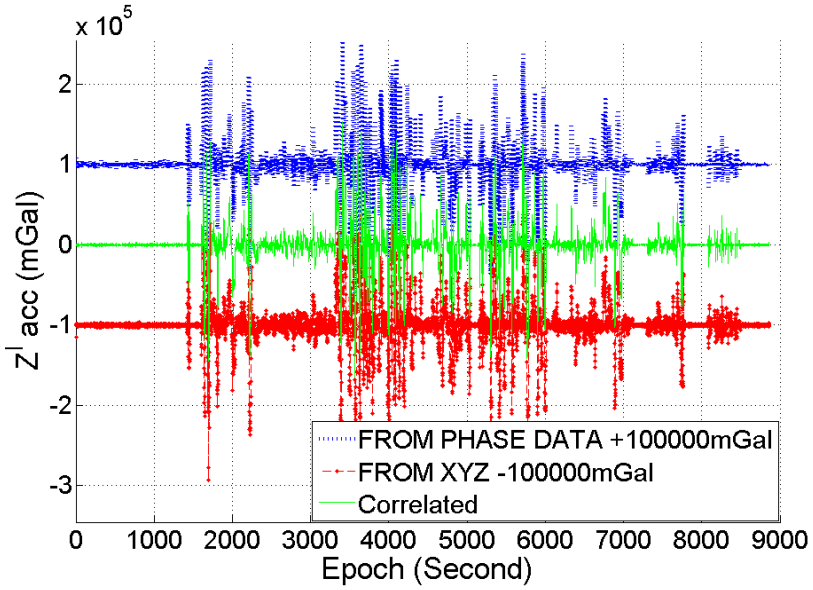

Figure 4.16: Z-component kinematic acceleration in the i-frame

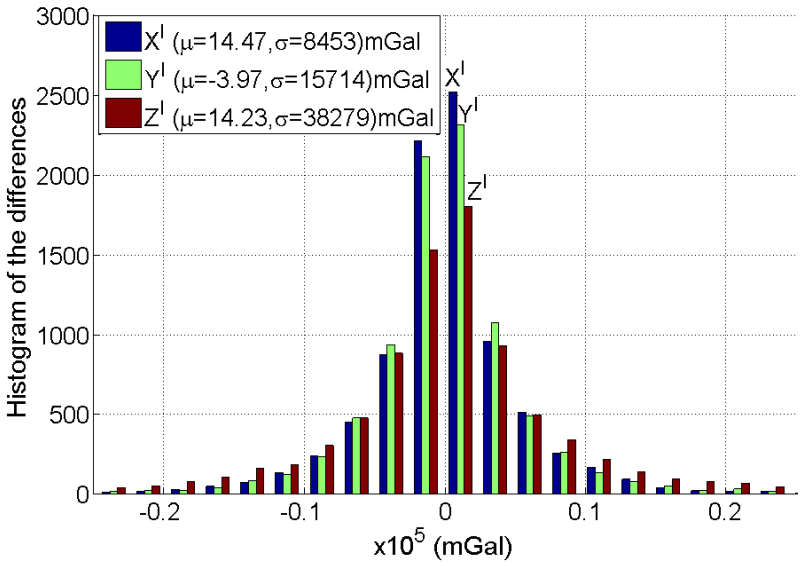

Figure 4.17: Statistics of the acceleration differences

CHAPTER 5

GPS/SINS VECTOR GRAVIMETRY

In Chapter 4 the long wavelength errors in the dynamic acceleration are removed by the TAEKF estimated IMU biases and scale errors. The precision of the kinematic acceleration is improved by combining the phase determined acceleration and the position derived acceleration. However, the noise level in the accelerations is still much higher than the gravity disturbance signal. It is well known that the gravity disturbance vector generally does not exceed a few hundred mGal in each component over a distance of about 100km (Kwon 2000), while the non-gravitational accelerations can be larger than the gravity disturbance signal by factors of 100 to 1000, as reported by Hannah (2001), among others. As a result, it is necessary to employ advanced techniques to obtain the gravity disturbance from the noisy acceleration observations.

5.1 Introduction

Isolation of the target gravity signal from the effects of motion noise is the primary challenge in a moving base gravimetric system. The techniques described in the previous chapter mainly focused on improving the robustness of the individual systems. For example, the TAEKF described in Chapter 3 can fix the position gaps in the GPS solutions. The phase method introduced in Chapter 4 provides alternatives in determining GPS acceleration. However, the noise level in the raw observations can not be reduced significantly enough with these methods to let the gravity disturbance vectors stand out directly. Further data processing is necessary to separate the gravity disturbance signals from these observables in such a low signal-to-noise-ratio (SNR) system. From the previous airborne gravimetry studies conducted by Jekeli and Kwon (Jekeli and Kwon, 1999; Kwon, 2000; Kwon and Jekeli, 2001), we know that the B-spline smoother very efficiently reduces the high frequency noises in both the GPS acceleration and the INS acceleration, and the modified Kalman filter (Kwon and Jekeli, 2001) could provide a preliminary estimate of the gravity disturbances. However, we know that the success of separating the gravity disturbances

from the noisy accelerations in certain frequency bands (corresponding roughly to spatial resolutions between 2km and 100km) is based on the following assumptions: first, the gravity signal dominates the noise in the long wavelengths, even though there are long-wavelength errors in the system; second, the noise is primarily restricted to shorter wavelength and can be removed by low-pass filtering.

However, in the terrestrial moving base system, due to the lower altitudes, compared to the airborne system, the shorter wavelength gravity signal is intensified. For instance, compared to gravity at 1000m altitude, the relative increase of gravity at resolution of 20km (harmonic degree complete to 1000) at ground level is about 17% (Figure 5.1). As a result, the high frequency band may contain both the observation noise and a significant part of the true gravity signal. A careful combination of the signal processing techniques is very important to obtain precise results with high resolution. Computation tests show that the B-spline smoothing method nevertheless should be applied first to effect a consistent comparison of the GPS and INS accelerations. Then the wavelet de-noising method is employed to isolate the gravity signal from the preliminary estimates provided by the modified Kalman filter. By using the de-noising method, even in the low speed scenario, the B-spline smoother does not need an extra large window (greater than 200 seconds) to reduce the high frequency noises. Thus, we can still preserve certain part of the high frequency signal in the gravity disturbance estimates. The wave-number correlation method can also be applied to further improve the precision of the gravity disturbance estimation if we have repeated estimates along the same traverses.

To validate the precision of the results, we have to interpolate the ground control data onto the points where the estimates are. Based on intensive computational tests, in the survey area, the multiquadrics interpolation method shows advantages over other methods, such as the Least Square Collation method, which suffers from the ill conditioned covariance matrix of the control data.

5.2 Basics of GPS/SINS gravimetry

In the local north-east-down (NED, n)-frame, the gravitational acceleration, $\vec{g}^n$ is obtained according to Newton's second law of motion, with appropriate rotations applied (Jekeli, 2000):

$$\tilde{\vec{g}}^n = C_i^n(\ddot{\vec{x}}^i - \hat{C}_b^i \hat{\vec{a}}^b) \tag{5.2.1}$$

where C_i^n is the rotation matrix from the i-frame to the n-frame and $\ddot{\vec{x}}^i$ is the total kinematic acceleration in the i-frame, both obtained from GPS (see Chapter 4); $\hat{C}_b^i$ is the rotation matrix from the b-frame to the i-frame, and $\hat{\vec{a}}^b$ is the specific force

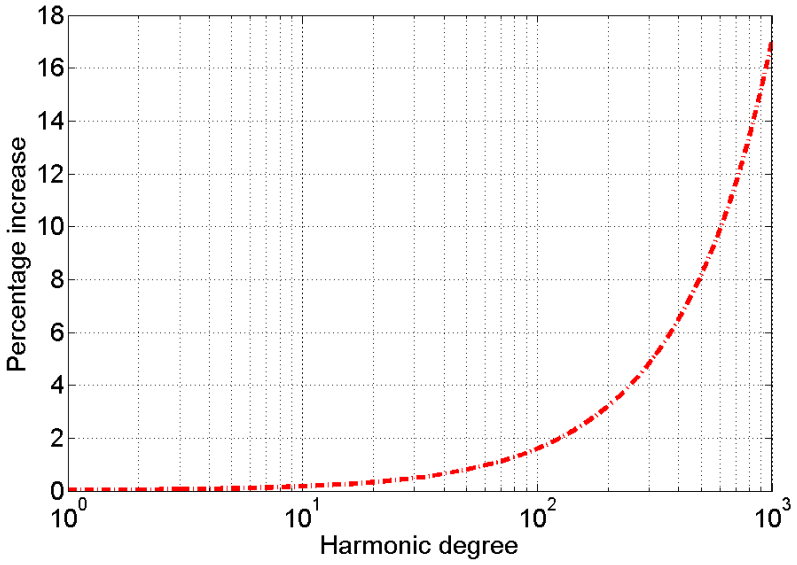

Figure 5.1: Relative increase in gravity by harmonic degree if the altitude decreases 1000m near the Earth's Surface

in the body frame, both determined from calibrated inertial sensor measurements (see chapters 3 and 4). The techniques described in Chapter 3 and Chapter 4 provide continuous GPS and INS accelerations for determining the gravity disturbance vector, which is given by.

$$\delta\tilde{\vec{g}}^n = \tilde{\vec{g}}^n - \gamma^n \tag{5.2.2}$$

where γ^n is the normal gravitation (normal gravity corrected for the centrifugal term associated with Earth's rotation). In practice, the low SNR of the gravity disturbance relative to the system errors makes it difficult to identify the gravity disturbances directly from equations (5.2.1) and (5.2.2).

To reduce the high frequency noise, previous studies of a number of low-pass filters such as the resistor-capacitor filter, Gaussian filter, and Butterworth filter, etc, (Kwon 2000, Kwon and Jekeli 2001) have shown that the B-spline smoother is a very efficient choice to reduce the noise in the GPS and INS accelerations. However, in the grand vehicle system, the relatively low speed and complicated dynamics introduce much more noises than in the airborne scenario. As a result, a 180-second, instead of 60-120 seconds (normally used in the airborne system), window size B-spline smoother is used to reduce the noises both in $\ddot{\vec{x}}^i$ and in $\hat{C}_b^i\hat{\vec{a}}^b$. After this, the modified Kalman

filter developed by Kwon and Jekeli (2001) is used to obtain a preliminary estimate of the gravity disturbance. The states of this filter include constant biases, b_g, b_a, and scale factor errors, κ_g, κ_a, for each of the gyros and accelerometers, respectively, as well as the orientation errors, Ψ, of the system. The following linear state-propagation model is formulated for these states:

$$X_k = \Phi X_{k-1} + \varepsilon \quad k = 1, 2, \ldots, \tag{5.2.3}$$

where k is a time index and

$$X_k = \begin{pmatrix} b_a^T & b_g^T & \kappa_a^T & \kappa_g^T & (\Psi^i)^T \end{pmatrix}^T \tag{5.2.4}$$

The TAEKF developed in Chapter 3 can provide the initial statistics of the state vector, if the *a priori* information of the system errors is not available. For example, the initial accelerometer biases of the SR43 data (collected on June 15 2006) can be obtained from Figures 3.10-3.15 (end value of the blue line). The differences between the smoothed GPS and INS accelerations are used to relate the filter states and the gravity disturbance as shown in equation (5.2.5).

$$\vec{y}_k := \text{smoothed}(\ddot{\vec{x}}^i) - \text{smoothed}(\hat{C}_b^i \hat{\vec{a}}^b) - \gamma^n = HX_k + \delta\vec{g}_k^i + \delta\ddot{\vec{x}}_k^i \tag{5.2.5}$$

where H is the observation matrix and the last term is the assumed white noise in the observed GPS acceleration. The specific construction of matrices H and Φ is in Appendix B (see Kwon 2001 for details). The observation is computed from the smoothed GPS acceleration and the smoothed INS accelerations as well as the normal gravity, as shown in equation (5.2.6):

$$\tilde{\vec{y}}_k = \ddot{\tilde{\vec{x}}}_k^i - \hat{\vec{a}}_k^i - \gamma_k^i. \tag{5.2.6}$$

Instead of modeling the gravity disturbance components in the states of the system (which has been done with mixed results; Schaffrin and Kwon, 2002), they are included in the observation residuals of the filter, given by:

$$\Delta\tilde{\vec{g}}_k^i = \tilde{\vec{y}}_k - H\hat{X}_k = \delta\vec{g}_k^i + \delta\ddot{\vec{x}}_k^i - C_b^i\varepsilon^b \tag{5.2.7}$$

where ε^b is the IMU processing error (Jekeli, 2000). The gravity disturbance estimate is thus:

$$\Delta\hat{\vec{g}}_k^n = C_i^n \Delta\tilde{\vec{g}}_k^i \tag{5.2.8}$$

where errors in the rotation matrix, C_i^n (depending only on position coordinates), can be neglected.

5.3 Wavelet De-noising and Wave-Number Correlation

From equations (5.2.8), and (5.2.7), it is clear that the errors in the estimated gravity disturbances are commingled with the GPS acceleration errors and the IMU processing errors. The differentiation operations which are used to calculate the GPS accelerations, as well as the road dynamics of the vehicle tend to concentrate the GPS acceleration error at the higher frequencies, where also some significant gravity disturbance signals reside (since the gravity disturbance is estimated at ground-level, rather than at altitude where field attenuation would ameliorate this concern). Therefore, extra efforts are needed to isolate the gravity disturbances from these errors.

We employ two steps to identify and isolate the gravity disturbance signal within the residuals. First, the wavelet de-noising approach (Donoho and Johnstone, 1994; Donoho and Johnstone, 1995) is used to reduce the noise across the entire spectrum. Because wavelet de-noising can localize the noise and does not have spectrum leakage (Li and Jekeli, 2004), the SNR at each frequency is improved, which simplifies the next step. Second, a wave-number correlation approach attempts to extract the gravity disturbance signal from background errors by comparing the estimates from repeated traverses (Kwon and Jekeli, 2001).

5.3.1 Wavelet De-noising

Unlike the traditional smoothing operators which remove high frequencies and retain low frequencies, wavelet de-noising attempts to remove whatever noise is present and retain whatever signal is present regardless of the frequency content of the signal. This section briefly recalls the general procedure of wavelet shrinkage de-noising. More can be found in (Donoho and Johnstone, 1994; Donoho and Johnstone, 1995 Taswell 2000, Taswell 2001). Assume that we can decompose the Kalman residuals into the following two parts

$$\Delta\hat{\vec{g}}^n_k = \delta\vec{g}^n_k + G_k \tag{5.3.1}$$

in which G_k is an additive Gaussian noise, $\delta\vec{g}^n_k$ is the gravity disturbance signal, both at sample point k. Let $W\{\bullet\}$, and $W^{-1}\{\bullet\}$ denote the forward and inverse wavelet transform operators respectively. Let $D\{\bullet, \lambda\}$ denote the de-noising operator with soft threshold λ. The wavelet shrinkage de-noising recovers $\delta\breve{\vec{g}}^n_k$ as an estimation of $\delta\vec{g}^n_k$ by the following three steps.

i. Linear forward wavelet transform

$$Y = W\{\Delta\hat{\vec{g}}^n_k\} \tag{5.3.2}$$

where Y represents the wavelet coefficients, $\Delta\hat{\vec{g}}_k^n$ is the n-frame Kalman residual from equation (5.2.8). As pointed out by Strang (1989) and Daubechies (1992), the choice of wavelet transform is essentially a choice of filter. However, there are no noticeable differences in the results by using several different kinds of base wavelets such as the Daubechies wavelet and Symlets wavelet. This agrees with the statements made by Bruton et al. (2000) and Li and Jekeli (2004), even though the wavelet de-noising is used for different purposes. For more details about the construction of wavelet, see Strang and Nguyen (1996), and Nassar and El-Sheimy. (2005).

ii. De-noising by Shrinkage

In the second step, the de-noising operator $D\{\bullet, \lambda\}$ will process the wavelet coefficient with soft threshold λ:

$$Z = D\{Y, \lambda\} \tag{5.3.3}$$

$$\text{where} \quad D\{Y,\lambda\} = \begin{cases} \text{sgn}(Y)(|Y| - \lambda) & \text{if } |Y| \geq \lambda \\ 0 & \text{if } |Y| < \lambda \end{cases}$$
$$\lambda = d(Y)$$

$d(Y)$ defines the threshold corresponding to Y according a given principle such as RiskShrink, VisuSrhink, SureShrink, and Hybrid SureShrink, developed principally by Donoho and Johnstone(1994, 1995). They introduced RiskSrhink with the min-max threshold, and VisuShrink with a universal threshold for all levels of decomposition (i.e. level of resolution) from fine to coarse. They also introduced the SureShrink threshold which is a local threshold estimated adaptively for each level of decomposition, and the Hybrid SureShrink to deal with the situation of extreme sparsity of wavelet coefficients (Taswell 2001). Among them, the Hybrid SureShrink is simple to implement and has broad adaptivity properties. This threshold selection scheme is essentially a combination of universal threshold ($\sqrt{2log(length\ of\ the\ data)}$) and SureShrink threshold, which is based on Stein's Unbiased Risk (see Donoho and Johnstone 1995 for details). The threshold is set to universal in dense situations and to SureShrink in sparse situations to yield the best performance.

iii. Linear inverse wavelet transform

Finally, in the third step, the processed wavelet coefficients are transformed from the wavelet domain back into the original domain with the same wavelet bases as used in the first step. And the estimate of $\delta\vec{g}_k^n$ is obtained by equation (5.3.4):

$$\delta\check{\vec{g}}_k^n = W^{-1}\{Z\} \tag{5.3.4}$$

From the above procedures, one can see that the wavelet de-noising does not require any assumptions about the nature of the signal. Furthermore, it permits discontinuities and non uniform spatial variation in the signal. So even if the data are not

uniformly distributed in time or space domain, this method still works. The wavelet transform maps white noise in the signal domain to white noise in the transform domain. Thus, while signal energy becomes more concentrated into fewer coefficients in the transform domain, noise energy does not. This is the important principle that enables the separation of signal from noise in the wavelet domain. Thus it works independently from the frequency domain analysis, which allows preserving the signal at every frequency band (Taswell 2001).

5.3.2 Wave-Number Correlation

If we have repeated transverses on the same road, the estimates of the gravity disturbances from different traverses should be highly correlated at the same locations, while the systematic processing and instrument errors should be much less correlated. One way to correlate the repeated estimates is by transforming each into the frequency domain using the Fourier Transform. Then, a frequency component of the estimate is retained if they are correlated more than a certain threshold. The final estimate is obtained by taking the average of the retained components and transforming them back to the original domain, either time or space.

Suppose we have two traverses along the same road segment, and after wavelet de-noising the two gravity disturbance estimates are $\delta\hat{\vec{g}}_1^n(k)$ and $\delta\hat{\vec{g}}_2^n(k)$, $k = 1, 2, \ldots,$, respectively. The corresponding Fourier transforms are $G_1(l)$ and $G_2(l)$, where l is the wave number. The correlation coefficient is given by

$$\sigma_l = \frac{\mathrm{Re}(G_1(l))\mathrm{Re}(G_2(l)) + \mathrm{Im}(G_1(l))\mathrm{Im}(G_2(l))}{|G_1(l)||G_2(l)|} \tag{5.3.5}$$

The signal is wave-correlation filtered via the following equations:

$$\overline{G}_{1,2}(l) = \begin{cases} G_{1,2}(l) & \text{if } \sigma_l \geq tol \\ 0 & \text{if } \sigma_l < tol \end{cases} \tag{5.3.6}$$

where tol is a given tolerance, e.g., $tol = 0.5$; and

$$\delta\hat{\vec{g}}^n(k) = \frac{1}{2}F\left\{\overline{G}_1(l) + \overline{G}_2(l)\right\} \tag{5.3.7}$$

where F denotes the Fourier transform.

5.4 Control Data Interpolation

To evaluate the system accuracy compared with the external control data, it is necessary to interpolate the discrete control data onto the survey traverses. There

are many interpolation methods for scattered data in the literature, e.g., Franke (1982) compared 29 algorithms. Even more broad reviews were given by Franke (1987) and Hubeli and Gross (2000). However, it is very difficult to categorize and rank these interpolation methods under uniform criteria, because the most important categorization principles differentiate between discrete/continuous, linear/nonlinear and local/global basis function models (Mautz et. al., 2003).

Here, the Least Square Collocation and Multiquadrics methods are considered. The performances are compared with that of the Matlab subroutines, which apply Delaunay triangulation-based cubic spline fits.

5.4.1 Least Square Collocation (LSC)

Consider the linear system:

$$\underline{l} = \underline{L}T + \underline{n} \tag{5.4.1}$$

where $\underline{l}$ is the vector of observables, $\underline{L}$ is a linear operator, T is a scalar stationary and ergodic stochastic process with zero mean, $\underline{n}$ is the vector of observation errors with dispersion matrix $D_{\underline{n}}$, and T and $\underline{n}$ are uncorrelated. Then a linear estimator of T based on observed values $\underline{l}$ may be written as

$$\hat{T} = \underline{H}^T \underline{l} \tag{5.4.2}$$

We wish to find a minimum error variance estimate for T, i.e., $E\left\{(T-\hat{T})^2\right\}$=min. So we have:

$$E\left\{(T-\hat{T})^2\right\} = E\left\{(T-\underline{H}^T\underline{l})(T-\underline{H}^T\underline{l})^T\right\} \tag{5.4.3}$$

Under the ergodic and stationary assumption, the above equation can by written as:

$$\begin{array}{rl} & E\left\{TT^T - T\underline{l}^T\underline{H} - \underline{H}^T\underline{l}T + \underline{H}^T\underline{l}\underline{l}^T\underline{H}\right\} \\ = & C_{T,T} + C_{T,\underline{L}T}\underline{H} - \underline{H}^T C_{\underline{L}T,T} + \underline{H}^T C_{\underline{l},\underline{l}}\underline{H} \end{array} \tag{5.4.4}$$

where $C_{T,T}$ is the auto covariance function of T, $C_{T,\underline{L}T}$ is the covariance function between T and $\underline{L}T$, and $C_{\underline{l},\underline{l}}$ is the covariance function of $\underline{l}$. If we assume that T is not correlated with the measurement error $\underline{n}$, then

$$C_{\underline{l},\underline{l}} = C_{\underline{L}T+\underline{n},\underline{L}T+\underline{n}} = C_{\underline{L}T,\underline{L}T} + D_{\underline{n},\underline{n}} \tag{5.4.5}$$

Also

$$C_{\underline{l},T} = C_{\underline{L}T+\underline{n},T} = C_{\underline{L}T,T} \tag{5.4.6}$$

So we can write:

$$E\left\{(T-\hat{T})^2\right\} = C_{T,T} - C_{T,\underline{L}T}C_{\underline{l},\underline{l}}^{-1}C_{\underline{L}T,T} + (\underline{H}^T - C_{T,\underline{L}T}C_{\underline{l},\underline{l}}^{-1})C_{\underline{l},\underline{l}}(\underline{H}^T - C_{T,\underline{L}T}C_{\underline{l},\underline{l}}^{-1})^T \tag{5.4.7}$$

The only variance is H in the above equation. So it is clear that if we choose $\underline{H}^T = C_{T,\underline{L}T}C_{\underline{l},\underline{l}}^{-1}$, then the error variance reaches minimum in the above equation.

Therefore,

$$\hat{T} = C_{T,\underline{L}T}C_{\underline{l},\underline{l}}^{-1}\underline{l} \tag{5.4.8}$$

If T and $\underline{l}$ refer to the same kind of quantity, say, the gravity disturbance δg, and denoted by δg_1, and $\delta \underline{g}_2$ respectively, then we have

$$\delta\hat{g}_1 = C_{\delta\hat{g}_1,\delta\underline{\hat{g}}_2}(C_{\delta\underline{\hat{g}}_2,\delta\underline{\hat{g}}_2} + D_{\underline{n}})^{-1}\delta\underline{\hat{g}}_2 \tag{5.4.9}$$

and

$$E\left\{(\delta g_1 - \delta\hat{g}_1)^2\right\} = C_{\varepsilon,\varepsilon} = C_{\delta\hat{g}_1,\delta\hat{g}_1} - C_{\delta\hat{g}_1,\delta\underline{\hat{g}}_2}(C_{\delta\underline{\hat{g}}_2,\delta\underline{\hat{g}}_2} + D_{\underline{n}})^{-1}C_{\delta\hat{g}_1,\delta\underline{\hat{g}}_2}^T \tag{5.4.10}$$

Equation (5.4.9) shows that if we observed δg at some points, we can estimate δg at any point. In another words, LSC can be used for the purpose of interpolation. However, in practice, the performance is directly determined by the quality of the covariance models. In general, there are two categories of covariance models in the literature, i.e., the empirical models, and global or local analytic models. Among them, the empirical model is most useful for interpolation.

5.4.2 Multiquadrics

Another interpolation method selected here is the well known Multiquadrics (MQ), introduced by Hardy (1971). Their functional model reads

$$f(x,y) = \sum_{k=1}^{n} A_k\sqrt{r_k^2 + c^2} \tag{5.4.11}$$

where $r_k^2 = (x-x_k)^2 + (y-y_k)^2$ as the radial distance between the evaluation point (x,y) and a fixed center position (x_k,y_k), which could be the location of one of the observations. The coefficients, A_k, are the unknown parameters and c is a predefined

real constant. As pointed out by Mautz et.al. (2003), this parameter is not very sensitive to the data, and it is reasonable to be constant. However, in order to obtain satisfying results, c has to be optimized prior to the application.

A natural extension of Hardy's (1971) Multiquadrics into higher dimensioned space gives the following expression of the underlying function as shown in equation (5.4.12).

$$\sum_{j=1}^{n} \alpha_j \left[(x_j - x_i)^2 + (y_j - y_i)^2 + (z_j - z_i)^2 + c^2\right]^{\frac{1}{2}} = \delta g_i \quad i = 1, 2, \ldots, n \quad (5.4.12)$$

where δg_i is the gravity anomaly at point (x_i, y_i, z_i) . Let $X = [\alpha_1, \alpha_2, \ldots, \alpha_n]^T$, and $a_{ij} = [(x_j - x_i)^2 + (y_j - y_i)^2 + (z_j - z_i)^2 + c^2]^{1/2} \quad (i, j = 1, 2, \ldots, n)$. If we let $A := [a_{ij}]$, and $B = [\delta g_1, \delta g_2, \ldots, \delta g_n]^T$,the coefficient X may be obtained from equation (5.4.13):

$$X = (A^T A)^{-1} A^T B \quad (5.4.13)$$

Then one can evaluate the underlying function at any interested point by equation (5.4.12).

5.4.3 Computation evaluations and conclusions

To evaluate the performances of the above methods, computation tests are conducted in southwestern Montana area, as shown in Figure (5.2), which shows the distribution of control points near and along the survey routes. The small dots in the figure are the gravity data provided by the National Geospatial-Intelligence Agency (NGA). The circled crosses are chosen for the purposes of testing. Three interpolation methods, i.e., LSC, Multiquadrics (MQ), and the Matlab interpolation (Delaunay triangulation-based cubic spline fit), are used to interpolate the values at the testing points by using the neighboring control. The interpolated values are compared with the original gravity values provided by NGA. Table 5.1 lists the statistics of the interpolation errors for each method.

From Table 5.1, LSC show slightly better accuracy than multiquadrics interpolation. However, the covariance function for LSC (derived by Jekeli 2003 and rescaled to fit the variance of the gravity anomalies in the Montana area) is unstable with respect to the added noise variances most of the time when the control data are spatially dense. As a result, the estimated error variances, as shown in equation 5.4.10, are negative, which indicates that the estimation itself is unstable. Therefore, the listed standard deviations are not necessarily representative of the accuracy of the control data that are interpolated to the estimation points. The MQ method was

Segment	no. points	[mGal]	LSC	MQ	Matlab
I90	34	Mean	−0.086	1.2	6.6
		STD	4.2	4.7	12.
SR1	25	Mean	0.034	1.5	6.9
		STD	2.1	3.2	13.
SR43	42	Mean	0.034	0.53	3.9
		STD	2.6	2.7	6.0

Table 5.1: Statistics of interpolation errors of the selected methods

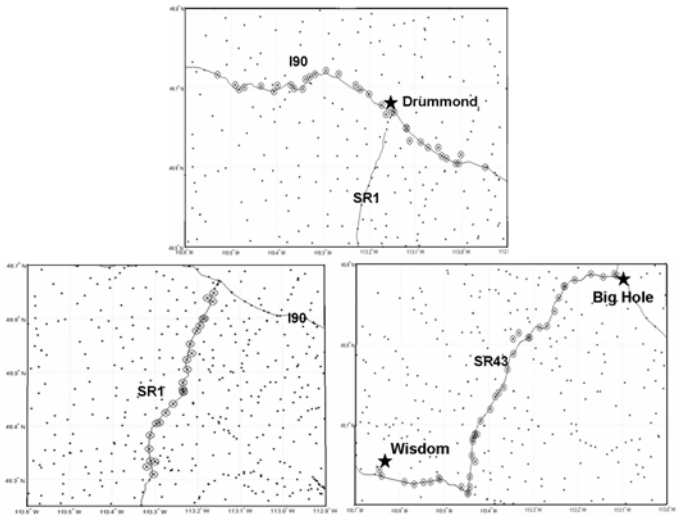

Figure 5.2: Control data and testing points in the survey area

found to be most stable and we can assume that this interpolated control has an accuracy of approximately 2-4 mGal.

The only advantage of Matlab subroutines is in the computation speed. However, considering computation time here is not very crucial, the MQ interpolation method is used to interpolate the control data onto the survey traverses for the purpose of external evaluation of the system accuracy in the following analysis.

CHAPTER 6

APPLICATIONS AND RESULTS

Moving base INS/GPS gravimetric system provides an efficient way to improve the resolution of the gravity field. Especially the airborne system has been extensively studied and successfully used for many years. From Greenland to Antarctica, many successful airborne gravimetric campaigns were conducted all over the world. However, due to the attenuation of the gravity field at high altitude, it is very challenging to detect short wavelength (<10km) gravity signals. But many applications in geology and geophysics require the knowledge of a local gravity field with a typical half wavelength resolution of 1km to 10km, or even higher resolution. Considering that the power of the gravity field (especially the short wavelength part) is greatest at the surface of the Earth and that lower vehicle speed implies higher resolution, a land vehicle based INS/GPS vector gravimetric prototype was developed at the Ohio State University (OSU).

Although more high frequency gravity signals reside in the acceleration measurements in the terrestrial system than in the airborne system, the dynamics of the slower moving terrestrial system creates more turbulence and high frequency accelerations. As a result, the observables of these two systems have different characteristics. Furthermore, the terrestrial moving base system may experience a more complicated observation environment than the airborne system. The survey routes may have turns and ups and downs unlike the flight trajectories, which can maintain at a relatively stable observation situation. This will severely degrade the quality of the observables, especially the GPS related ones, which may have data gaps due to signal blocking in valleys, forest, or tunnels.

So it is necessary to introduce new techniques and adjust the airborne algorithms for the terrestrial moving base INS/GPS gravimetric system in order to overcome the above difficulties. This chapter applies the techniques described in the previous chapters to a terrestrial moving base INS/GPS gravimetric survey campaign conducted by NGA and OSU on 2005 at southwestern Montana. The first section describes the system setup and survey campaign. The second section contains the data processing

details of the traverses on State Route 43 (SR43). The data processing procedures and results on the other survey routes are contained in section 6.3.

6.1 System Setup and Survey Campaign

The survey vehicle is a GMC Suburban modified for a GIS-type survey (2 GPS antennas mounted on the roof, camera mounts available, and the interior is outfitted with a secure instrument platform and battery-driven power supplies). This vehicle, known as the GPSVan, belongs to OSU's Center for Mapping. Figure 6.1 shows the GPSVan and the interior suite of IMU and GPS instruments, looking aft. The SINS is the high-accuracy Honeywell H764G inertial navigation system and is configured to provide raw accelerometer and gyro data at a rate of 256 Hz. For redundancy, three brands of geodetic quality GPS receivers were used in the GPSVan: Trimble5700, Topcon, and NovAtel. In April and June of 2005, NGA and OSU performed the data collection in southwestern Montana by using this system. The survey area map is shown in Figure 6.2. The earlier test in April was mainly focused on the Interstate Highway 90 (I90) from Butte to Missoula, MT. The data sets collected in June are more extensive over some mountain passes and through major valleys. In all cases, the vehicle essentially remained on well-paved roads.

Figure 6.1: System exterior and interior look

In addition to the nearby CORS station (MSOL) at Missoula, several temporary GPS base stations were set up around the survey routes as shown in Figure 6.2 to obtain the DGPS solution. The coordinates of these temporary base stations are obtained by network adjustments using TGO^{TM} (Trimble Geomatics Office). The values are shown in Tables 6.1-6.3.

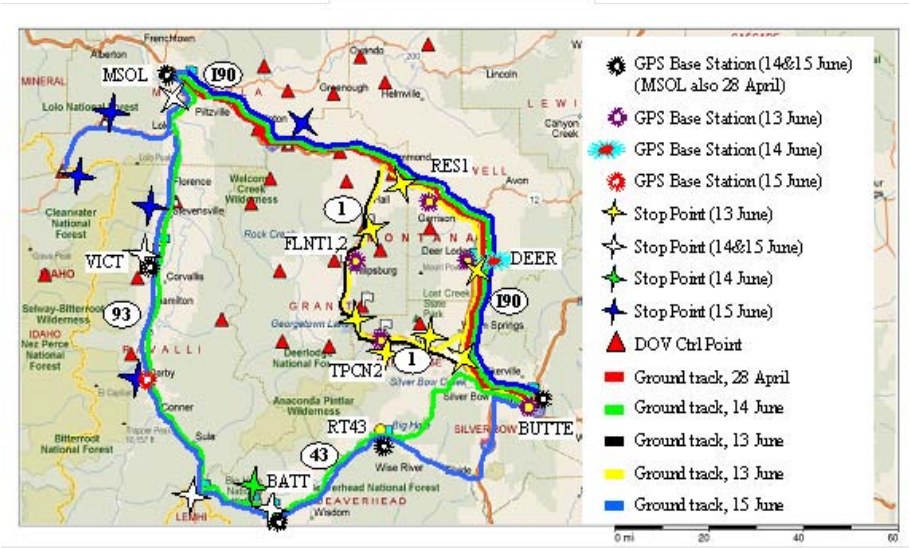

Figure 6.2: Map of the survey area

Station Name	Lat/Lon/Ht(WGS84)		
BUTTE	45^o 57' 59.96768" N	112^o 30' 48.30209" W	1663.225m
FLNT1	46^o 23' 54.01455" N	113^o 18' 27.06106" W	1518.158m
FLNT2	46^o 23' 54.00591" N	113^o 18' 27.06384" W	1518.018m
TPCN2	46^o 10' 07.25022" N	113^o 09' 30.92281" W	1835.858m
DEER	46^o 24' 20.30241" N	112^o 44' 07.90459" W	1363.709m
RES1	46^o 35' 07.40556" N	112^o 54' 25.51021" W	1267.839m

Table 6.1: June 13 205 temporary base station coordinates.

Station Name	Lat/Lon/Ht(WGS84)		
TPCN2	45^o 57' 59.96661" N	112^o 30' 48.30269" W	1665.735m
BATT	45^o 38' 26.75867" N	113^o 38' 37.00976" W	1913.502m
DEER	46^o 24' 20.30278" N	112^o 44' 07.90449" W	1363.614m
RT43	45^o 53' 01.14267" N	113^o 07' 40.28175" W	1746.186m
VICT	46^o 25' 02.25527" N	114^o 08' 49.02570" W	1021.924m

Table 6.2: June 14 205 temporary base station coordinates.

Station Name	Lat/Lon/Ht(WGS84)		
TPCN2	45^o 57' 59.96635" N	112^o 30' 48.30321" W	1665.635m
BATT	45^o 38' 26.63928" N	113^o 38' 36.96147" W	1913.415m
DARB	46^o 01' 39.66985" N	114^o 10' 36.14283" W	1169.582m
R43	45^o 53' 04.81068" N	113^o 09' 12.79905" W	1752.202m
VICT	46^o 25' 02.25119" N	114^o 08' 49.03433" W	1021.749m

Table 6.3: June 15 205 temporary base station coordinates.

From Figure 6.2, we can see that there are two repeated traverses on State Routes 43, 93, and 1 (SR43, SR93, SR1), and there are three repeated traverses on I90. Not all the collected data were used in the final analysis due to a number of adverse conditions (as well as blunders) encountered during the survey. Primarily, GPS data and corresponding positioning solutions were not always adequate in the precision needed to compute the kinematic accelerations; many of the temporary GPS base stations were found to be less useful than originally anticipated, and the accuracy of the INS data depended to some extent on the dynamics of the vehicle. However, a large sample of data could be analyzed to assess the capability of the INS/GPS gravimetric capabilities for the two types of roads (interstate highways and well paved and graded state routes). The segments of successful estimation on SR1, SR 43, and I90 are shown by the thicker lines in Figure 6.3.

The available gravity control data are shown by the (green) dots in Figure 6.3. These data are measured by gravimeters. They are the magnitudes of the down gravity component. The corresponding gravity disturbances at these points are obtained by subtracting the normal gravity from the observed values. Also the DOV (deflection of vertical) data obtained by NGA with astrometric instruments (astrolabe and theodolite) along SR1 and SR43 are plotted by the thick black lines in this figure. In addition, the National Geodetic Survey (NGS) produced a $1' \times 1'$ DOV grid derived from a national geoid model (GEOID99; Smith and Roman, 2001). This DEFLEC99 model was computed by NGS using a two-step procedure. First, slopes of GEOID99 were determined using bicubic splines; and, subsequently, these were corrected for the curvature of the plumb line based on simple Bouguer gravity anomalies to yield DOV's at the Earth's surface. It allows the user to determine the deflection components at any defined set of coordinates in the Conterminous United States. Table 6.4 gives the statistics of the differences (shown in Figure 6.4) between the interpolated DEFLEC99 values and the presumably more accurate astrogeodetic DOVs at points along SR1 and SR43. All deflection values were converted into equivalent horizontal

gravity components. We conclude that the DEFLEC99 control is accurate to about 4.6 mGal (RMS), or about 1 arcsec (RMS). Table 6.5 summarizes the estimated accuracies of all control data.

Figure 6.3: The successful estimates and the control data

These control data and the repeated estimates enable assessing both system accuracy and internal repeatability. For instance, in the horizontal components, the estimates are compared with the DEFLEC99 model generated values. The down component estimates are compared with the control data interpolated to the estimation points. The multiquadrics method (Section 5.4.2) is used to interpolate the available gravity data onto the traverses. The repeated estimates are compared in the along track distance domain; see the following section for details.

6.2 Data Processing on SR43

There are two repeated traverses on SR43 as shown in Figure 6.2. Traverse 1 was run on June 14 2005 from northeast to southwest and Traverse 2 on June 15 2005, but in the opposite direction. From Wisdom to Big Hole (Figure 6.2), these two traverses generate two independent gravity disturbance estimates on SR43 with a total along-track distance about 60km. The average speed is about 22m/s. Considering the 1Hz GPS sampling rate, the raw gravity disturbance observation has a 22-meter

(mGal)	mean	St.dev.	RMS	abs max	abs min
North (SR1)	4.15	3.27	5.29	12.48	0.54
East (SR1)	1.67	4.12	4.44	13.45	0.10
North (SR43)	2.07	3.46	4.03	10.48	0.22
East (SR43)	0.37	4.78	4.80	11.39	0.11
North (overall)	2.93	3.52	4.58	12.48	0.22
East (overall)	0.91	4.55	4.64	13.45	0.10

Table 6.4: Statistics of differences between interpolated DEFLEC99 DOV and NGA DOV along SR1 and SR43.

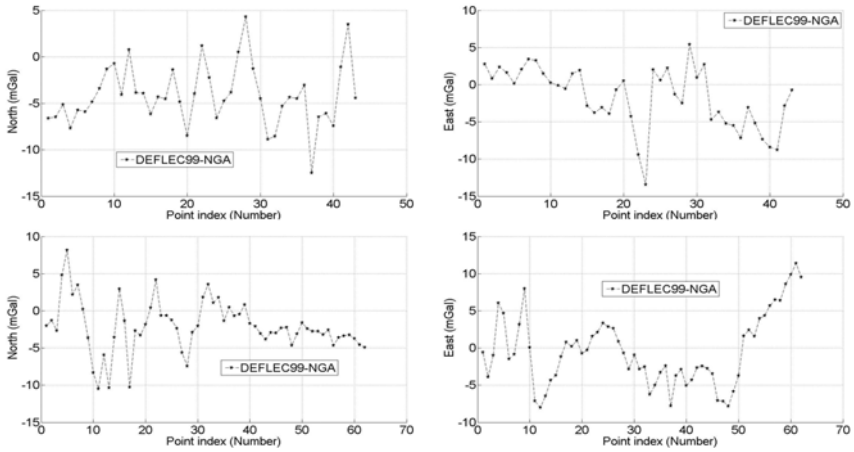

Figure 6.4: The DOV differences

Data Type	number; resolution	accuracy
Gravity	6496; irregular	1 mGal (est) (2-4mGal, interpolated value)
astro-geodetic DOV (SR1)	43; 1.6 km	0.5 arcsec (est)
astro-geodetic DOV (SR43)	62; 1.6 km	0.5 arcsec (est)
DEFLEC99 DOV	Whole area; $1' \times 1'$	1 arcsec[1]

[1] estimated from RMS comparison to astrogeodetic DOVs along SR1 and SR43 (Table 6.4) .

Table 6.5: Summary of control data.

	$X(m)$	$Y(m)$	Z(m)	VX(m/s)	VY(m/s)	VZ(m/s)
Mean	-0.402	0.641	-0.009	-0.107	0.056	0.007
STD	2.385	1.097	0.533	0.219	0.124	0.047

Table 6.6: statistics of the TAEKF positioning errors.

resolution. However, the 180-second B-spline smoother degrades the final resolution to about 2.2km. This section describes the details of the data processing to estimate the gravity disturbance on SR43.

6.2.1 Traverse1

Since it is important that the positioning solution is precise and continuous in the moving base gravimetric system. The TAEKF (see section 3.4) is employed first to fix the gaps in the DGPS solution. To test the algorithm, we generate a 50-second artificial gap in the DGPS solutions of position and velocity from 1350 seconds to 1440 seconds of the SR43 segment. The filter is run in both forward and backward directions. Then the data gap is fixed by optimally combining the forward direction results and the backward direction results. Figure 6.5 shows the integration results and the originally removed GPS solution (indicated by the red lines), which serves as control data. The differences, estimated minus the original position and velocity values, are shown in Figure 6.6. The statistics of the differences are shown in Table 6.6.

We see that by using the TAEKF the position gap can be fixed with accuracy at the 1-2 meter level, and the velocity gap can be fixed at the accuracy level of tens of cm. It is noted that in general the accuracy in the z direction is much better than in the other two directions, i.e., x and y axes.

In Chapter 3, we know that the TAEKF also can provide the long wavelength IMU errors. So the entire data set of this traverse is processed by the filter. The estimated IMU errors are shown in Figures 6.7-6.10, and used to calibrate the dynamic accelerations by using equation (4.1.2). The calibrated IMU accelerations are shown in Figures 6.11-6.13. Even though this calibration does not appear to improve the accuracy of the IMU accelerations significantly, it may still be worth from a theoretical standpoint to attempt it in the preliminary data processing stage.

To obtain an estimate of the gravity disturbance, we also need to compute the GPS acceleration. As described in Chapter 4, two methods are used to compute the GPS acceleration. First, in the position method, the rover GPS data from a

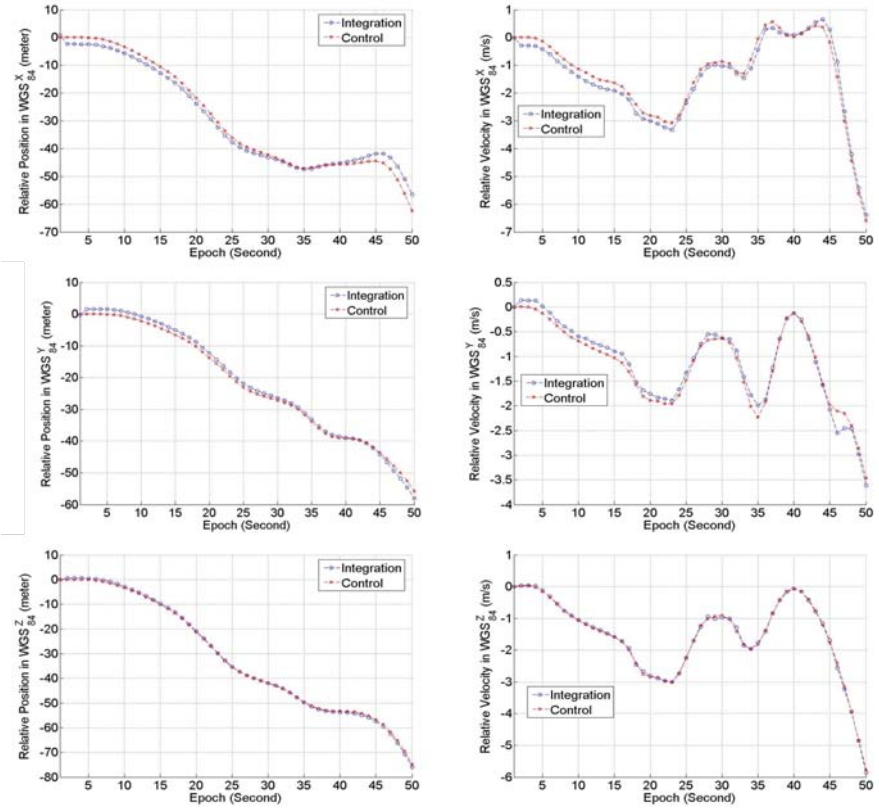

Figure 6.5: TAEKF positioning solutions

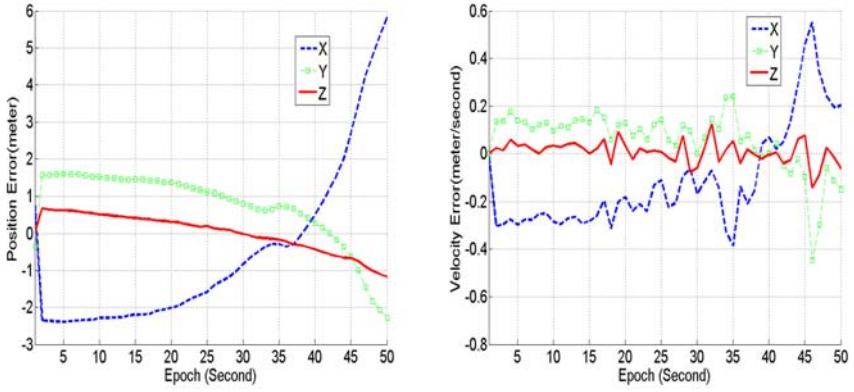

Figure 6.6: TAEKF integration errors

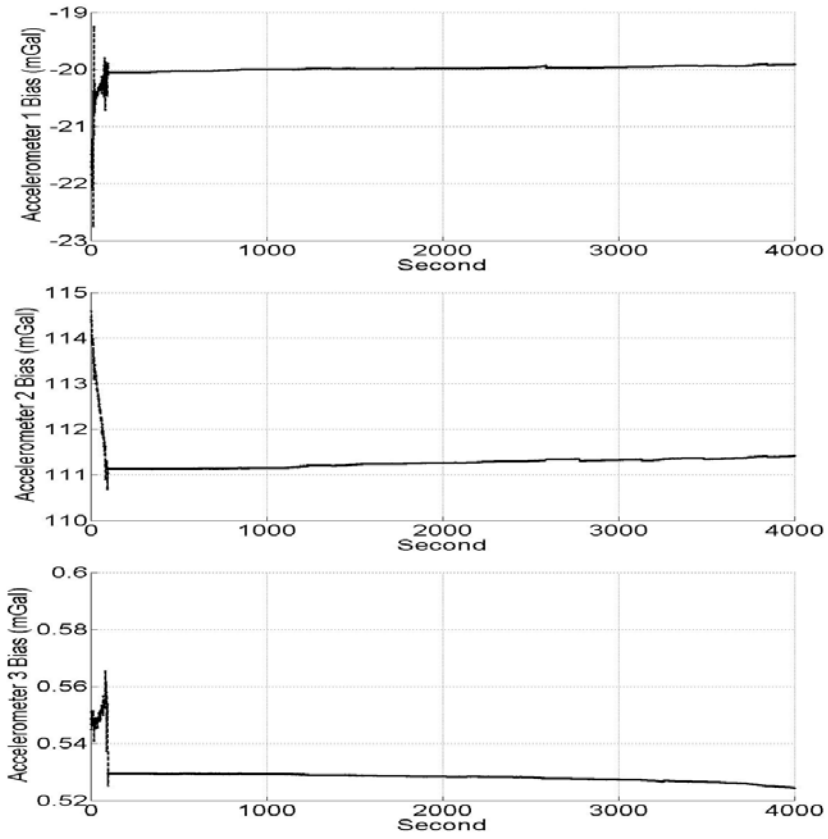

Figure 6.7: Accelerometer Bias estimated by the TAEKF

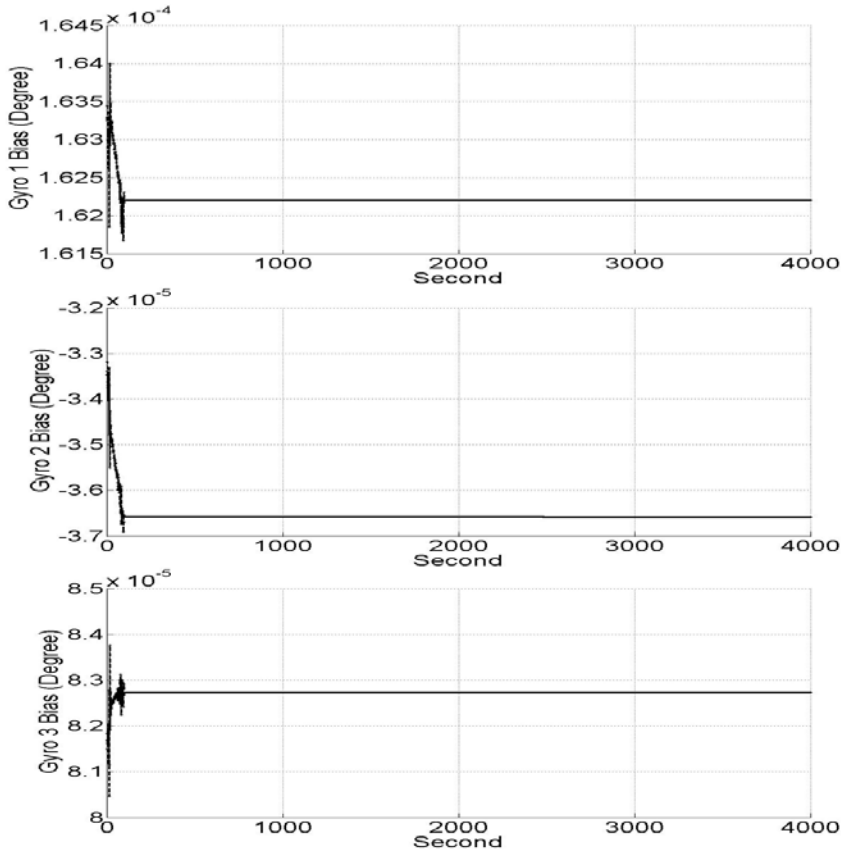

Figure 6.8: Gyro Bias estimated by the TAEKF

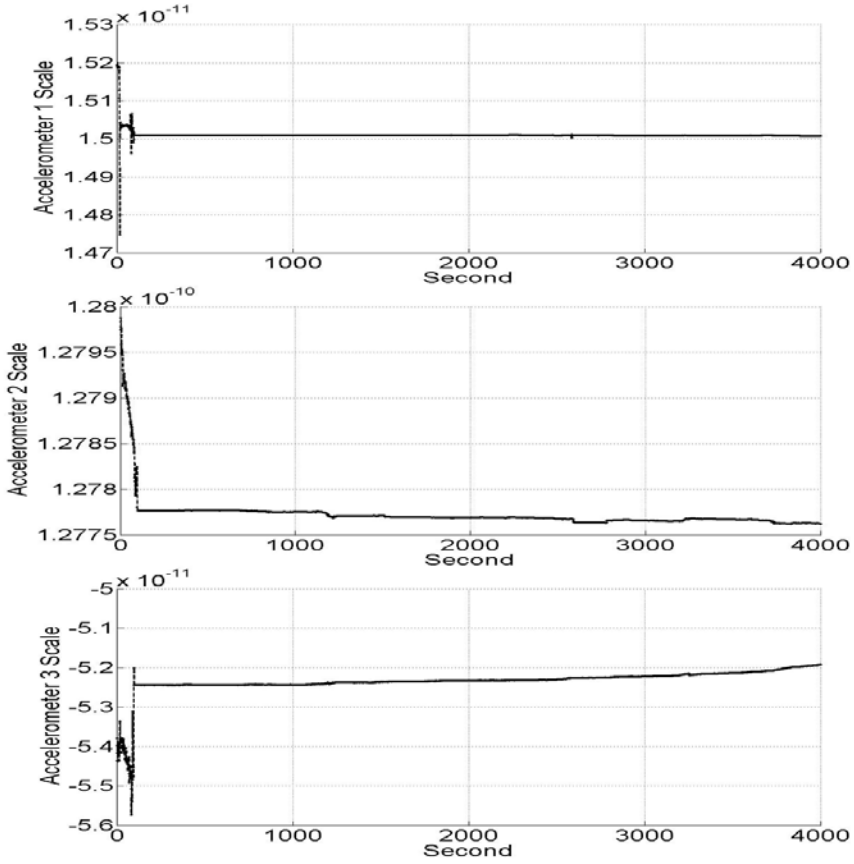

Figure 6.9: Accelerometer Scale estimated by the TAEKF

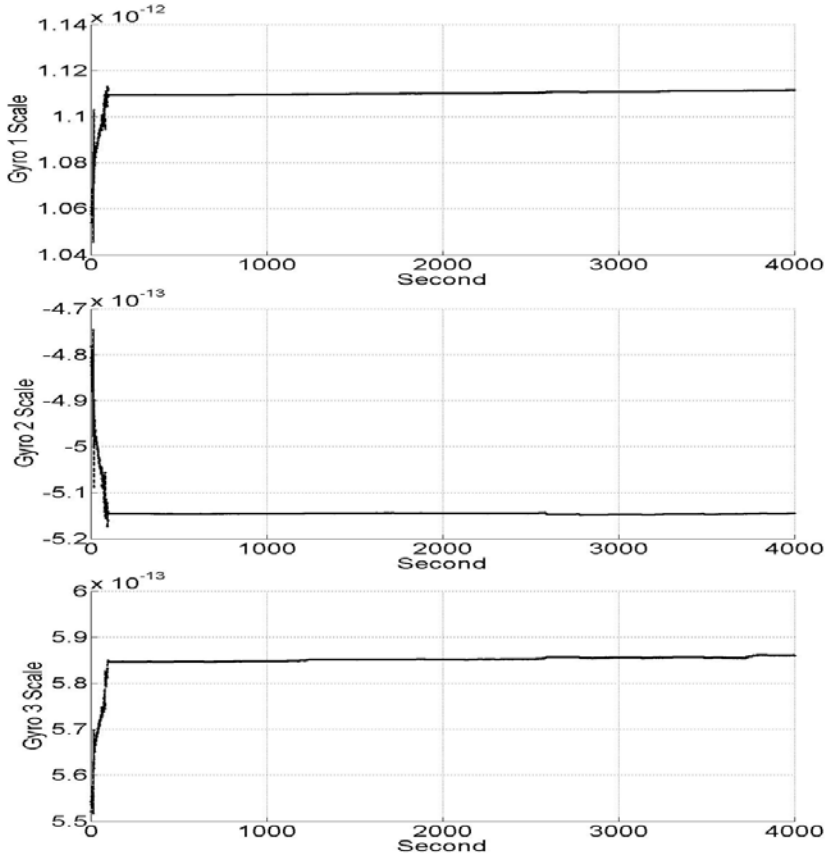

Figure 6.10: Gyro Scale estimated by the TAEKF

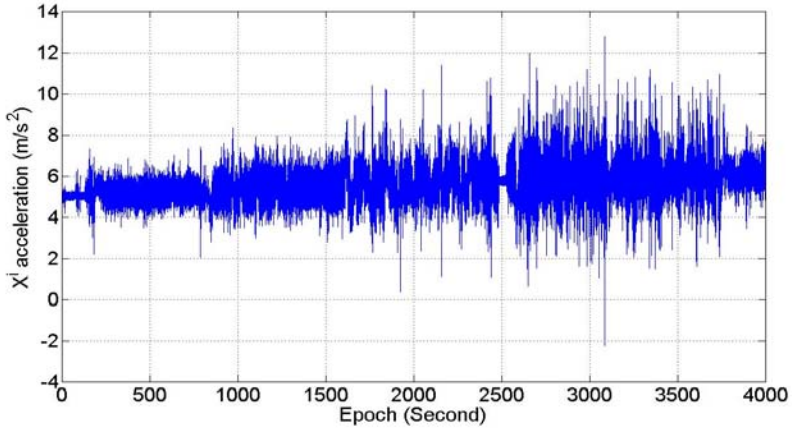

Figure 6.11: IMU acceleration in the x component of the inertial frame

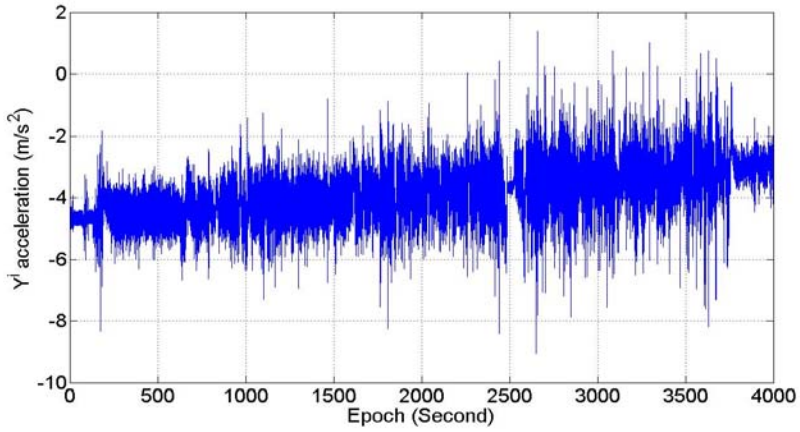

Figure 6.12: IMU acceleration in the y component of the inertial frame

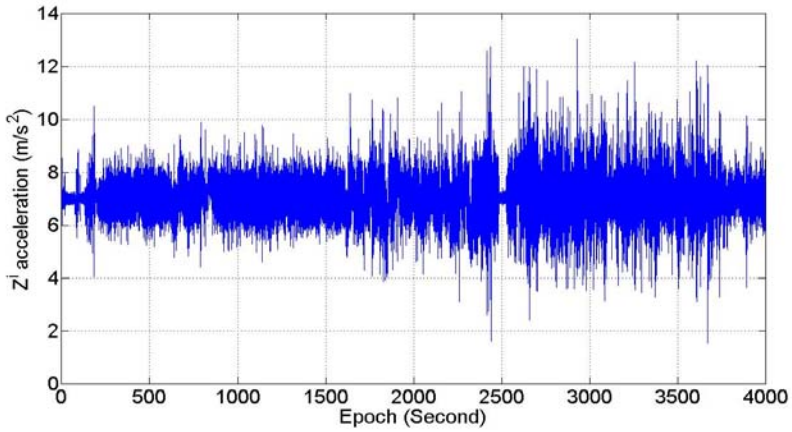

Figure 6.13: IMU acceleration in the z component of the inertial frame

Trimble receiver and the base station data from a Topcon receiver are used to build the DD observables, which are then processed by the ApplanixTM software to obtain the positioning solutions. To yield better results, the IGS precise orbits are used instead of using the broadcast orbits. Then the acceleration is obtained by taking two consecutive derivatives of the positioning solution. There are several ways to implement the derivatives numerically (see e.g. Bruton et. al., 1999). Based on our studies, we choose the B-spline method to obtain the derivatives. First, a B-spline function is fitted to the data under the principle of least sum of squares. Then the derivatives are obtained from the analytical representation of the fitted function. Notice, before taking the derivatives, the positioning solution should be transformed from the ECEF frame into the defined inertial frame, which is usually an earth-centered, no-rotation, Cartesian frame, i.e., $x^i = C_e^i x^e$. Second, the phase method is employed to evaluate the GPS acceleration independently. As we have seen in Chapter 4, the cycle slips should be correctly fixed so that we can take derivatives of the phase observables. And the final solution is obtained via the wave number correlation method, which combines the position derived acceleration and the phase derived acceleration in the frequency domain. The acceleration results are shown in Figures 6.16-6.18. From Chapter 4, we also know that after fixing the cycle slips, the Triple Difference (TD) solution is easily obtained. Figure 6.14 shows the differences between the TD solution and the Applanix^{TM} solution. At every epoch, the position distance between these two solutions is plotted in Figure 6.15, which shows meter level differences.

The accelerations in Figures 6.16-6.18 are highly correlated, implying that there are no programming or computation errors in both methods. However, due to this high correlation, the filtered acceleration after using wave-number correlation method does not change too much in the high frequency components (Figures 6.16-6.18). Only marginal improvements are noticed in the gravity diturbance estimates. The IMU accelerations in Figures 6.11-6.13 also have strong high frequency components (noise) which clearly are not due to gravity disturbance variantions. As a result, a B-spline smoother is used to reduce these noises in both the GPS and IMU accelerations. Numerical tests show that a window size of 180-second is a good choice of the smoother (see Jekeli and Li 2006 for details). Previous studies conducted by Kwon (2000) showed that a window size of 60-second or 90-second is appropriate for the airborne data. However, the relatively low speed of the GPSVan introduces more effects of atmospheric disturbances (See Appendix C for more details, also agrees with Hannah 2001). Moreover, the frequently changing heading direction and the ups and downs also bring in more high frequency accelerations (In the airborne scenario, we noticed large oscillations in the turns). Thus, we have to increase the window size in order

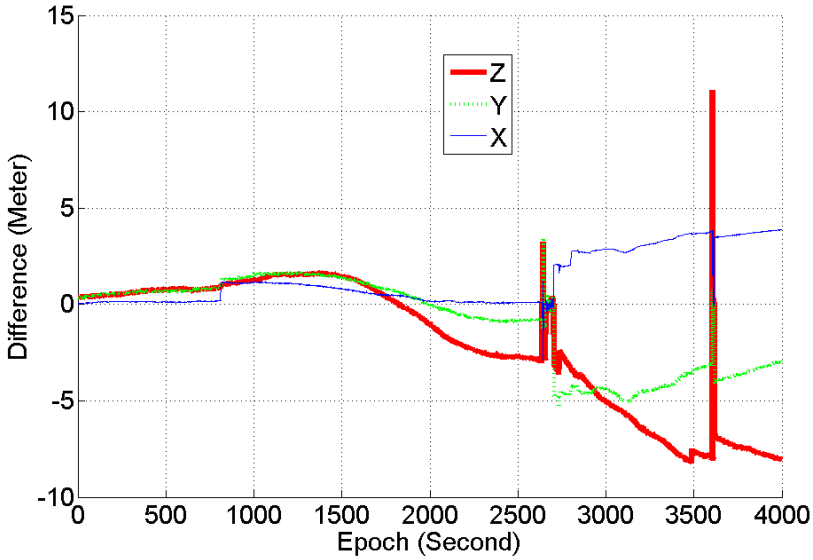

Figure 6.14: TD and Applanix^{TM} solution differences

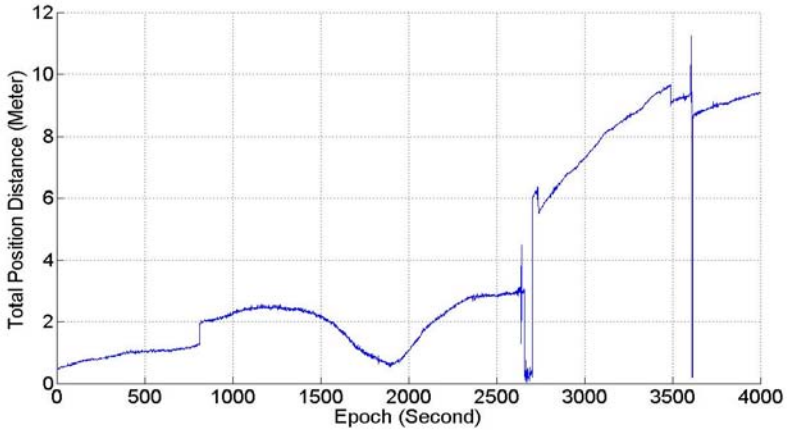

Figure 6.15: TD and Applanix^{TM} position distances

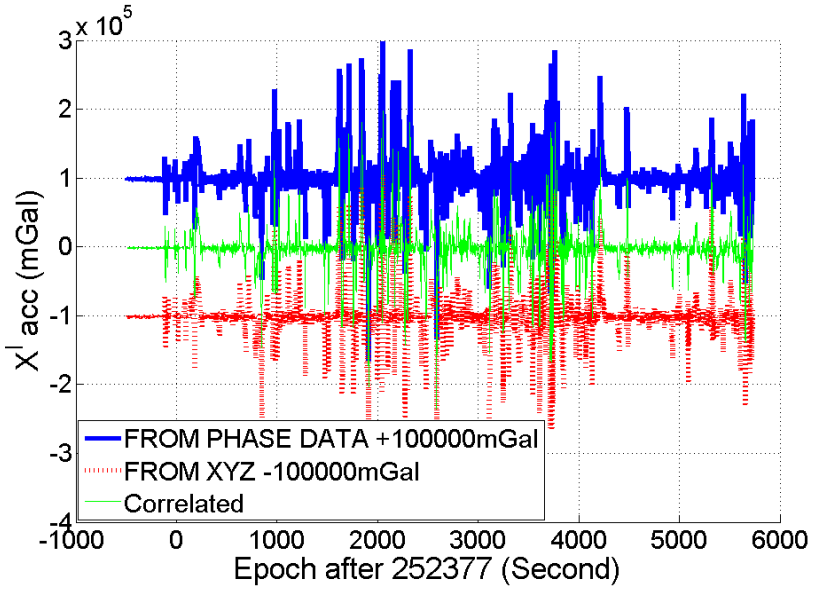

Figure 6.16: GPS acceleration in the x component of the inertial frame

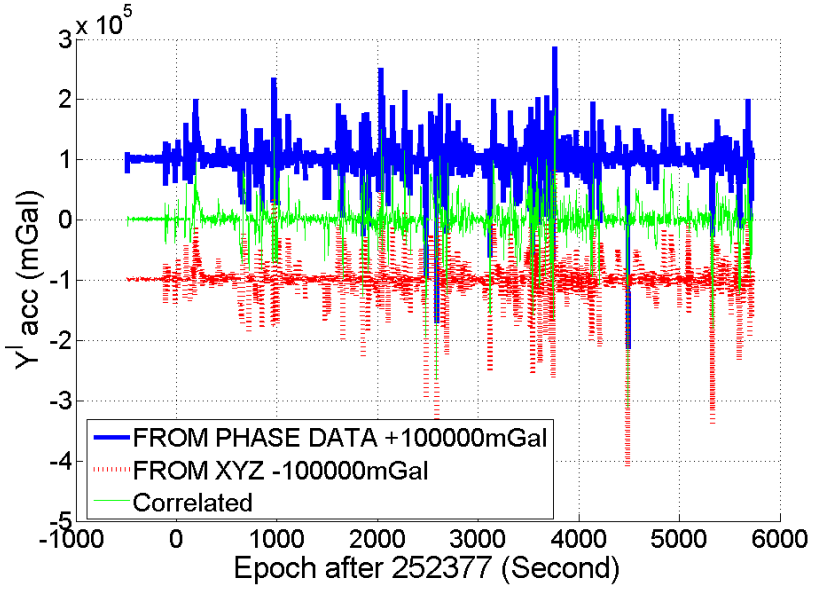

Figure 6.17: GPS acceleration in the y component of the inertial frame

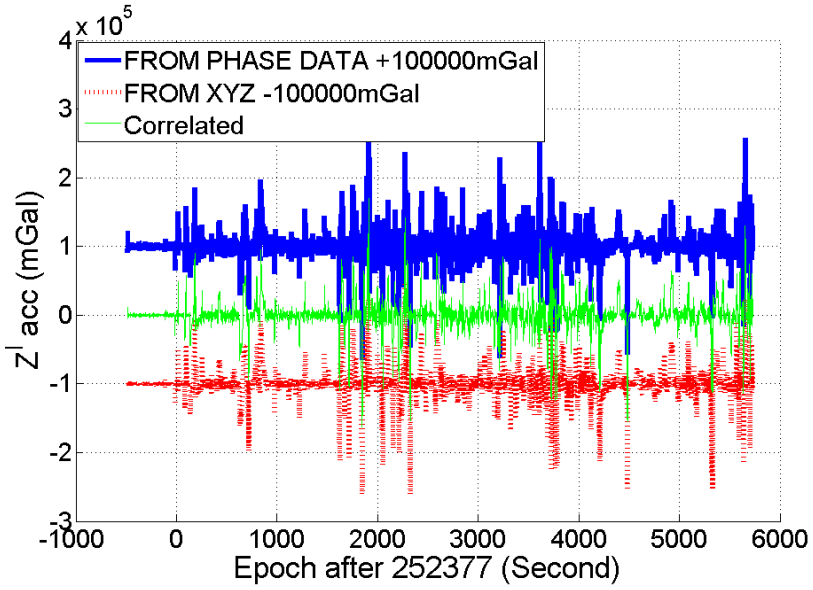

Figure 6.18: GPS acceleration in the z component of the inertial frame

to yield better results in the terrestrial system, even though this will decrease the resolution of the final estimates.

The Kalman system (equations 5.23-5.25) described in Section 5.2 is applied to these smoothed accelerations to get the first estimates of the gravity disturbance. The results are shown in Figure 6.19 for two sets of smoothed accelerations. The thick(blue) lines are the gravity disturbance estimates based on the calibrated IMU acceleration and the wave number correlated GPS accelerations. The dashed(red) lines are based on the un-calibrated IMU acceleration and the position-derived GPS acceleration. The horizontal control data are obtained from the DEFLEC99 model. The vertical control data are obtained by the multiquadrics interpolation method described in Chapter 5. The variations of the differences are described by the standard deviations. From these statistics we can see that the improved GPS and IMU accelerations have a positive effect in the gravity disturbance estimates. The improvement is mainly due to the improvements in the GPS accelerations.

6.2.2 Traverse2

We follow the same procedure as described in the above section to process the data along traverse 2 of the SR43 segment. The TAEKF results are given in Figures

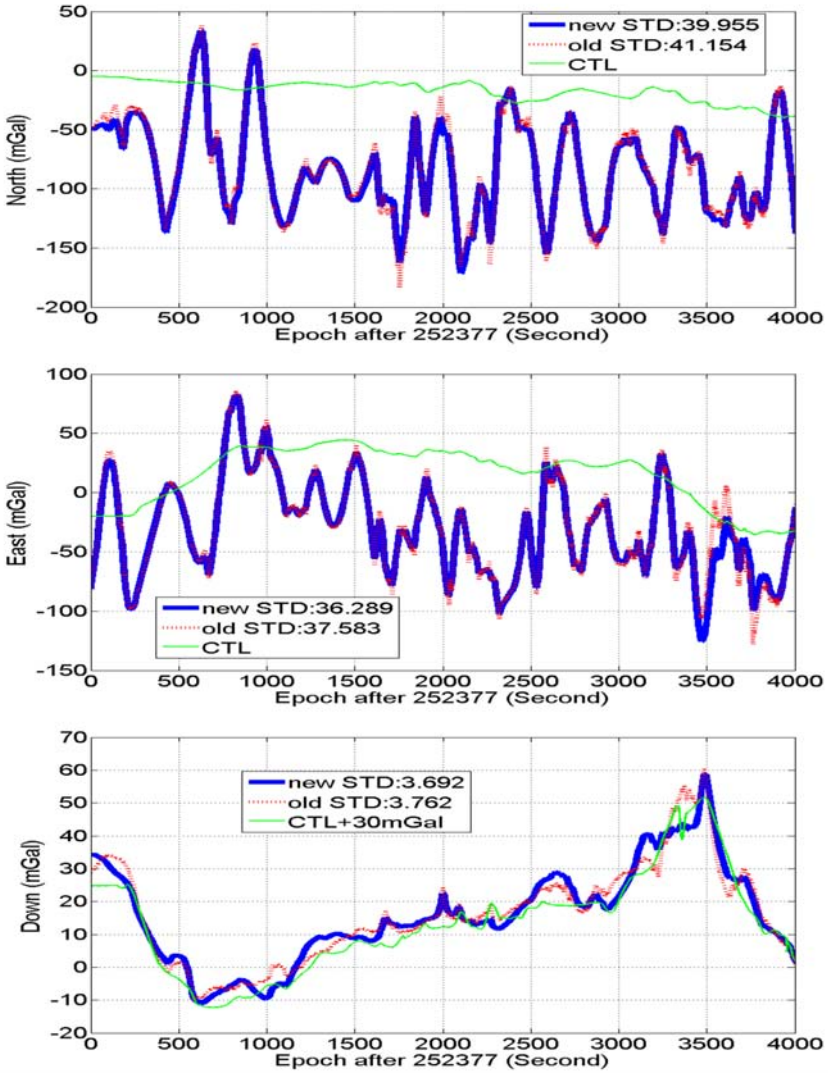

Figure 6.19: Gravity disturbance estimate on Traverse 1 SR43

3.11-3.14 in Section 3.5, and the GPS acceleration results are shown in Figures 4.14-4.16 in section 4.8.2. After smoothing and Kalman filtering, the estimated gravity disturbances are shown in Figure 6.20.

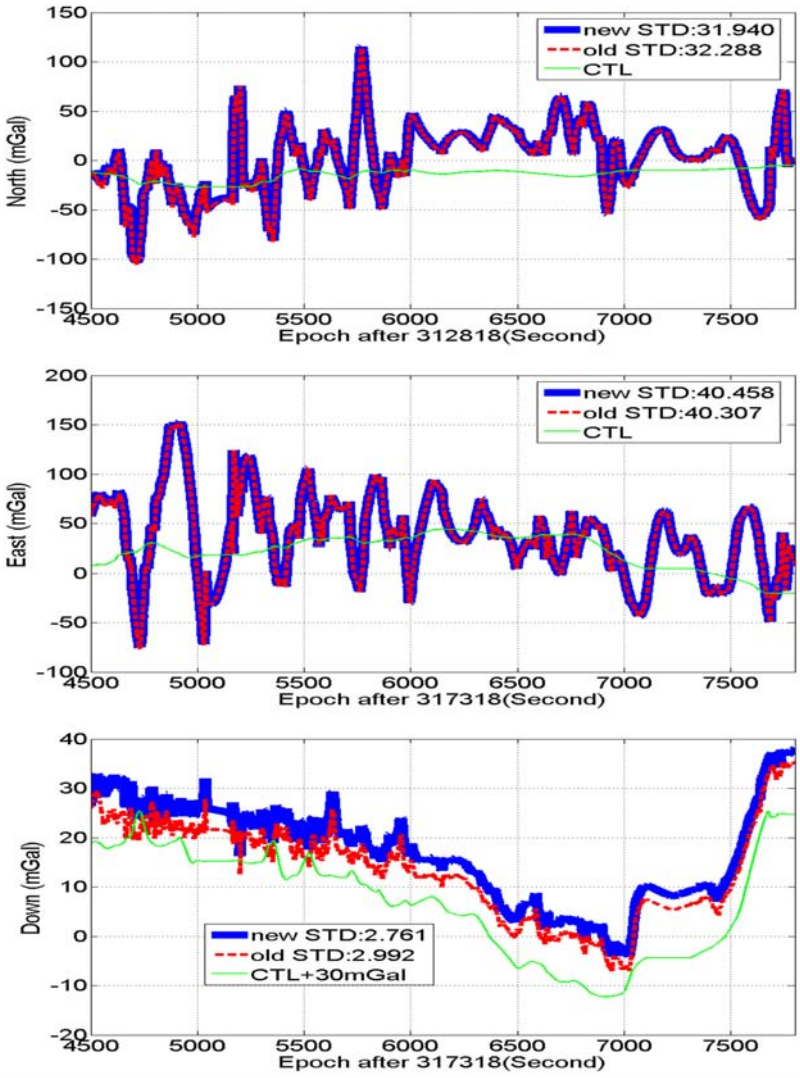

Figure 6.20: Gravity disturbance estimate on Traverse 2 SR43

Again, the dashed(red) lines are based on the un-calibrated IMU acceleration and the position-derived GPS acceleration. The thick(blue) ones are based on the calibrated IMU acceleration and the correlated GPS acceleration. From the statistics,

both the IMU calibration and the GPS acceleration correlation procedure have a positive effect on determining the gravity disturbances. As with traverse 1, improving the GPS acceleration is more effective than calibrating IMU acceleration in terms of improving the precision of the estimates. In the TAEKF, it is very challenging to push the acceleration bias and scale effects down to the mGal accuracy level because of the high frequency components in the observables. (Note, in order to preserve the vehicle's dynamics, we can not smooth the observables of the TAEKF filter with too large window size, e.g., 180 seconds). As a result, there are still bias and scale error effects in the gravity disturbance estimates, as shown in Figures 6.20.

6.2.3 Wavelet De-noising and Wave Number correlation

In the above two sections, we have obtained gravity disturbance estimates for the two traverses on SR43. In other words, we have duplicated estimates along the same route. Although they are not exactly at the same points, we can benefit from these independent estimations. For instance, we can determine the system repeatability, and obtain better results by performing a correlation analysis. To do this, we have to reregister these two estimates so that they refer to the same location. One way to do this is to transform the estimates from the time domain into the space domain and use the along track distance as index to rearrange the gravity disturbance estimates. First, we choose the starting point of traverse 2 as the origin of the along-track distance. This point is close to Big Hole in Figure 6.2. Then for traverse 2, the accumulated 3D distance is the along-track distance. For traverse 1, the accumulated 3D distance is computed in reverse in the time domain because traverse 1 is in the opposite direction of traverse 2. It is very important to notice that some parts of the data both in traverse 1 and traverse 2 are off-road, i.e., the van sometimes was driven off the main road. These points in both traverses should be deleted in order to obtain the correct "along-track" distances on SR43; see Jekeli and Li (2006) for details. Then, a spline fitting method is used to interpolate the gravity disturbances onto exactly the same position in terms of along-track distances. The resulting repeated estimates on SR43 are shown in Figure 6.21. The statistics of the differences are shown in Table 6.7. The statistics in Table 6.7 are different from the counterparts in Figures 6.19-6.20 due to the omission of the off-road points. After rearranging the data, the gravity disturbance estimates on these two traverses show high correlation, especially in the down component. The horizontal components appear to be subject to an unknown scale effect. The wavelet de-noising (Hybrid SureShrink) and wave number correlation (tol=0.5) methods (see Section 5.3 for more details) are used to further isolate the gravity disturbance estimates from the observation errors, which

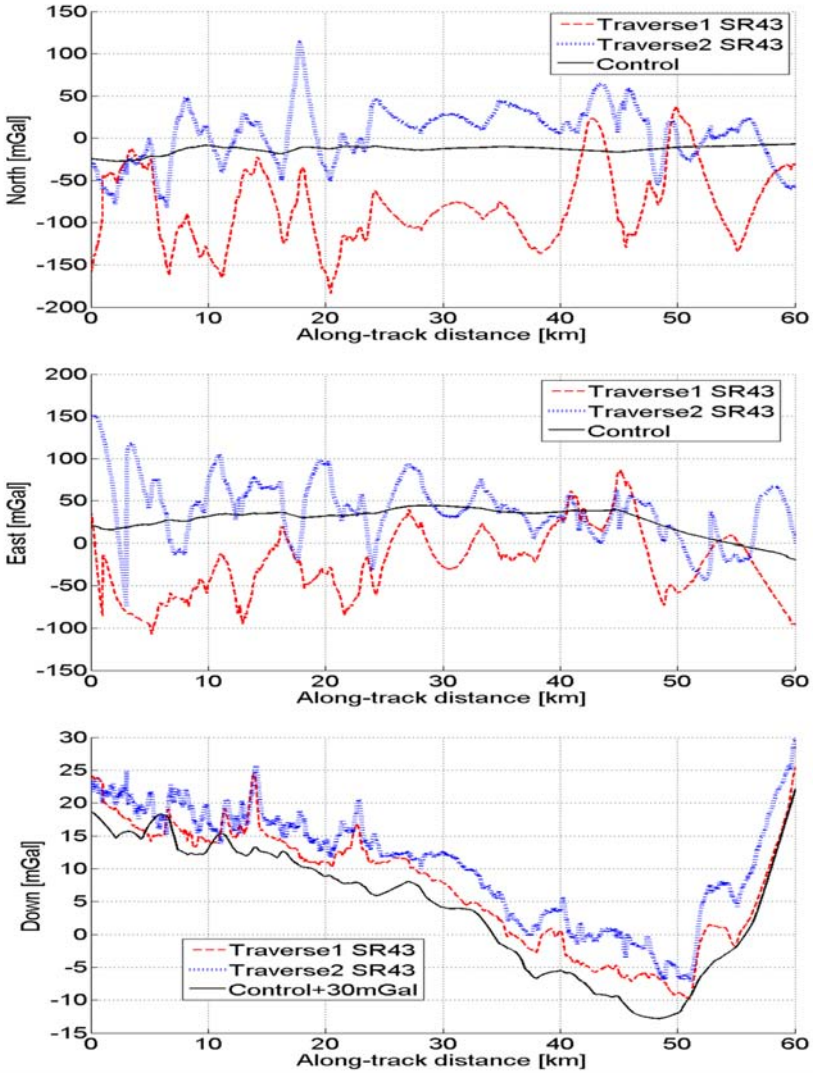

Figure 6.21: Gravity disturbance estimates on SR43 in space domain

mGal	North		East		Down	
	Mean	st.dev.	Mean	st.dev.	Mean	st.dev.
Traverse 1- Traverse 2	-83.55	**55.10**	-61.40	**54.76**	-3.42	**2.44**
Traverse 1- Control	-66.00	**45.94**	-49.96	**37.03**	33.26	**2.51**
Traverse 2- Control	17.55	**31.95**	11.44	**36.01**	36.68	**2.61**

Table 6.7: Statistics of the differences of the estimates and the control data on SR43.

mGal	North		East		Down	
	Mean	st.dev.	Mean	st.dev.	Mean	st.dev.
Traverse 1- Traverse 2	-83.50	**54.30**	-61.37	**51.80**	-3.43	**2.10**
Traverse 1- Control	-66.05	**44.89**	-49.98	**35.95**	33.26	**2.39**
Traverse 2- Control	17.45	**30.36**	11.38	**32.31**	36.68	**2.39**
Filtered- Control	13.05	**17.40**	-25.80	**24.15**	34.97	**2.09**

Table 6.8: Statistics of the differences of the estimates and the control data on SR43, after wavelet de-noising and wave number correlation.

are the last two terms in equation (5.2.7). The results are shown in Figure 6.22. The statistics of the differences are shown in Table 6.8.

Considering that we have interpolated control data on the traverses, the remaining bias and trend in Figure 6.22 are removed by using the end-matching method developed by Serpas (2003, pp 64.), which fits the estimates to the control values at the beginning and end points to solve the bias and trend in the estimates. After removing these estimated errors, the refined gravity disturbance estimates are shown in Figure 6.23.

From Figure 6.23, we can see that the down component has 2-3mGal precision and system repeatability, while the horizontal estimates are apparently contaminated by some systematic errors, such as an IMU scale error. The reason is mainly due to the special dynamics of the vehicle, which experiences relatively more heading angle changes than the airplane, as shown in Figure 6.24. These frequently changing heading angles make it very difficult for the IMU to accurately measure some components of the rotation rate. As a result, the sytem can not precisely decompose the horizontal gravity disturbance into North and East components. Comparing Table 6.7 and Table 6.8, we notice that the wave-number correlation and wavelet de-noising improve the precision by only a few tenths of mGal in the standard deviations. This may tell us that the remaining random observation errors in the Kalman residuals as shown in equation (5.2.7) are not very significant. However, the systematic IMU errors cause large oscillations in the horizontal components, which prohibit horizontal component estimates being as precise as the down component estimates. This problem will be solved in section 6.3 by using the control data.

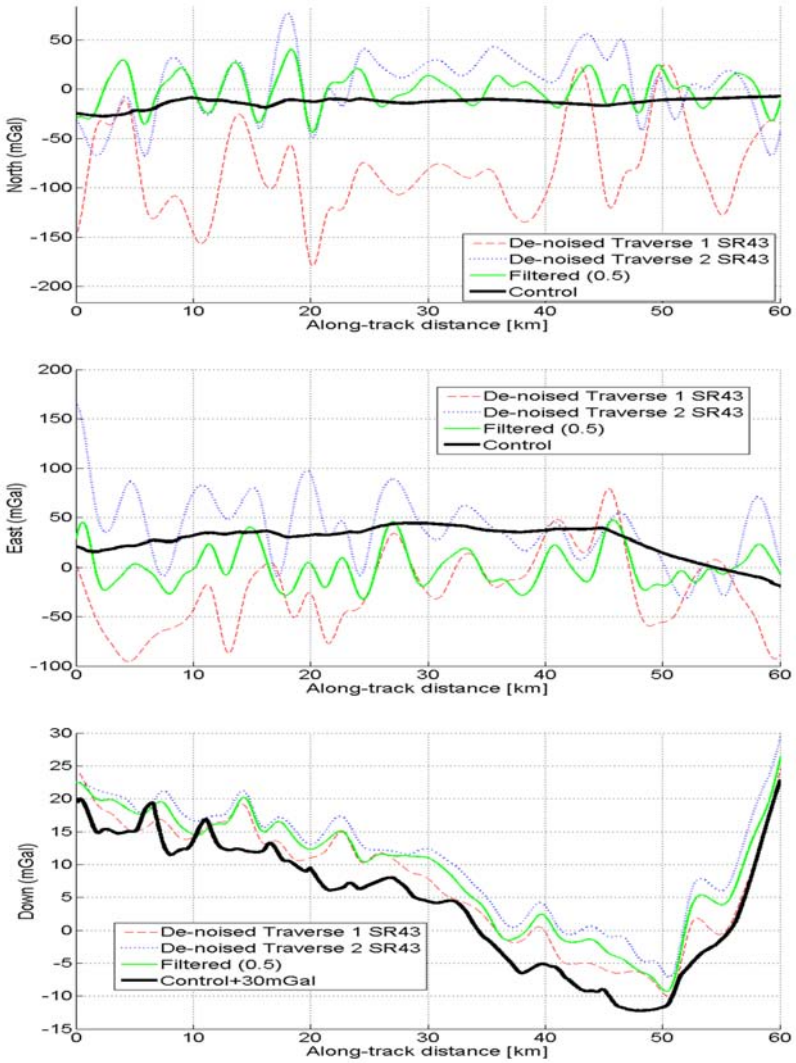

Figure 6.22: Gravity disturbance estimates on SR43 after wavelet de-noising and wave-number correlation

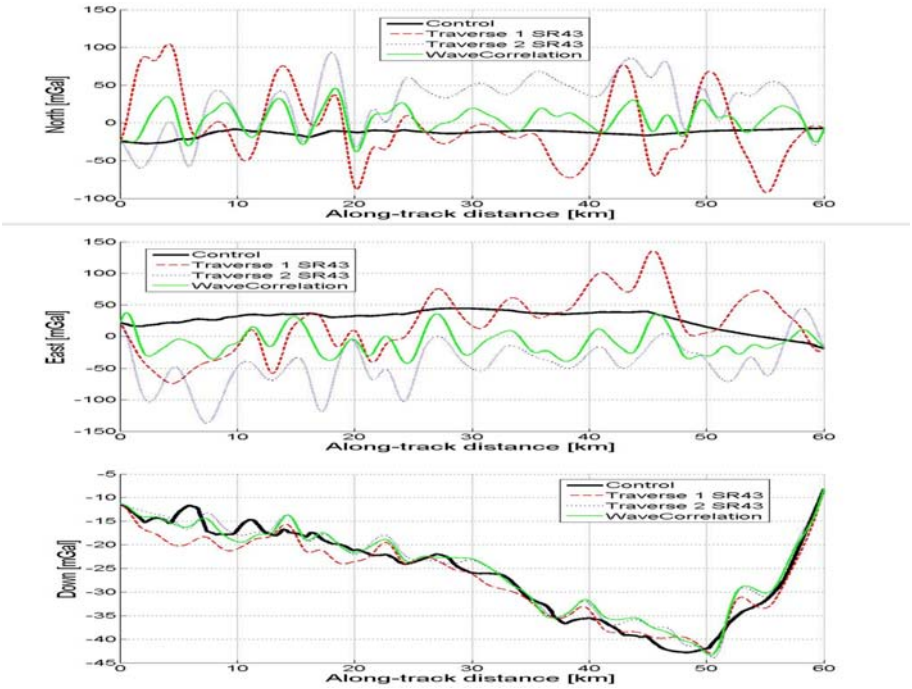

Figure 6.23: Gravity disturbance estimates on SR43 after wavelet de-noising, wave-number correlation and End point matching

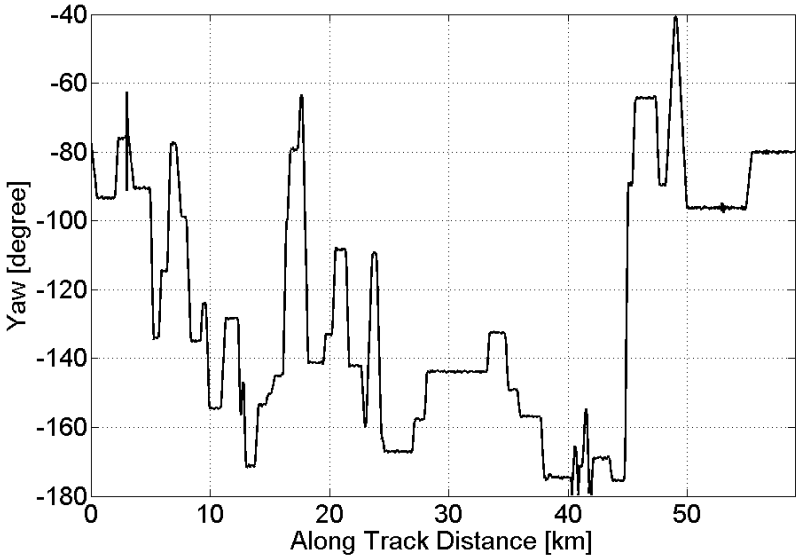

Figure 6.24: Heading direction of Traverse 2 SR43

6.3 Data Processing and results on SR1 and I90

Following the same procedure, the gravity disturbance estimates are obtained on other segments, i.e., SR1 and I90 (see Figure 6.3). Note, the extended I90 segment, indicated by the thick(blue) line in Figure 6.3, has a relatively worse DGPS position solution at the begining and the end parts, as shown in Figure 6.25. The final estimation results are shown in Figures 6.26-6.28. The statistics are shown in Table 6.9. From the table and figures, we see the down component estimates have about 2-3 mGal precision compared with the interpolated control data. Slightly worse results in the extended I90 part are mainly due to the degradation of the DGPS solution. The system repeatability can be as good as 0.64mGal. In addition, the repeatability suffers from the co-location error between the traverses. We note that for I90 (indicated by the red line in Figure 6.3), Traverses 2 and 3 were run in opposite directions. There is typically 25 to 30m, up to 100m, in the physical separation of the driving lanes of the interstate highway. As a result, the "repeatability" is worse compared with the repeatability between Traverse 2 and Traverse 4, which have the same traveling direction (1.77 mGal, st.dev. vs. 0.64 mGal). Also, Traverse 1 and 2 on SR43 were run in opposite directions, but in this case it is a two-lane road and the positioning discrepancy is only about 3m.

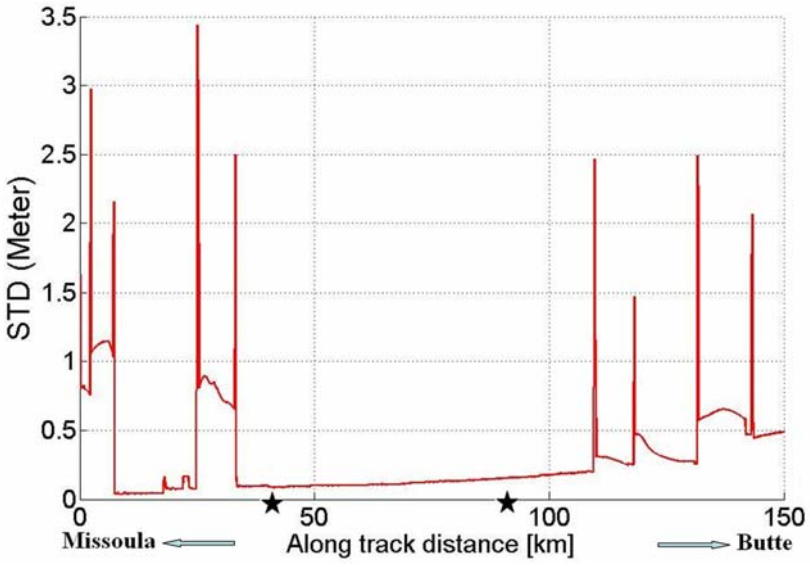

Figure 6.25: Positioning precision along extended I90, indicated by Applanix^{TM}. The two stars are the begining and end points of segment I90.

mGal	I90		I90 Extended		SR1	
	Mean	st.dev.	Mean	st.dev.	Mean	st.dev.
Trav1-Trav2					-0.26	2.46
Trav2-Trav3	2.48	1.77	-1.34	4.04		
Trav2-Trav4	-0.38	0.64	7.31	4.75		
Trav1-control					-0.03	2.47
Trav2-control	3.27	2.58	3.47	3.80	0.29	2.89
Trav3-control	0.79	2.05	4.80	2.83		
Trav4-control	3.65	2.84	-3.84	3.61		
WC(1,2)-control					2.21	2.67
WC(2,3)-control	2.03	2.16	4.54	2.82		
WC(2,4)-control	3.46	2.69	-0.16	2.97		

Table 6.9: The statistics of the differences relative to MQ-estimated control of the vertical gravity disturbance estimates after de-noising, wavenumber-correlation filtering, and end-matching.

As we have seen in the previous section, the horizontal component estimates are still problematic. However, the large estimation errors appear highly correlated between traverses. They are likely due to a systematic effect. Indeed, they are errors because the control values are accurate to better than 5mgal. We suspect an unestimable scale error in the accelerometers and gyros. By using the DEFLEC99 values, these scale errors can be estimated by equations (6.3.1) and (6.3.2).

$$\delta g_{N,E}^{DEFLEC99}(j) - \delta \overline{g}_{N,E}^{DEFLEC99} = \kappa_{N,E}(j)\left(\delta \hat{g}_{N,E}(j) - \delta \overline{\hat{g}}_{N,E}\right) \tag{6.3.1}$$

where a particular segment has J estimation points, $\delta \overline{g}_{N,E}^{DEFLEC99}$ is the average north or east DEFLEC99 gravity disturbance along the segment, and $\delta \overline{\hat{g}}_{N,E}$ is the average of the north or east INS/GPS gravity disturbance estimates. The final scale estimates are given by equation (6.3.2). For each traverse, the estimated scale parameters are shown in Table 6.10. On I90 Traverse 3, the procedure described in equations (6.3.1) to (6.3.2) can not provide reasonable results. So the values of Traverse 2 on I90 are used. Except that, most of the scale factors are of the same order of magnitude. However, they are not constant from traverse to traverse, and, their calibration in the absence of extensive control, therefore, remains a problem to be solved.

$$\overline{\kappa}_{N,E} = \frac{1}{J}\sum_{j=1}^{J}\left(\kappa_{N,E}(j)\right) \tag{6.3.2}$$

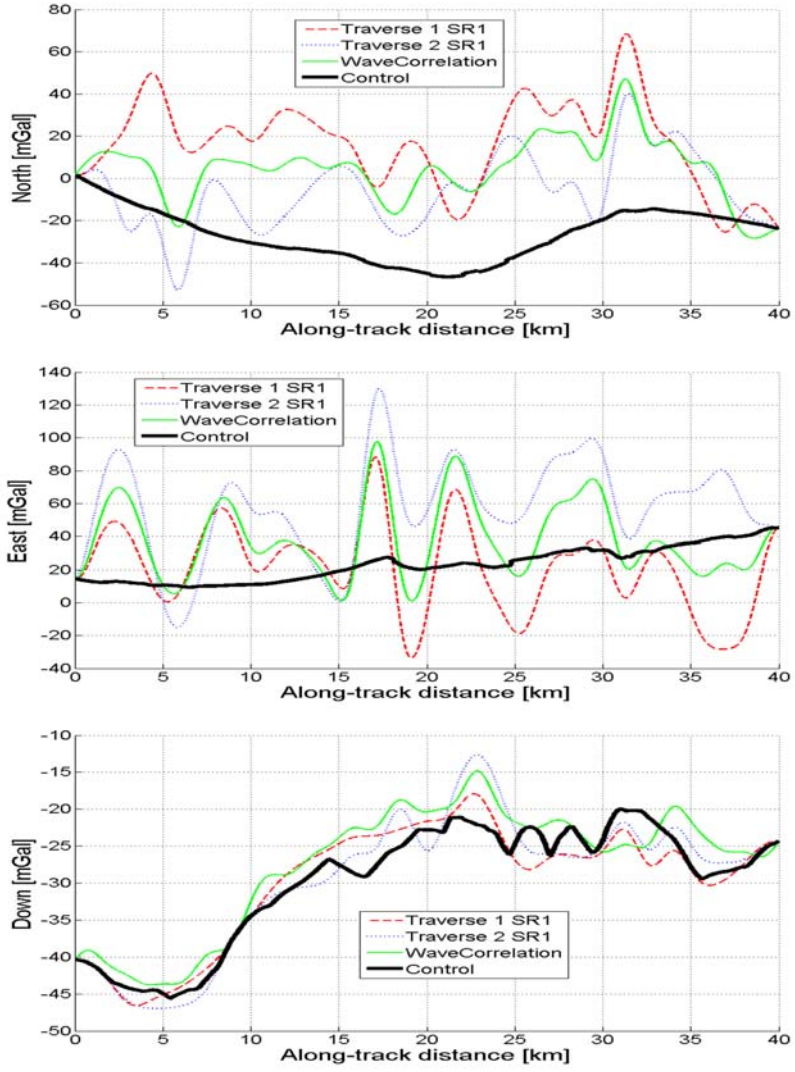

Figure 6.26: SR1 Gravity Disturbance Estimates Results after Kalman Filtering, Wavelet De-noising, Wave-number Correlation, and End Point Matching.

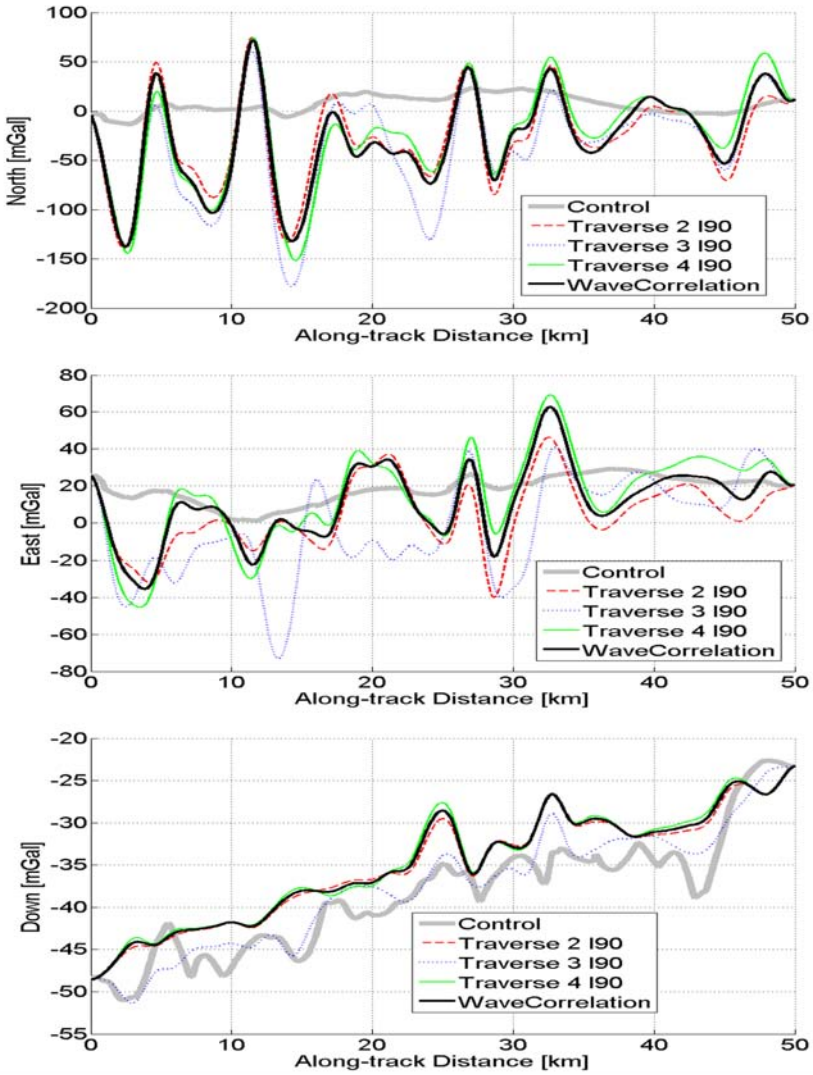

Figure 6.27: I90 Gravity Disturbance Estimates Results after Kalman Filtering, Wavelet De-noising, Wave-number Correlation, and End Point Matching.

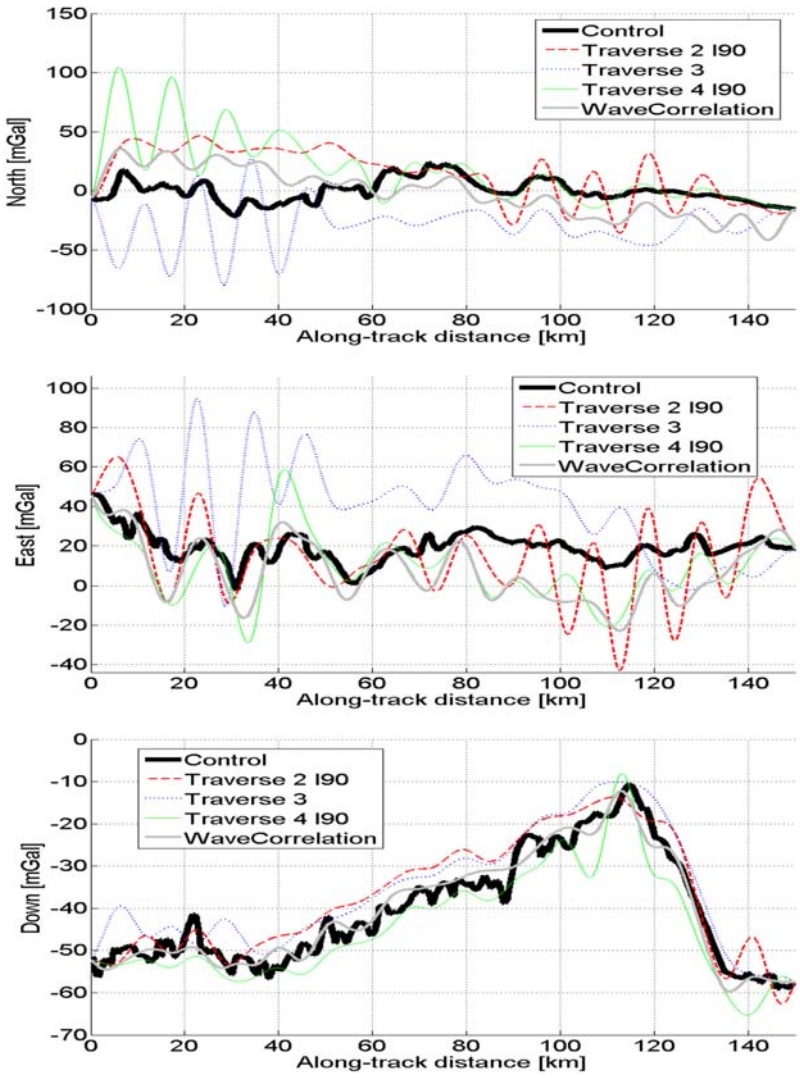

Figure 6.28: I90 Extended Part Gravity Disturbance Estimates Results after Kalman Filtering, Wavelet De-noising, Wave-number Correlation, and End Point Matching.

Scale Parameter	North	East
SR1 Traverse 1	0.28564410	0.26851645
SR1 Traverse 2	0.20040798	0.21776170
SR43 Traverse 1	0.04639524	0.03653619
SR43 Traverse 2	0.03724525	0.14321325
I90 Traverse 2	0.11819829	0.13316407
I90 Traverse 3	0.11819829	0.13316407
I90 Traverse 4	0.10246489	0.25810915
I90 Extended Part Traverse 2	0.28367589	0.14648047
I90 Extended Part Traverse 3	0.36641469	0.15979688
I90 Extended Part Traverse 4	0.24821640	0.16547760

Table 6.10: The estimated scale errors used to calibrate the horizontal component estimates.

mGal	North	East
	STD	STD
Traverse 1 -Traverse 2	8.26	6.74
Traverse 1 -CTL	5.04	8.24
Traverse 2 -CTL	8.75	9.77
Filtered -CTL	5.21	8.73

Table 6.11: Statistics of the rescaled horizontal component estimation errors on SR1.

$$\delta\hat{\hat{g}}_{N,E}(j) = \overline{\kappa}_{N,E}\left(\delta\hat{g}_{N,E}(j) - \delta\overline{\hat{g}}_{N,E}\right) + \delta\overline{g}^{DEFLEC99}_{N,E} \tag{6.3.3}$$

Using these scale error estimates, the horizontal estimates are calibrated according to equation (6.3.3). The results are shown in Figures 6.29-6.32 with the statistics of the estimation errors in Tables 6.11-6.14.

After removing the scale errors, the repeatability in the horizontal components is in the range of 2-15 mGal (st.dev.) and agreement with the control at the level of 5-9 mGal (st.dev.). Comparing Figures 6.26-6.28 with Figures 6.30-6.32, we see this simple calibration significantly reduces the differences with respect to the control data, and improves the internal repeatability, which proves our original assumption

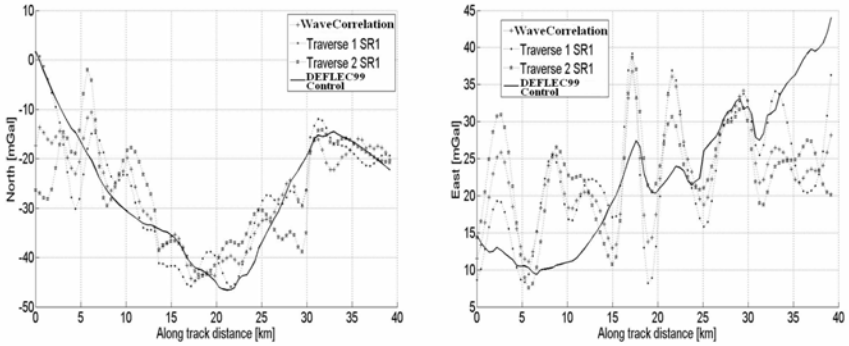

Figure 6.29: SR1 Horizontal Rescaled Gravity Disturbance Estimates.

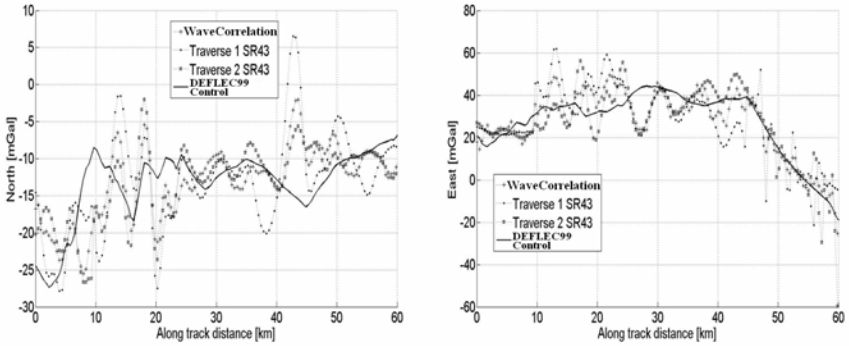

Figure 6.30: SR43 Horizontal Rescaled Gravity Disturbance Estimates.

mGal	North	East
	STD	STD
Traverse 1 -Traverse 2	5.22	14.90
Traverse 1 -CTL	6.64	12.16
Traverse 2 -CTL	5.38	9.89
Filtered -CTL	5.06	7.71

Table 6.12: Statistics of the rescaled horizontal component estimation errors on SR43.

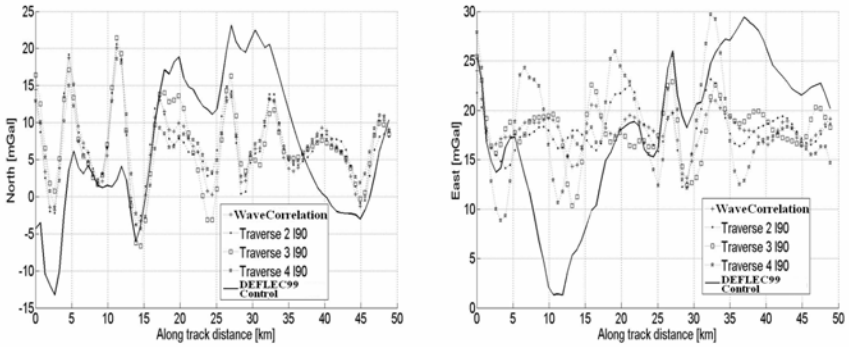

Figure 6.31: I90 Horizontal Rescaled Gravity Disturbance Estimates.

mGal	North	East
	STD	STD
Traverse 2 -Traverse 3	2.59	2.97
Traverse 2 -Traverse 4	2.02	3.28
Traverse 2 -CTL	8.89	7.17
Traverse 3 -CTL	9.20	7.04
Traverse 4 -CTL	8.64	8.03
Filtered (2,3)-CTL	8.86	7.32
Filtered (2,4)-CTL	8.95	7.44

Table 6.13: Statistics of the rescaled horizontal component estimation errors on I90.

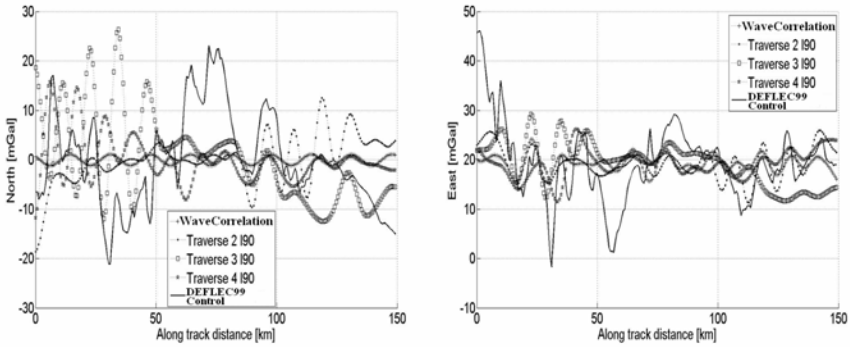

Figure 6.32: I90 Extended Part Horizontal Rescaled Gravity Disturbance Estimates.

mGal	North	East
	STD	STD
Traverse 2 -Traverse 3	11.08	5.02
Traverse 2 -Traverse 4	6.92	3.02
Traverse 2 -CTL	10.66	6.54
Traverse 3 -CTL	12.00	7.86
Traverse 4 -CTL	10.77	7.19
Filtered (2,3)-CTL	9.61	7.36
Filtered (2,4)-CTL	9.54	6.86

Table 6.14: Statistics of the rescaled horizontal component estimation errors on I90 extended part.

that the large oscillations are mainly due to a scale factor error. Indeed, it is known that the scale factor errors of inertial sensors are modeled reasonably well as random constants. That is, the scale factor error for the instrument may have a persistent value (as supposed here), but it is not necessarily constant from traverse to traverse. Thus, the success of the horizontal rescaling calibration is highly dependent on the availability of the control data. In another words, it is not guaranteed to yield good results if we apply the scale factors of one traverse to another traverse, even though it works some time, such as for Traverses 2 and 3 along I90.

CHAPTER 7

Conclusions

This study introduces the INS/GPS moving base gravimetric system. Both the theoretical issues and the practical concerns are thoroughly discussed. To my knowledge, this is the first time that the SINS/GPS based gravimetric system is working in a ground vehicle, which experiences much more severe observation conditions than the airborne system does.

To overcome the special difficulties encountered under this scenario, several cutting-edge techniques are applied in the data processing stage. First, the GPS positioning gaps are fixed by using a Two-stage Extended Kalman Filter, which is based on processing noise adapting. Second, the kinematic acceleration is determined by optimally combining the position-derived acceleration and the phase-derived acceleration. Third, the B-spline smoother and the modified Kalman filter are used to obtain a preliminary estimate of the gravity disturbance. Then the wavelet de-noising and the wave-number correlation methods are employed to further isolate the gravity disturbances from the remaining random errors. Finally, the biases in the estimates are removed by using the end-matching method. Based on the analysis of a vast amount of real data collected in a mountainous area (southwestern Montana), we have the following conclusions.

1. The estimation of the gravity vector depends critically on the high performance of both the INS and the GPS instruments. Assuming the INS and the GPS receiver hardware operate satisfactorily, the most detrimental influence on the estimation was the loss of lock on GPS signal, causing data gaps in the position solution. The integrated GPS/INS solution only has meter level accuracy in 50-second gaps, and it is even worse when the gap is longer. As a result, the position-derived GPS accelerations were adversely affected.

2. The phase-derived GPS acceleration relaxes the stringent requirement on the positioning accuracy, but it requires cycle slip free phase observables. In the kinematic scenario, it is well known that fixing cycle slips is quite challenging. Furthermore, when cycle slips occur consecutively within a short period of time, the classical fitting and smoothing techniques do not work. Our new approach based on the Doppler

observables successfully solved this problem. The resulting acceleration slightly improves the precision of the gravity disturbances.

3. Gravity disturbance estimates show significant consistency (as good as 0.6 mGal, st.dev., but also as poor as 3.7mGal, st.dev.) in the vertical component on repeated traverses where GPS quality is considered adequate. The consistency in the horizontal components is lower and includes a scale error.

4. The accuracy of the horizontal component estimates improves substantially after adjusting for a scale factor error and bias, both determined from control data along the entire segment. While in an operational setting such control presumably would not be available, the analysis shows that the large horizontal component errors are of a simple character.

5. The estimates of the vertical gravity disturbance components, after wavelet de-noising, wavenumber correlation filtering, agree with the available control at the 2-3mGal level (st.dev) along traverses where GPS quality is considered adequate. Slightly higher standard deviations are obtained along the extended I90 segment on which the GPS quality shows instances of clear degradation.

6. Wavelet de-noising and wavenumber correlation filtering have a positive effect on the final estimation; however, they yield only a marginal improvement of a few tenths mGal in the standard deviation of the errors (relative to the control data). The biases in the estimation are removed by using the end-matching method.

7. Several interpolation techniques are used to interpolate the control data for the vertical component. Even though the LSC offers the best results at the testing points, its performance is not guaranteed considering the covariance matrix is singular most of the time. The extended 3D multiquadrics method was found to be the most stable one and we can assume that the corresponding interpolated control data has an accuracy of approximately 2-4 mGal. Therefore, the INS/GPS estimates may have better accuracy than indicated in Conclusion 5, above.

8. The resolution of the estimated gravity disturbances depends on the applied data smoothing and the speed of the vehicle. With the 180-second B-spline smoother and a vehicle speed of about 80km/hr (22m/s), we estimate a resolution of about 2km (minimum wavelengths of 4km).

We may conclude that the INS/GPS gravimetry system successfully recovers the vertical gravity disturbance at a resolution of 2km and an accuracy of least 2-3mGal (st.dev). The horizontal component estimates still have relative poor accuracy (5-9mGal, st.dev) after removing the scale factor error. Nevertheless, this study shows it is feasible to estimate the gravity disturbance vector using a ground-vehicle SINS/GPS system. To achieve better results, may require looking for new algorithms, as well as designing the operations more carefully. For instance, considering the abundance of the control data, we may employ an artificial neural network

to estimate the gravity disturbances; and considering the relatively high variations in the heading angle, we may add the heading angle constraints in the system dynamic equation.

APPENDIX A

BROADCAST EPHEMERIS AND IGS ORBITS

The GPS satellite coordinates can be computed from the GPS broadcast ephemeris. A typical record of the ephemeris is given in Figure A.1. Table A.1 describes the format and content of each record in the broadcast ephemeris.

```
     ---+----1----+----2----+----3----+----4----+----5----+----6----+----7----+----8
  1  1 05  6 15 19 59 44.0   .408574473113D-03  .204636307899D-11  .000000000000D+00
  2       .184000000000D+03  .100000000000D+01  .401766753200D-08  .244739469481D+01
  3       .100582838058D-06  .584817898925D-02  .828877091408D-05  .515364106369D+04
  4       .331184000000D+06  .484287738800D-07  .241494228274D+01 -.113621354103D-06
  5       .984256139156D+00  .230156250000D+03 -.167910727770D+01 -.770353558721D-08
  6       .157506563347D-09  .100000000000D+01  .132700000000D+04  .000000000000D+00
  7       .240000000000D+01  .000000000000D+00 -.325962901115D-08  .696000000000D+03
  8       .327912000000D+06  .400000000000D+01
```

Figure A.1: GPS broadcast ephemeris

The physical meaning of the parameters is shown in the Figure A.2. For more information about the broadcast ephemeris please refers to the RINEX document (Gurtner 2001).

The satellite ephemeris is broadcast two hours in advance of the epoch for which they were calculated. The parameters are given in terms of the ephemeris reference time (toe), which is normally the centre of the transmission period [Rizos 1999].

To compute the GPS satellite position by use of the above parameters, it is necessary to obtain precise GPS time first. The GPS system time is characterized by a week number and the number of seconds since the beginning of the current week. The following algorithm (Hoffman-Wellenhof et al. 2001) is used to compute the GPS week and seconds of the week.

Let the civil date be expressed by integer values for the year Y, month M, day D, and a real value for the time in hours UT. Then, the Julian day, JD, is obtained by

Line	Description	Field Width*
1	Satellite PRN number	I2
	Epoch (year with 2 digits, month, day, hour, minute, second)	I25I3,F5.1
	Clock bias(s), drift, drift rate (s^{-1}) $[a0, a1, a2]$**	3D19.12
2	Age of ephemerides data (s) [IODE]	3X,D19.12
	Sine term for r-correction (m) [Crs]	D19.12
	Mean motion difference (rad s^{-1}) $[\Delta n]$; Mean anomaly (rad) $[\overline{M}_0]$	2D19.12
3	Cosine term for u-correction (rad) [Cuc]; Eccentricity [e]	3X,2D19.12
	Sine term for u-correction (rad) [Cus]; Square root of semi-major axis ($sqrtm$)	2D19.12
4	Time of ephemerides (seconds of GPS week) [Toe]; Cosine term for i-correction (rad) [Cic]	3X,2D19.12
	Node's longitude (rad) $[\Omega_0]$; Sine term for i-correction (rad) [Cis]	2D19.12
5	Inclination (rad) $[i_0]$; Cosine term for r-correction (m) [Crc]	3X,2D19.12
	Argument of perigee (rad) $[\omega]$; Rate of node's longitude (rad s^{-1}) $[\dot{\Omega}]$	2D19.12
6	Rate of inclination (rad s^{-1}) $[\dot{i}]$; Codes on L2 channel	3X,2D19.12
	GPS week; L2 P data flag	2D19.12
7	SV accuracy; SV health; TGD; IODC Issue of data, Clock	3X,4D19.12
8	Transmission time of message (Sec of GPS week)	3X,D19.12
	Fit Interval (hours) zero if not known; Spare; Spare	3D19.12
Note	*: X denotes a blank space; I denotes an integer; F denotes a float number; D denotes a double precision number.	
	**: The units are of the quantities are in ( ). The symbols that represent the quantities are shown in [ ].	

Table A.1: Rinex navigation message description

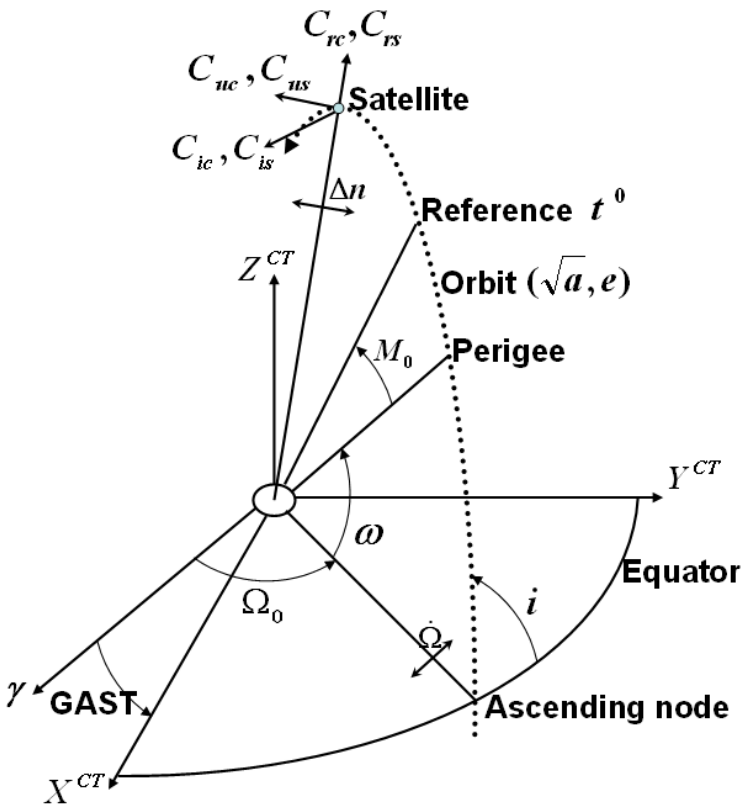

Figure A.2: GPS orbit parameter description

the following equation:

$$\text{JD} = \text{INT}[365.25y] + \text{INT}[30.6001(m+1)] + \text{D} + \text{UT}/24 + 172098.5 \qquad \text{(A.0.1)}$$

where INT denotes the integer part of a real number and y, m are given by:
$y = Y - 1$ and $m = M + 12$ if $M <= 12$
$y = Y$ and $m = M$ if $M > 12$.

The GPS week is obtained by:

$$\text{Week} = \text{INT}[(\text{JD} - 2444244.5)/7] \qquad \text{(A.0.2)}$$

The seconds of the week is obtained by using the following equations:

$$\begin{aligned} &a = \text{INT}(\text{JD} + 0.5) \Rightarrow b = a + 1537 \Rightarrow c = \text{INT}[(b - 122.1)/365.25] \\ &\Rightarrow d = \text{INT}[365.25c] \Rightarrow e = \text{INT}[(b - d)/30.600 \Rightarrow \\ &\text{DD} = b + d - \text{INT}[30.6001/e] + \text{FRAC}[\text{JD} + 0.5] \end{aligned} \tag{A.0.3}$$

where FRAC denotes the fractional part of a number.

The seconds of week, SOW, is given by:

$$\text{SOW} = [\text{FRAC}(\text{DD}) + N + 1] * 86400.0d0 \tag{A.0.4}$$

where N = modulo{INT[JD+0.5],7}.

However, this textbook algorithm only provides seconds of week with precision at 10^{-5} seconds. As a result, the Remondi DATE/TIME algorithm (Hilla et al. 2000) is used instead.

The satellite coordinates are computed for a given epoch t with respect to the Earth-fixed geocentric reference frame by the following equations.

$$t_k = t - toe \tag{A.0.5}$$

A possible change of the week has to be considered i.e.,

$$\text{if} \quad t_k = 302400 \quad t_k = 302400 \tag{A.0.6}$$

$$\text{if} \quad t_k > 302400 \quad t_k = t_k - 302400 * 2 \tag{A.0.7}$$

$$\text{if} \quad t_k < -302400 \quad t_k = t_k + 302400 * 2 \tag{A.0.8}$$

$$\tag{A.0.9}$$

$$n_0 = \sqrt{\frac{GM}{A^3}} \tag{A.0.10}$$

where $GM = 3.986005d14m^3/s^2$, $A = \sqrt{A}^2$

$$n = n_0 + \Delta n \text{ corrected mean motion} \tag{A.0.11}$$

$$\overline{M}_k = \overline{M}_0 + n * t_k \text{ mean anomaly} \tag{A.0.12}$$

Kepler's equation of eccentric anomaly

$$E_k = \overline{M}_k + e * \sin E_k \tag{A.0.13}$$

It is solved by iteration. Because of the very small eccentricity of the GPS orbits (e< 0.001) usually two steps are sufficient.

The satellite coordinates are then obtained, using the following equations:

$$\cos v_k = \frac{\cos E_k - e}{1 - e * \cos E_k} \text{ true anomaly} \tag{A.0.14}$$

$$\sin v_k = \frac{\sqrt{1-e^2}\sin E_k}{1 - e * \cos E_k} \text{ true anomaly} \tag{A.0.15}$$

$$\Phi_k = v_k + \omega \text{ argument of latitude} \tag{A.0.16}$$

where $\omega = 7.2921151467 * 10^{-5}\ rad/s$.

$$\delta u_k = C_{uc}\cos 2\Phi_k + C_{us}\sin 2\Phi_k \text{ argument of latitude correction} \tag{A.0.17}$$

$$\delta r_k = C_{rc}\cos 2\Phi_k + C_{rs}\sin 2\Phi_k \text{ radius correction} \tag{A.0.18}$$

$$\delta i_k = C_{ic}\cos 2\Phi_k + C_{is}\sin 2\Phi_k \text{ inclination correction} \tag{A.0.19}$$

$$u_k = \Phi_k + \delta u_k \text{ corrected argument of latitude} \tag{A.0.20}$$

$$r_k = A(1 - 2\cos E_k) + \delta r_k \text{ corrected radius} \tag{A.0.21}$$

$$i_k = i_0 + \dot{i} * t_k + \delta i_k \text{ corrected inclination} \tag{A.0.22}$$

$$X'_k = r_k \cos u_k \text{ position in the orbital plane} \tag{A.0.23}$$

$$Y'_k = r_k \sin u_k \text{ position in the orbital plane} \tag{A.0.24}$$

$$\Omega_k = \Omega_0 + (\dot{\Omega} - \omega_e)t_k - \omega_e t_{oe} \text{ corrected longitude of ascending node} \tag{A.0.25}$$

Earth-fixed geocentric satellite coordinates

$$X_k = X'_k \cos\Omega_k - Y'_k \sin\Omega_k \cos i_k \tag{A.0.26}$$

$$Y_k = X'_k \sin\Omega_k + Y'_k \cos\Omega_k \cos i_k \tag{A.0.27}$$

$$Z_k = Y'_k \sin i_k \tag{A.0.28}$$

A set of GPS data is used to validate the above computation procedures. The resulting GPS satellite coordinates are compared with the interpolated IGS precise orbits (see section 4.3). The differences of the satellite coordinates at exactly the same epoch for PRN15, PRN18 are shown in Figure A.3.

In Figure A.3, we see that the differences between the broadcast orbit and the IGS precise orbit could reach several meters. The jumps in the differences probably due to the change of broadcast orbit parameters, which are obtained from a curve

fit to the predicted ephemeris over an interval of 4 to 6 hours. As a result, the IGS precise orbit is used in the GPS data processing described in Chapter 4.

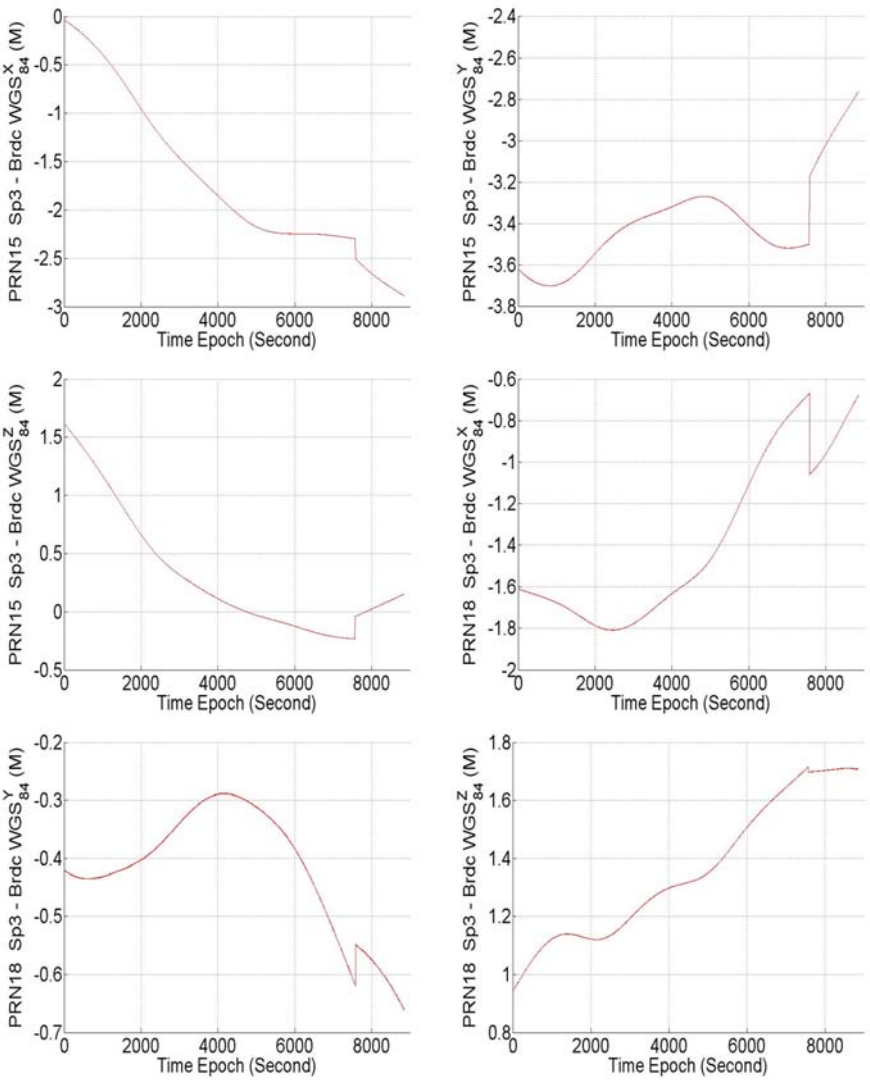

Figure A.3: Broadcast and precise GPS orbit differences

APPENDIX B

THE MODIFIED KALMAN SYSTEM FOR ESTIMATING GRAVITY DISTURBANCES

The observation matrix H is given by equation B.0.1.

$$H := \begin{bmatrix} -C_b^i & 0 & -\text{diag}\{a^i\}C_b^i & 0 & -a^i\times \end{bmatrix} \tag{B.0.1}$$

where a^i is the INS acceleration, C_b^i is the transformation matrix from b-frame to i-frame, $\text{diag}\{a^i\} = \begin{bmatrix} a_1^i & 0 & 0 \\ 0 & a_2^i & 0 \\ 0 & 0 & a_3^i \end{bmatrix}$, and $a^i\times = \begin{bmatrix} 0 & -a_3^i & a_2^i \\ a_3^i & 0 & -a_1^i \\ -a_2^i & a_1^i & 0 \end{bmatrix}$.

The state transition matrix Φ is given by equation B.0.2.

$$\Phi := \begin{bmatrix} 0 & 0 & 0 & 0 & 0 \\ 0 & 0 & 0 & 0 & 0 \\ 0 & 0 & 0 & 0 & 0 \\ 0 & 0 & 0 & 0 & 0 \\ 0 & -C_b^i & 0 & -C_b^i[\omega_{ib}^b] & 0 \end{bmatrix} \tag{B.0.2}$$

where ω_{ib}^b is the angular velocity of the b-frame with respect to the i-frame with coordinates in the b-frame.

APPENDIX C

POWER SPECTRAL DENSITY OF THE GPS AND INS ACCELERATIONS IN BOTH AIRBORNE AND GROUND SCENARIO

The data from Traverse 3 along I90 and a typical airborne data set provided by NGA are used to demonstrate the effects in the INS/GPS vector gravimetry caused by different observation scenarios. Figure C.1 shows seven passes in one flight test. Table C.1 gives a short summary of each pass. Here, only the data from pass 6 are used in the following analysis. The results from other passes are similar.

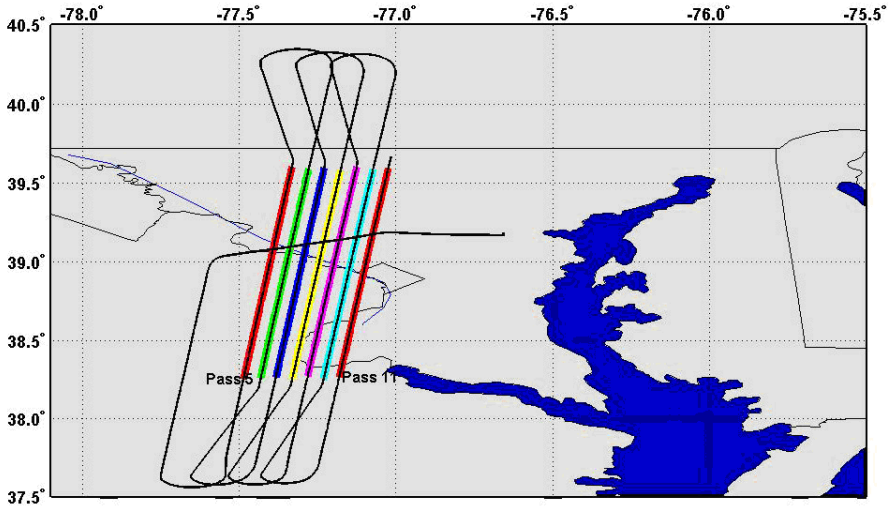

Figure C.1: Trajectory of the airborne data provided by NGA

Table C.1: Summary of the passes in the flight test provided by NGA

Flight / pass	duration [s]	mean altitude [m]	length [km]	velocity [m/s]	Sampling Rate[Hz]
FLT02/5	767	6342.476	150.976	196.846	
FLT02/6	963	6333.064	148.953	154.597	GPS 2
FLT02/7	794	6330.765	148.974	187.630	
FLT02/8	1007	6325.897	148.838	147.807	INS 25
FLT02/9	819	6303.257	149.014	181.952	
FLT02/10	1054	6301.224	148.930	141.302	
FLT02/11	844	6299.020	148.113	175.386	

Figure C.2 - C.7 show the power spectral density of the raw (unsmoothed) accelerations. We see the frequency contents of both the GPS and INS accelerations in the ground-vehicle system are more complicated than in the airborne case.

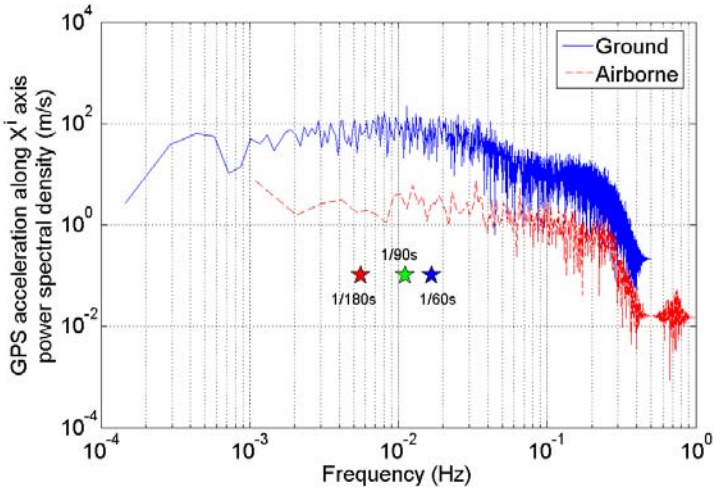

Figure C.2: Power spectral density of the GPS accelerations along x component

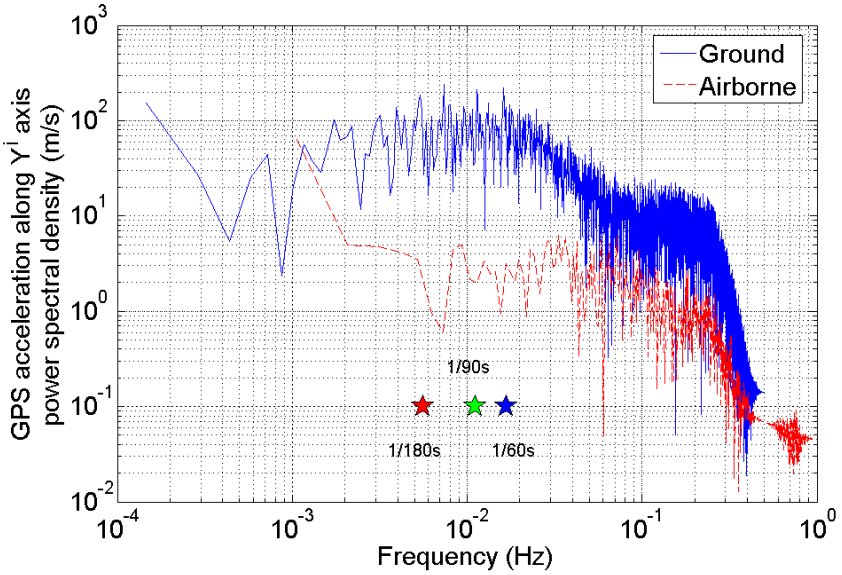

Figure C.3: Power spectral density of the GPS accelerations along y component

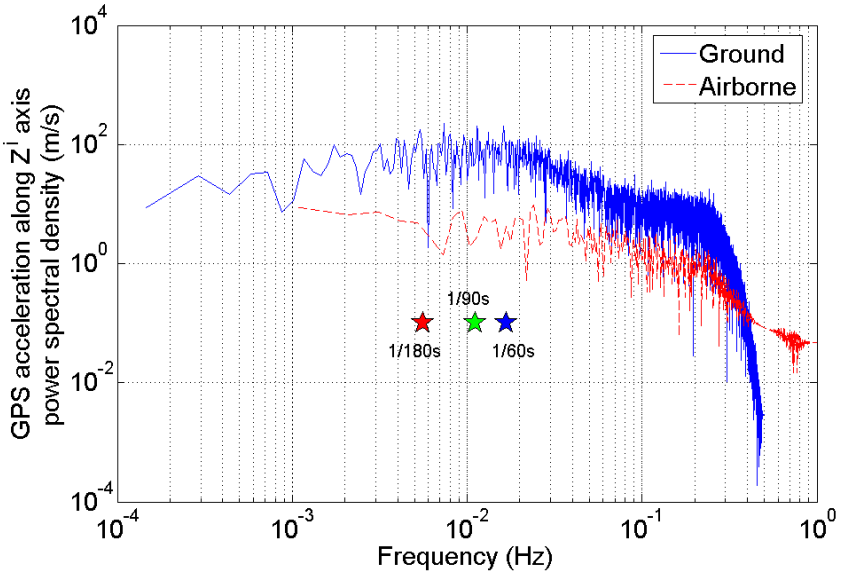

Figure C.4: Power spectral density of the GPS accelerations along z component

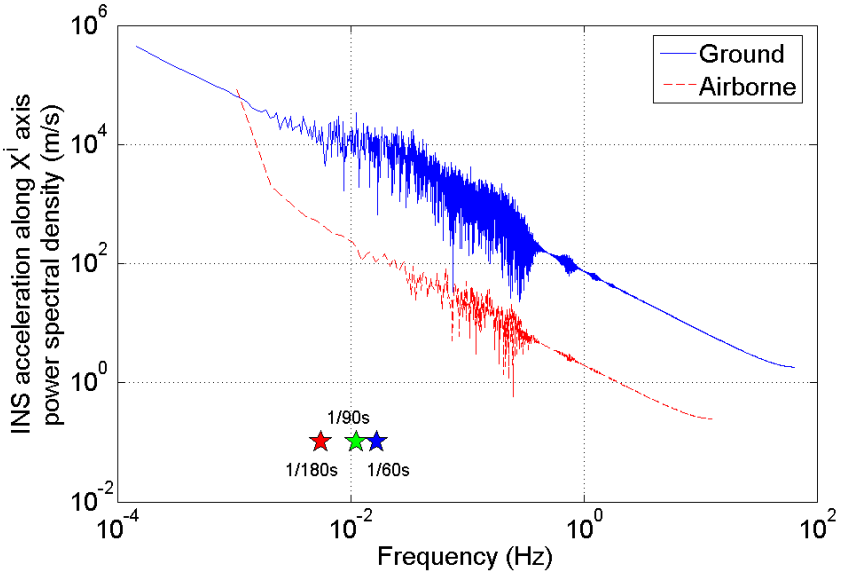

Figure C.5: Power spectral density of the INS accelerations along x component

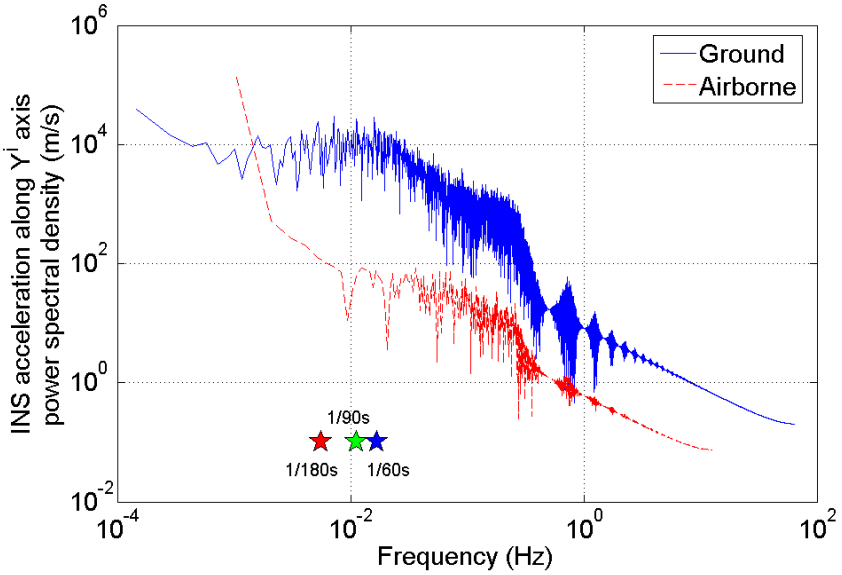

Figure C.6: Power spectral density of the INS accelerations along y component

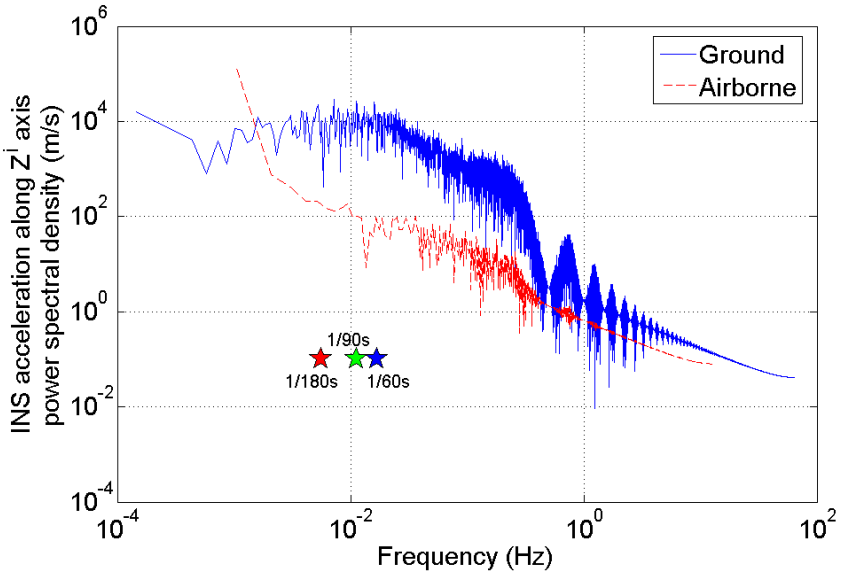

Figure C.7: Power spectral density of the INS accelerations along z component

REFERENCES

Bastos, L., Landau, H. (1988). Fixing cycle slips in dual-frequency kinematic GPS-applications using Kalman filtering. *Manuscripta Geodaetica*, *13(4)*: 249-256.

Bell, R., Childers, V., Arko, R., Blankenship, D. & Brozena, J. (1999). Airborne gravity and precise positioning for geologic applications. *Geophysical Research Letters*, *104*, 15 281-15 292.

Bisnath, S.B. (2000). Efficient, automated cycle-slip correction of dual-frequency kinematic GPS data. *Proceedings of ION GPS 2000*, Salt Lake City, Utah, 19-22 September: 145-154.

Brozena, J.M. (1992). The Greenland Aerogeophysics Project: Airborne Gravity, Topographic and Magnetic Mapping of an Entire Continent. *Proceedings of International Association of Geodesy Symposium G3: Determination of the Gravity Field by Space and Airborne Methods*. Springer Verlag, 203-214.

Bruton, A.M., Glennie, C. L. & Schwarz, K. P. (1999). Differentiation for High-recision GPS Velocity and Acceleration Determination. *GPS Solutions*, Vol. 2, No. 4.

Bruton, A.M., Schwarz, K. P. & Skaloud, J. (2000). The Use of Wavelets for the Analysis and De-noising of Kinematic Geodetic Measurements. *Proceedings of the International Association of Geodesy Symposia No. 121, Geodesy Beyond 2000: The Challenges of the First Decade*, Birmingham, UK.

Cheney, W. and Kincaid, D. (1994). *Numerical Mathematics and Computing*. (3rd ed.), Pacific Grove, CA: International Thomson Publishing Company.

Childers, V., Bell, R. & Brozena, J. (1999). Airborne gravimetry: an investigation of filtering. *Geophysics*, *64*, 61-69.

Daubechies, I. (1992). *Ten lectures on Wavelets*, SIAM: Philadelphia.

Donoho D.L. and Johnstone, I.M. (1994). Ideal Spatial Adaptation via Wavelet Shrinkage. *Biometrika*, *Vol. 81*, 425-455.

Donoho, D. L. and Johnstone, I. M. (1995). Adapt to unknown smoothness via wavelet shrinkage. *Journal of The American Statistical Association*, 90, 1200-1224.

El-Gizawy, M., El-Sheimy, N., Re. D., Taha, M. & Noureldin, A. (2004). Neuro-Fuzzy System for GPS/INS Integration. *Proceedings of the European Navigation Conference (GNSS 2004)*, Rotterdam.

El-Sheimy, N., Nassar, S. & Noureldin, A. (2004). Wavelet De-noising for Fast and Accurate Alignment of Inertial Measurement Units Techniques. *IEEE Aerospace and Electronic Systems*, *Volume: 19, Issue*: 10, 32-39.

Franke, R. (1982). Scattered data interpolation: tests of some methods. *Mathematics of Computation*, *38 (157)*, 181-200.

Franke, R. (1987). Recent advances in the approximation of surfaces from scattered data. *Topics in Multivariate Approximation*, C. K. Chui, L. L. Schumaker, and F. I. Utreras, eds., Orlando, Florida: Academic Press, Inc.: 79-98.

Friedland, B. (1969). Treatment of Bias in Recursive Filtering. *IEEE Transaction on. Automatic Control, AC-14*: 359-367

Forsberg, R., Olesen, A.V. & Keller, K. (1999). Airborne Gravity Survey of the North Greenland Shelf 1998. *Kort & Matrikelstyrelsen Technical Report*.

Goad, C. (1986). Precise Positioning with the Global Positioning System. *Proceedings of the Third International Symposium on Inertial Technology for Surveying and Geodesy*, September 16-20, 1985, Banff, Canada: 745-756.

Gao, Y., Li, Z. (1999). Cycle slip detection and ambiguity resolution algorithms for dual-frequency GPS data processing. *Marine Geodesy, Vol. 22*, no. 4: 169-181.

Gurtner, W. (2001). RINEX: the Receiver Independent Exchange Format Version 2.10. *http://. www.ngs.noaa.gov/CORS/Rinex2.html*. Cited 27 Sep 2007.

Gustafsson, F., Gunnarsson, F., Bergman, N., Forssell, U., Jansson, J., Karlsson, R., & Nordlund, P. (2002). Particle filters for positioning, navigation and tracking. *IEEE Trans. Signal Process*, *50 (2)* 425-437.

Hammond, S. and Murphy, C.A. (2003). Air-FTG^{TM}: Bell Geospace's Airborne Gravity Gradiometer - a description and case study. *ASEG Preview*, *105*, 24-26.

Hannah, J. (2001). *Airborne Gravimetry: A Status Report*. Department of Surveying. University of Otago, Dunedin.

Hardy, R.L. (1971). Multiquadric Equations of Topography and Other Irregular Surfaces , *Geophys. Res., 176*: 1905-1915.

Harrison, J.C., MacQueen, J.D., Rauhut, A.C., & Cruz, J.Y. (1995). The LCT Airborne Gravity System. *International Association of Geodesy Symposium G4, IUGG XXI General Assembly*. Boulder, Colorado.

Heiskanen, W.A., Moritz, H. (1967). *Physical Geodesy*. W. H. Freeman and Company, San Franscisco and London.

Hide, C., Moore, T., Smith, M. (2003). Adaptive Kalman filtering for low cost GPS/INS. *Journal of navigation, vol. 56*, no. 1: 143-152.

Hilla, S. and Jackson, M. (2000). The GPS Toolbox. *GPS Solutions*, *Vol. 3, Issue: 4*, 71-74.

Hirt, C. and Burki, B. (2002). The Digital Zenith Camera -A New High-Precision and Economic Astrogeodetic Observation System for Real-Time Measurement of Deflections of the Vertical. Proc. of the 3rd Meeting of the *International Gravity and Geoid Commission of the International Association of Geodesy*, Thessaloniki, Greece (ed. I. Tziavos): 161-166.

Hoffman-Wellenhof, B., Lichtenegger. H, & Collins, J. (2001). *GPS theory and practice*. 5th edn. Springer, Berlin Heidelberg New York, ISBN 3-211-83534-2.

Honeywell Sensotec Inc. *http://www.sensotec.com/accelerometer_faq.asp?27*, 2080 Arlingate Lane, Columbus, Ohio 43228, USA. Cited 20 Sep 2007.

Hu, C., Chen, Y., Chen, W. (2001). Adaptive Kalman filtering for DGPS positioning. *In Proceedings ofthe International Symposium on Kinematic Systems in Ceodmy, Geomorics and Navigation (KIS)*, Eon8 Canada.

Hubeli, A., Gross, M. (2000). A survey of surface representations for geometric modeling. *Technical Report, 335*, ETH Z urich, Institute of Scientific Computing.

Ignagni, M.B. (1981). An alternate derivation and extension of Friedland's twostage Kalman estimator. *IEEE Trans. Autom. Contr., AC-26*, 746–750.

Ignagni, M.B. (1990). Separate-bias Kalman estimator with bias. state noise. *IEEE Trans. Automat. Contr. 33*, 338-341.

Jeffreys, H. and Jeffreys, B. S. (1988). *Methods of Mathematical Physics*, 3rd ed. Cambridge, England: Cambridge University Press.

Jekeli, C. (1993). A review of gravity gradiometer survey system data analysis. *Geophysics,Vol.58, No.4*, 508-514.

Jekeli, C. (1994). On the computation of vehicle accelerations using GPS phase accelerations. *Proceedings of International Symposium of Kinematic Systems in Geodesy, Geomatics and Navigation (KIS94)*, Banff, Alberta. Department of Survey Engineering, the University of Calgary, 473-482.

Jekeli, C. (1995). Airborne vector gravimetry using precise, position-aided inertial measurement units. *Bulletin Godsique, Vol.69, No.1, 1-11*

Jekeli, C. (2000). *Inertial Navigation Systems with Geodetic Applications*. Berlin: Walter de Gruyter, xiii+352.

Jekeli, C. (2003). Statistical analysis of moving-base gravimetry and gravity gradiometry: Report no.466, Geodetic Science, Ohio State University, Columbus, Ohio.

Jekeli, C., and Garcia, R. (1997) GPS phase acceleration for moving-base vector gravimetry. *Journal of Geodesy, Vol, 71, No. 10*, 630-639.

Jekeli, C. and Kwon, J.H. (1999). Results of airborne vector (3-D) gravimetry. *Geophysical Research Letters, Vol.26, No.3*, 3533-3536.

Jekeli, C. and Li, X. (2006). INS/GPS Vector Gravimetry along Roads in Western Montana. OSU Report No. 477, Dept. of Geodetic Science and Surveying, The Ohio State University, Columbus Ohio, USA.

Jekeli, C. and Serpas J.G. (2003). Review and numerical assessment of the direct topographical reduction in geoid determination. *Journal of Geodesy, 77*,226-239.

Jwo, D.J. and Huang H.C. (2005). GPS Navigation Using Fuzzy Neural Network Aided Adaptive Extended Kalman Filter. *Proceedings of the 44th IEEE Conference on Decision and control, and the European Control Conference 2005*, Seville, Spain.

Julier, S.J., Uhlmann, J.K. (2004). Unscented Filtering and Nonlinear Estimation. *Proc. of the IEEE 92*: 401-422.

Kalman, R. E. (1960). A new approach to linear filtering and prediction problems. textitTransaction of the ASME, series D 82, 35-45.

Kaygisiz. B.H., Erkmen, A.M. & Erkmen, I. (2003). GPS/INS Enhancement Using Neural Networks for Autonomous Ground Vehicle Applications. *Proceedings of the 2003 IEEE/RSJ Intl. Conference on Intelligent Robots and Systems*, Las Vegas, Nevada.

Kennedy, S. (2002). "Precise Acceleration Determination from Carrier Phase Measurements." *Proceedings of ION GPS 2002*, Portland, Oregon, 24-27 September 2002, pp. 962-972.

Kim, D., Langley, R.B. (2001). Instantaneous real-time cycle-slip correction of dual frequency GPS data. *In: Proc. Of International Symposium on Kinematic Systems in Geodesy, Geomatics and Navigation (KIS2001)*, Banff, Alberta, 5-8 June, pp. 255-264.

Kim, K.H., Jang, G.L., Park, C.G. (2006). Adaptive Two-Stage EKF for INS-GPS Loosely Coupled System. Submitted to IEEE.

Kleusberg. A, Peyton, D. and Wells, D. (1990). Airborne gravimetry and the Global Positioning System. *Proceedings of IEEE PLANS 1990*, Las Vegas, published by: IEEE, Piscataway, NJ, 273-278.

Knickmeyer, E. T. (1990). Vector gravimetry by a combination of inertial and GPS satellite measurements, Doctoral Dissertation, USCE Report No. 20035, Department of Survey Engineering, the University of Calgary.

Kwon, J.H. (2000). Airborne Vector Gravimetry Using GPS/INS, Doctoral Dissertation, OSU Report No.453, Dept. of Geodetic Science and Surveying, The Ohio State University, Columbus Ohio, USA.

Kwon, J.H. and Jekeli C. (2001). A new approach for airborne vector gravimetry using GPS/INS. *Journal of Geodesy, 74(10)*, 690-700.

Leick, A. (2004). *GPS Satellite Surveying*, 3rd ed. New York: Wiley.

Li, X. and Jekeli, C. (2004). Improving resolution of airborne gravimetric system by use of wavelet shrinkage denoising. *Proceedings of 60th ION Annual Meeting*, 491-496.

Li, X. and Jekeli, C. (2006). Ground-Vehicle INS/GPS Vector Gravimetry Assessment Using Repeated Traverses in Montana. *Proceedings of The First Symposium of the International Gravity Field Services.*

Mautz, R., Schaffrin, B., Kaschenz, J. (2003). Biharmonic Spline Wavelets versus Generalized Multi-quadrics for Continuous Surface Representations, *International Association of Geodesy Symposia, Symposium G04, Volume 128*, pp500-505.

Mohamed, A.H., Schwarz, K.P. (1999). Adaptive Kalman filtering. for INS/GPS. *Journal of Geodesy, 73*: 193-203.

Murphy, C.A. (2004). The Air-FTG^{textTM} airborne gravity gradiometer system. Abstracts from the ASEG-PESA airborne gravity 2004 workshop.

Myers, K.A., Tapley, B.D. (1976). Adaptive sequential estimation with unknown noise statistics. *IEEE Trans. Automat. Contr., vol. 21*: 520-523.

Nassar, S. (2003). Improving the Inertial Navigation System (INS) Error Model for INS and INS/DGPS Applications, (Doctoral Dissertation), UCGE Report No. 20183, Department of Survey Engineering, the University of Calgary.

Nassar, S. and El-Sheimy, N. (2005).Wavelet Analysis For Improving INS and INS/DGPS Navigation Accuracy, *Journal of Navigation, vol. 58, Issue 1*, 119-134.

Olesen, A.V., Forsberg, R. & Gidskehaug, A. (1997). Airborne Gravimetry Using the LaCoste and Romberg Gravimeter - An Error Analysis. *Proceedings of International Symposium on Kinematic Systems in Geodesy, Geomatics and Navigation (KIS97)*, Banff, Canada, June 3-6, 613-618.

Remondi, B. W. (1984). Using the Global Positioning System (GPS) phase observable for relative geodesy: Modeling, processing, and results. Ph.D. dissertation, Center for Space Research, University of Texas at Austin, May 1984.

Rizos, C. (1999). Principles and Practice of GPS Surveying, *Monograph 17*, School of Geomatic Engineering, University of New South Wales. *http://www.gmat.unsw.edu.au/snap/gps/gps_survey/principles_gps.htm.* Cited on Sept. 27, 2007.

Salychev, O.S., Bykovsky, A.V., Voronov, V.V., Schwarz, K.P., Liu, Z., Wei, M. & Paneka, J. (1994). Determination of gravity and deflections of the vertical for geophysical applications using the ITC-2 platform. *Proceedings, International Symposium on Kinematic Systems in Geodesy, Geodynamics and Navigation*, University of Calgary, 521-529.

Sasiadek, J. Z., Wang, Q. & Zeremba, M. B. (2000). Fuzzy adaptive Kalman filtering for INS/GPS data fusion, *Proceedings of the 15th IEEE international symposium on intelligent control*, Rio, Patras, Greece, pp.181-186.

Schaffrin, B., Kwon, J.H. (2002). A Bayes filter in Friedland form for INS/GPS vector gravimetry, *Geophys. J. Int.*, 149(1): 64-75

Schwarz, K.P., Columbo, O.L., Hein, G. & Knickmeyer, E.T. (1992). Requirements for airborne vector gravimetry. *Proceedings International Association of Geodesy Symposia, From Mars to Greenland: Charting Gravity with Space and Airborne Instruments, No.110*,273-283.

Schwarz, K.P. and Wei, M. (1994). Some unsolved problems in airborne gravimetry. *Proceedings of the International Association of Geodesy Symposium 113, Gravity and Geoid*. Springer, Berlin, 131-150.

Seeber, G. (2003). *Satellite Geodesy*. Walter de Gruyter and Co., Berlin, 531 pp.

Serpas, J.G. (2003). *Local and regional geoid determination from vector airborne gravimetry*. Doctoral Dissertation, OSU Report No. 468. Dept. of Geodetic Science and Surveying, The Ohio State University, Columbus Ohio, USA.

Smith, D.A., and D.R. Roman, 2001, GEOID99 and G99SSS: 1 arc-minute geoid models for the United States. *Journal of Geodesy*, 75(9-10), 469-490.

Serrano, L., Kim, D. & Langley, R.B. (2004). A Single GPS Receiver as a Real-Time, Accurate Velocity and Acceleration Sensor. *Proceedings of ION GNSS 2004*, Long Beach, California, 21-24.

Shin, E.H. (2005). Estimation Techniques for Low-Cost Inertial Navigation, (Doctoral Dissertation), UCGE Report 20219, Department of Survey Engineering, the University of Calgary.

Strang, G. (1989). *Wavelets and dilation equations: A brief introduction*, SIAM Review 31, 614-627.

Strang, G. and Nguyen, T. (1996). *Wavelets and Filter Banks*. Wellesley-Cambridge Press.

Taswell, C. (2000). The what, how, and why of wavelet shrinkage denoising. *IEEE Computing in Science & Engineering, 2(3)*, 12-19.

Taswell, C. (2001). Experiments in Wavelet Shrinkage Denoising. *Journal of Computational Methods in Science and Engineering 1(2s-3s)*, 315-326.

Wan, E.A., and van der Merwe, R. (2000). The Unscented Kalman Filter for Nonlinear Estimation. *In Proceedings of Symposium 2000 on Adaptive Systems for Signal Processing*, Communication and Control (AS-SPCC), IEEE, Lake Louise, Alberta, Canada.

Wang J. and Wang J.L. (2006). Designing a Neural Network for GPS/INS/PL Integration. *International Global Navigation Satellite Systems Society IGNSS Symposium 2006*.

Wei, M., Schwarz, K.P. (1990). Testing a decentralized filter for GPS/INS integration. *IEEE Position, Location and Navigation Symposium*, Las Vegas, Nevada.

Wei, M. and Schwarz, K.P. (1994). An error analysis of airborne vector gravimetry. *Proceedings of the International Symposium on Kinematic Systems in Geodesy, Geodynamics and Navigation, KIS-94*, Banff, Canada, 509-520.

Wei, M. and Schwarz, K.P. (1995). Analysis of GPS-derived acceleration from airborne tests. *International Association of Geodesy Symposium G4, IUGG XXI General Assembly.* Boulder, Colorado.

Wei, M. and Schwarz, K.P. (1998). Flight test results from a strapdown airborne gravity system. *Journal of Geodesy, Vol.72*, 323-332.

Williams, S. D. P., Baker, T. F. and Jeffries, G. (2001). Absolute gravity measurements at UK tide gauges, *Geophysical Research Letters, 28*, 2317-2320.

Witchayangkoon, B. (2000). Elements of GPS Precise Point Positioning. Ph.D. dissertation, Dept of Spatial Information Science and Engineering, Univ of Maine, USA.

Wu, J. T., Wu, S. C., Hajj, G. A., Bertiger, W. I. & Lichten, S. M. (1993). Effects of antenna orientation on GPS carrier phase. *Manuscr. Geodaet., vol. 18*, 91-98.